UNIVERSITÀ
DEGLI STUDI
FIRENZE

School of engineering

Department of Industrial Engineering of Florence (DIEF)

DOCTOR OF PHILOSOPHY in INDUSTRIAL ENGINEERING

Address "*Energy engineering and Innovative Industrial Technologies*"

CYCLE XXVII

Academic Discipline ING-IND/09

Development of probes for the measurement of total pressure/total temperature in wet gas conditions

Tutor

Prof. Giampaolo Manfrida

Industrial Tutor

Marco Marrazzo, PhD, *GE Oil & Gas*

Academic Supervisor

Prof. Daniele Fiaschi

PhD Candidate

Eng. Francesco Maraschiello

PhD Course Coordinator

Prof. Maurizio De Lucia

2012-2014

Volli, e volli sempre,
e fortissimamente volli

Vittorio Alfieri

E' tutto sedimentato sotto
il chiacchiericcio e il rumore,
il silenzio e il sentimento,
l'emozione e la paura,
gli sparuti incostanti sprazzi
di bellezza, e poi lo squallore
disgraziato, e l'uomo miserabile

La Grande Bellezza

Declaration

I hereby declare that this submission is my own work and, to the best of my knowledge and belief, it contains no material previously published or written by another person, nor material which to a substantial extent has been accepted for the award of any other degree or diploma at University of Florence or any other educational institution, except where due references are provided in the thesis itself.

Any contribution made to the research by others, with whom I have been working at the University of Florence or elsewhere, is explicitly acknowledged in the thesis.

Acknowledgments

Quando si giunge alla fine di un percorso così bello e così lungo, sono molte le persone che abbiamo il dovere di ringraziare per quello che ci hanno insegnato. Per me la tesi di dottorato rappresenta la fine di un percorso di studi, iniziato da bambino e concluso adesso, dopo tanta fatica ma anche dopo altrettante soddisfazioni. Mi sento davvero felice di potermi guardare indietro senza rimpianti, e allo stesso tempo sono carico di entusiasmo per il percorso lavorativo che sto per iniziare. Spero davvero di mettere a frutto le nozioni tecniche che ho appreso in questi anni, ma soprattutto la mia voglia di sorridere e di imparare giorno dopo giorno.

Il mio primo ringraziamento va a DIO, Che non ha mai smesso di credere in me e di farmi scoprire quali sono davvero le cose che contano. Un grazie davvero sentito anche a mio padre e mia madre, il cui affetto mi ha sempre accompagnato e a Giulia, che con il suo amore, la sua passione e la sua capacità di sognare ha rotto gli schemi di una vita bella ma monotona. E poi Fulvio, che mi ha accompagnato nel mio percorso di vita facendomi crescere giorno dopo giorno, Andrea, un fratello più che un amico, e tutti gli amici di Masiano, con cui ho condiviso i momenti più significativi della mia vita, ed i ragazzi del dopocresima, il cui affetto e la cui fiducia mi riempiono di gioia il cuore.

Ringrazio di cuore anche il Prof. Manfrida, la cui passione per la ricerca è davvero entusiasmante, il Prof. Fiaschi, una presenza davvero continua e significativa nel mio percorso di laurea e di dottorato, l'Ing. Marrazzo, un esempio di impegno, correttezza e onestà, il team OGTL, l'Ing. Camatti, un riferimento importante ed un modello da seguire, il Prof. Rinchi, la Dott.ssa Tuci, ed infine i miei compagni d'ufficio Duccio, Gianmaria e Luigi. Un ultimo grande ringraziamento va a Riccardo, che è stato davvero un collega

insostituibile, ma soprattutto un amico fidato e sempre presente nei momenti belli ed in quelli più bui.

Summary

Subsea compression is becoming an important technology in the exploitation of natural gas resources, especially in the North Sea. The well stream is typically a mixture of hydrocarbon gases, liquids and water, with a liquid content up to 5% in volume. The wet flow can be processed with liquid/gas separators before its compression, or compressed as it is. The use of separators or scrubbers, which is possible in most land based applications, becomes exceedingly expensive for subsea applications. For this reason, technology for wet gas compression is currently being developed. Several studies focus on the development of such compressors, but low attention is paid to the measurement technologies and test accuracy. Performance tests on these machines involve the measurement of several parameters, which is usually performed by standard probes. This is not recommended in a wet environment, where the droplets can come in contact with the sensing element of the sensors and considerably perturb the measurement. For this reason, wet tolerant probes are a fundamental issue in order to execute reliable measurements.

The objective of the present work is the development of a validated methodology for the design and characterization of wet tolerant probes for the measurement of total pressure and total temperature of gas phase in wet conditions.

Starting from a literature search, some conceptual designs of probe were developed, together with an analytical model for their detailed design. The model is based on the specific application operating conditions and on a first attempt geometry. It provides a complete analysis of probes performance, from the fluid dynamics and the structural point of view. After the first iteration, the user can change the value of the design parameters, until the required performance is reached. The developed tool aims to become a reliable instrument for wet tolerant probes design. For this reason, it requires a validation.

The model was used to design probes for a real case, which consisted in a pressurized two phase flow composed by air and water, with a liquid content up to 3% in volume. From the structural point of view, probes reduced size and the high stress deriving from the interaction with the droplets lead to two calculation steps: first, a calculation was done applying traditional engineering sizing rules on a simplified probe assembly model; then, a 3-D Finite Element Analysis (FEA) was carried out to validate the model. As expected, the results of the numerical analysis confirmed those of the analytical model, in terms of mechanical stress and natural frequencies.

The design obtained with the model was then used to manufacture some probe prototypes, using a Direct Metal Laser Sintering (DMLS) technique. After manufacturing, some ping tests were performed on probes, in order to estimate their first natural frequencies. The results of these tests confirmed those obtained with the numerical analyses, with percentage relative errors on the first natural frequencies lower than 2.0%.

After this step, some preliminary performance tests were run in dry conditions, in the aerodynamic facility of GE Oil & Gas (Florence). A good agreement between analytical and experimental data was obtained in terms of recovery factor, especially for total pressure probes.

The results of tests in dry conditions are not sufficient to validate the probes in a wet environment: to this end, tests were also run in wet conditions, in a facility located at Southwest Research Institute (SwRI, Texas). The results showed a certain agreement between analytical and experimental results, even though the test rig was not specifically designed for probes validation and the test conditions were not suitable for getting all the needed information. The measurement uncertainty also affected the results. For this reason, a dedicated test rig for an accurate wet probes validation is currently under development.

The testing and post processing activities were followed by a study on technologies for the improvement and miniaturization of probes. A specific research was conducted on super-hydrophobic materials for industrial applications. These materials represent an important way to improve and miniaturize probes, which again should require experimental tests. The dedicated test rig will be an useful instrument for the validation of probes and the investigation of new solutions to improve their design.

Contents

List of figures

List of tables

Nomenclature

Symbols

A Area, m^2

a Speed of sound, m/s

AR Aspect ratio

C Discharge coefficient

C_D Drag coefficient

C_m Center of mass

cp Specific heat, J/kg K

d Diameter, m

dis Displacement, m

E Young modulus, N/mm^2

f Correction factor, roughness factor (Cassie-Baxter)

F_D Drag force, N

FoS Factor of safety

fr Frequency, Hz

GVF Gas Volume Fraction

g Constant gravity, m/s^2

h Height, m

I Moment of inertia, m^4

k	Collection efficiency, stiffness, N/m
L	Length, m
LMF	Liquid Mass Fraction
LVF	Liquid Volume Fraction
m	Mass, kg
$\dot{m}$	Mass flow rate, kg/s
Ma	Mach number
M_B	Bending moment, N m
N	Number of particles
Ob	Obedience number
P	Pressure, bar
PC	Purge coefficient
q	Uniformly distributed load, N/m
$\dot{Q}$	Volumetric flow rate, m^3/s
r	Recovery factor, roughness factor
Re	Reynolds number
SF	Stress factor
ST	Strouhal number
T	Temperature, °C
v	Velocity, m/s
Vol	Volume, m^3
W	Modulus of elasticity, m^3
Z	Number of devices

XXIV

Greek symbols

γ Specific heat ratio, interfacial tension N/m or J/m^2

δ Density ratio (liquid to gas)

θ Yaw angle, Contact angle °

μ Dynamic viscosity, kg/(m s)

ρ Density, kg/m^3

σ Tension, N/mm^2

τ Tension (shear and torsion), N/mm^2

ω Pulsation, rad/s

Subscripts

a   Allowable (referred to tension)

act   Actual (referred to geometry)

alt   Alternating

B   Bending

bk   Blockage

calc   Calculated (analytical model)

cd   Converging duct

d   Droplets

des   Design

di   Droplets impact

dis   Discharge

e   External

el   Endurance limit

eq   Equivalent

f	Fatigue
fr	Frontal
g	Gas
h	Homogeneous
i	Internal
in	Inlet
l	Liquid
lat	Lateral
LV	Liquid vapor (interface)
max	Maximum
mean	Average
meas	Measured
min	Minimum
mod	Analytical model
ms	Mini-shield
nat	Natural, referred to frequency
net	Net value
nom	Nominal (referred to geometry)
out	Outlet
ph	Purge hole
ps	Pressure sensor
R	Ratio
s	Shield
sens	Sensor
sh	Shear
SL	Solid liquid (interface)

st	Stem
suc	Suction
SV	Solid vapor (interface)
T	Torque
test	Experimental result
ts	Temperature sensor
u	Ultimate (referred to tensile strength)
vh	Vent hole
VM	Von Mises
vs	Vortex shedding
x	Local coordinate, parallel to probe axis
y	Local coordinate, orthogonal to probe axis
yld	Yield
0	Total conditions

Miscellaneous

$()^{CB}$	Cassie-Baxter
$()^{W}$	Wenzel
Δ	Difference
$()^{*}$	Fictitious

Acronyms

CAH	Contact angle hysteresis
DMLS	Direct metal laser sintering

RTD   Resistance Temperature Detector

SwRI   Southwest Research Institute

TC   Thermocouple

TP   Test point

TPP   Total pressure probe

TT   Transient test

TTP   Total temperature probe

Introduction

Context and significance of the present research

Because of the increasing demand for natural gas and the limited resources [1, 2], the oil and gas industry is going to develop new technologies to access remote gas reserves and to improve the exploitation of the existing ones. Within this context, subsea compression is becoming a fundamental technology for the exploitation of gas reserves in the North Sea [3]. The processed fluid is a mixture of hydrocarbon gases, liquids and water. The Liquid Volume Fraction *LVF* is defined as:

$$LVF = \frac{\dot{Q}_l}{\dot{Q}_l + \dot{Q}_g} \qquad (I.1)$$

and can reach in practice values of 5%. The wet flow can be processed with liquid/gas separators before its compression, or compressed as it is. The use of separators or scrubbers, which is possible in most land based applications, becomes exceedingly expensive for subsea applications, where the footprint reduction of the equipment plays also a crucial role. For this reasons, the development of wet tolerant compressors is a fundamental issue. A few papers [4-6, 8-11] deal with the development and test of wet tolerant single-stage and two-stage centrifugal compressors, but low attention is paid to the measurement technologies and test accuracy.

In 2005, Brenne et al. [4] presented some experimental results of a single-stage centrifugal compressor operating under wet gas conditions. The test was executed in cooperation with Statoil. The compressor was run using a mixture of hydrocarbon gas and hydrocarbon condensate. Thermodynamic and mechanical performance of the machine

were evaluated at different values of Gas Volume Fraction *GVF*, compressor test speed, suction pressure and liquid injection pattern. *GVF* is the one's complement of *LVF*:

$$GVF = \frac{\dot{Q}_g}{\dot{Q}_l + \dot{Q}_g} \qquad (I.2)$$

The authors found that, relative to dry conditions, the compressor pressure ratio increased. This trend was attributed to the larger density of the fluid that was handled by the compressor in wet conditions. The temperature ratio decreased and the polytropic efficiency also decreased with increasing *LVF*. The efficiency drop was strongly affected by the suction pressure of the compressor, which influences the density of the two flows (i.e. higher Liquid Mass Fraction *LMF* for the same *LVF*). *LMF* is defined as:

$$LMF = \frac{\dot{m}_l}{\dot{m}_l + \dot{m}_g} \qquad (I.3)$$

The results of the test showed also that the compressor performance in wet conditions were independent of the form of the injection (atomized droplets or liquid film). Finally, the power consumption for the wet compression was higher than separating the two phases and boosting them separately.

Another work was presented in 2006 by Hundseid and Bakken [5], who pointed the importance of developing an accurate method for performance prediction in wet gas compression. In the first part of the paper there is a paragraph on wet gas compression fundamentals, where the authors state that the homogeneous flow model represents a suitable method to describe the mixture. A direct integration approach for wet gas performance analysis is then proposed. The compression is divided into a large number of sub compressions, and the properties of real gas along the compression path are used. The phase transitions along the compression path are also taken into account by the model.

Hundseid et al. [6] presented another paper in 2008, in cooperation with Statoil. The authors reported the performance of a single stage centrifugal compressor again, and developed a method for the comparison between wet and dry compressor performance data. They introduced a mass flow correction and considered the changes in compressibility with the use of a two phase speed of sound model, based on Wood's

correlation [7]. This model can be applied if the multi-phase flow is homogeneous. The homogeneous flow model has been generally adopted in wet gas compression, even if more detailed studies are required to demonstrate that it represents a correct approach.

In 2008, Grüner et al. [8] investigated the performance of an airfoil in an air-water mixture. The work was developed in cooperation with Statoil. The influence of wet gas on the airfoil performance was investigated at different angles of incidence and different values of *GVF*. The authors stated a performance degradation of the airfoil at increased liquid mass flow rate, due to a premature boundary layer separation. The authors concluded that a revised compressor design was generally required in order to make a compressor able to handle a wet gas.

Fabbrizzi et al. [9], from GE Oil & Gas, presented a paper in 2009. They performed some tests on a laboratory scale impeller at atmospheric suction conditions. The impeller was a standard, with no design adjustments for wet streams. The flow consisted in an air-water mixture, with a *LMF* ranging between 0% and 50% and an average droplet diameter between 50 μm and 75 μm. The results of the tests showed that the compressor performance were strongly affected by the wet gas in terms of adsorbed power, efficiency and compressor characteristics. As a comparison with the dry phase, the compressor pressure ratio increased for small amounts of injected liquid (*LMF* lower than 10%). For *LMF* higher than 10% the pressure ratio decreased. These results are not in agreement with those presented in [4] and [6]. The authors pointed that this difference was probably caused by a difference in the test conditions, which led to different values of density ratio between the two phases. The influence of the form of water injection on the performance was also carried out. When the water was introduced into the impeller in the form of a liquid film on the pipe wall, the influence of the droplet size on the performance was negligible. When the liquid was directly atomized onto the compressor inducer, the droplet size strongly affected the performance. Small droplets led to better performance. The authors underlined also the problems of accurate measurements of gas properties, especially total temperature, in wet conditions.

After the first tests on a single stage compressor [9], GE Oil & Gas performed some tests on a two-stage centrifugal compressor. The results of this analysis are reported in [10] and [11]. The tests were performed in a facility located at Southwest Research Institute

(SwRI, Texas), with a mixture of air and water at a suction pressure of 20 bar and values of *LVF* ranging from 0 to 5%.

Ransom et al. [10] focused on the mechanical performance of the machine under wet conditions. They observed that the influence of wet gas operation on radial vibration was negligible for the compressor which had been tested. Conversely, it had a significant impact on the axial vibration. The results showed also an increase in the thrust load, caused by an increased pressure ratio of the compressor under wet gas conditions.

Bertoneri et al. [11] reported the results of the measured performance from the thermodynamic point of view. The results and the physical trends are similar to those discussed in [4] and [6]. Relative to dry conditions, the pressure ratio increased with increasing LVF, and the temperature ratio decreased. Finally, as the LVF increased, the power absorbed by the compressor increased too and the polytropic efficiency decreased.

From the works cited above, it emerges that wet gas compression is a new and important topic for the oil and gas industry. Several studies focused on the development and test of wet gas compressors, but low attention was paid to the measurement technology and test accuracy. Performance tests on such machines involve the measurement of several parameters, including total pressure and total temperature. In the previous works, such parameters have been measured with conventional probes, even if the authors pointed that this was not the best choice. The droplets could come in contact with the sensing element of the probes and lead to measurement errors. For this reason, the development of wet tolerant probes adapted to such an environment represents a fundamental issue in order to perform reliable measurements.

Measurements in turbomachinery: standard probes

Before presenting the previous attempts to design wet tolerant probes it's important to focus on the standard probes for measurements in turbomachinery, with special attention to total pressure and total temperature. The present section is a short and general introduction on sensors and probes for the measurement of static and total pressure as well as temperature in turbomachinery.

The measurement of static pressure P, together with that of static temperature T, is necessary to define the thermodynamic state of a real substance. In order to characterize the performance of turbomachines, where the flow is in motion, it's important to measure also total pressure P_0 and total temperature T_0 of the operating fluid.

The sensor for **pressure** measurements usually consists of an open ended tube, located in a small perpendicular hole in the wall, called *static pressure tap* [12], installed in a region where the flow is aligned with the wall. In order to avoid flow disturbance, the hole must have a small diameter (d < 1 mm), be perfectly orthogonal to the wall, and free from bevels. The best values for length/diameter hole ratio are between 2 and 5. The measurement error is expressed as a function of the dynamic pressure. Fig I.1 represents the influence of hole shape on pressure measurements. The percentage values indicate the error respect to the dynamic pressure.

The measuring principle discussed above is the basis of static pressure probes. Such devices are used to measure the static pressure of a flow in locations away from the walls. Several examples of static pressure probes can be found in [12]. The choice of the probe depends on the available space, the application (Reynolds and Mach number), and the required accuracy. The measurement accuracy depends on holes positioning and direction, flow direction, etc. Referring to a Prandtl Pitot tube [13, 14], Fig I.2 represents the errors on static pressure measurements induced by the hole-tip spacing and by the influence of hole support spacing.
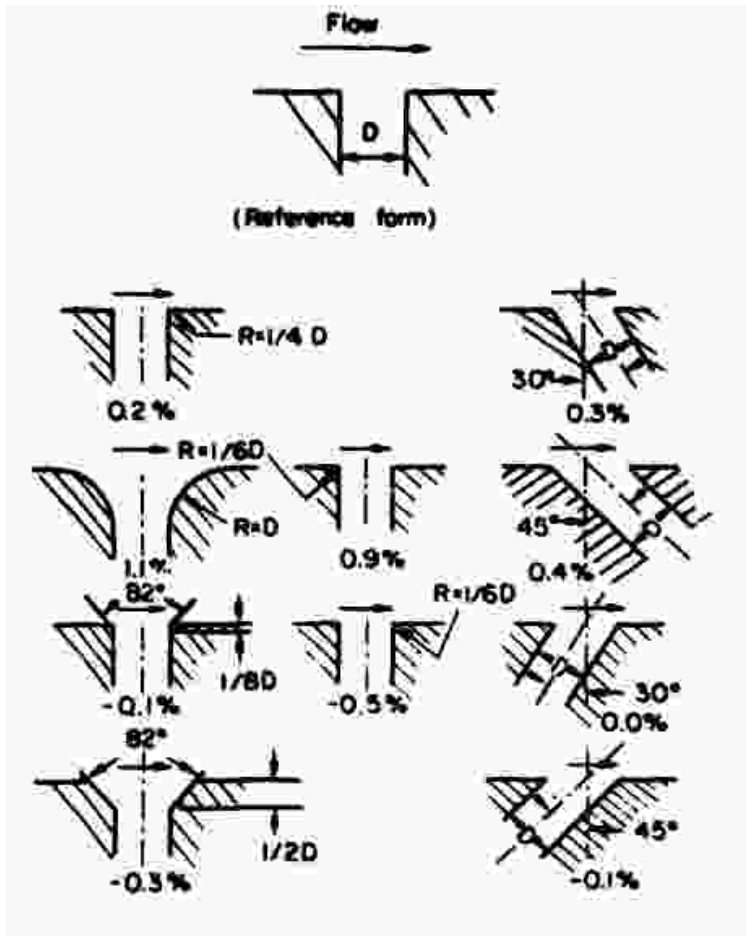
Figure I.1: Influence of orifice configuration on static pressure measurements [12].
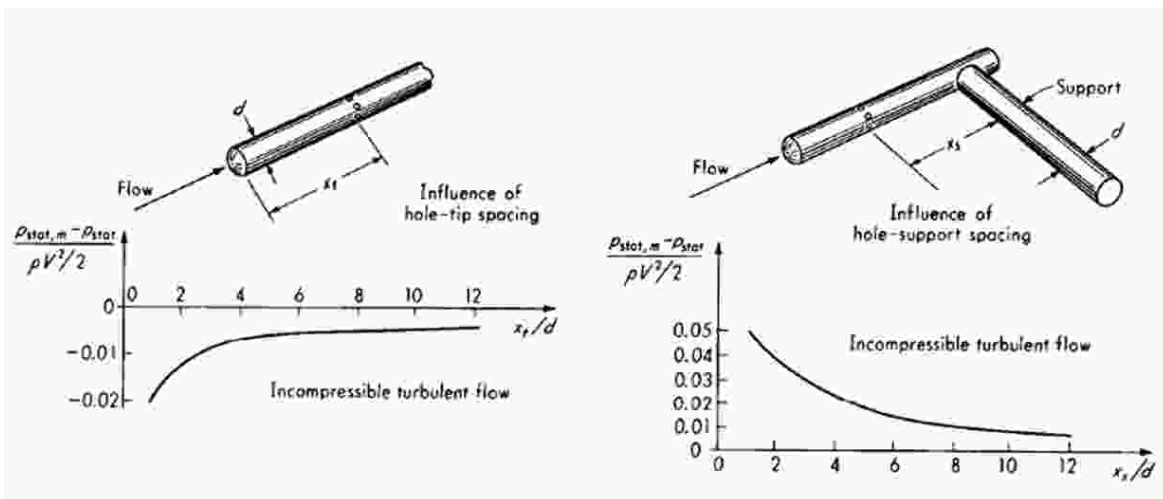
Figure I.2: Influence of nose geometry and support on static pressure measurements with a Prantl Pitot tube [14].

As described in [12], static pressure probes are sensitive to angular deviation. Fig I.3 shows the yaw characteristics of three static pressure probes [12]:
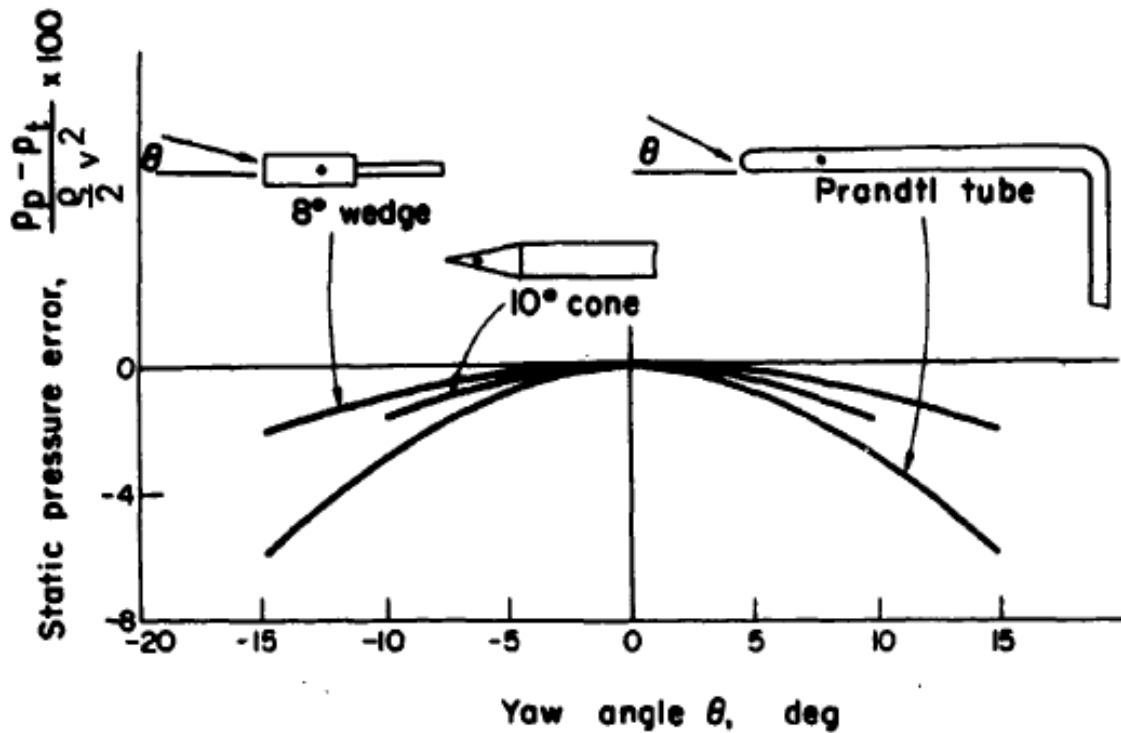
Figure I.3: Yaw characteristics of three static pressure probes at low speeds [12].

The **total pressure** is obtained by measuring the pressure at a stagnation point on the probe; stagnation conditions are theoretically achieved by decelerating the flow to zero speed by a frictionless process. A total pressure probe usually consists of an open-ended tube aligned with its axis parallel to the gas stream and with its mouth facing upstream. Total pressure is less sensitive to misalignment between the flow and the probe. A deep discussion on the effects of inlet geometry on flow angle characteristics of total pressure tubes was proposed by Dudziniski and Krause [15]. Fig. I.4 shows the variation in total pressure error with flow angle for three types of total pressure tubes. The pressure error is expressed as the ratio between the recovered pressure and the maximum recoverable value. As emerges from Fig. I.4, the best angular insensitivity is obtained with shielded probes, which are called *Kiel probes*. Such probes, developed by Kiel [16] for total pressure measurements, are nowadays used both for total pressure and total temperature. The pressure or temperature sensing element is located inside a beveled shield, which ensures a great insensitivity of probe to changes in yaw angle and, depending on the probe, it decelerates the flow. For this reason, Kiel probes are used when the direction of flow is unknown or it varies with operating conditions.
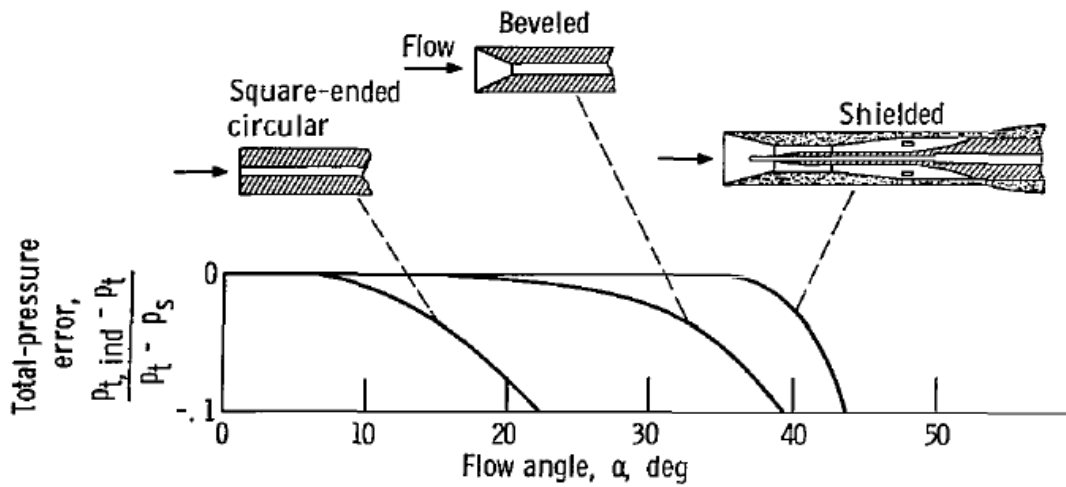
Figure I.4: Variation in total pressure error with flow angle for three types of total pressure tubes [15].

Fig. I.5 shows the original design developed by Kiel [16] and some examples of standard industrial probes from United Sensor Corporation [17]:
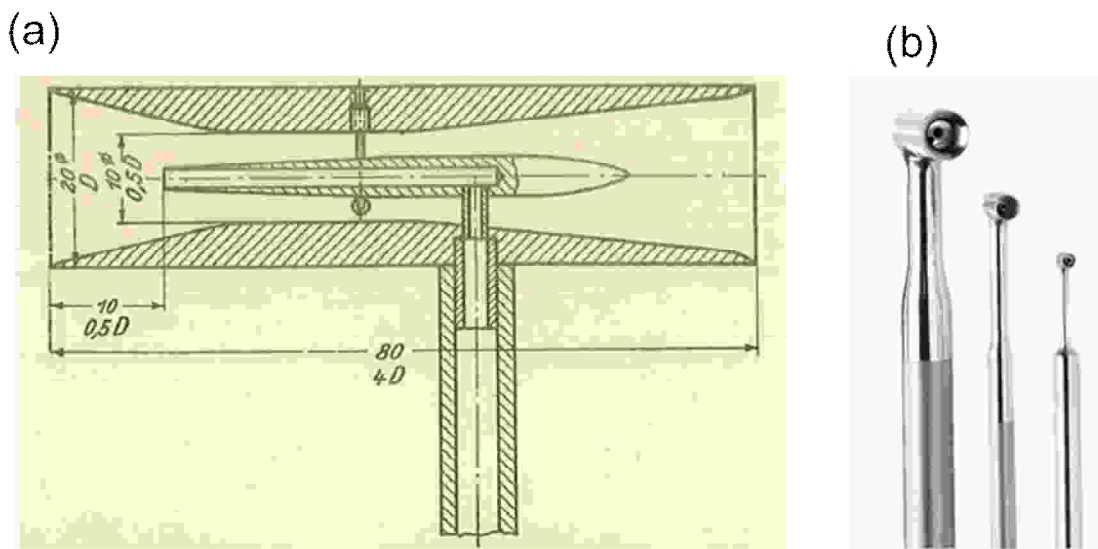
Figure I.5: Kiel probes. (a) Original design developed by Kiel [16]; (b) standard probes from United Sensor Corporation [17].

The **temperature** sensors commonly used for turbomachinery performance characterization are the following:

- Thermocouples
- Resistance temperature detectors

- Thermistors

Thermocouples are the most used. In fact, compared to the others, they offer a small size, an adaptability to high temperature applications, an ease of manufacture and a small cost. Total temperature probes developed in the present research activity use standard K thermocouples.

The design of a probe for the measurement of total temperature in a gas flow is more difficult than the corresponding for total pressure. In order to measure total temperature, the sensor must be located in a region where the flow is in stagnation conditions. As for total pressure, Kiel probes can be used also for total temperature measurements. However, some modifications are required. First of all, in a total temperature probe the gas is not brought to stagnation condition inside the shield. In fact, in order to achieve a great thermal exchange between the flow and the sensing element, a certain flow must be ensured around it. The velocity can be controlled by vent holes (Fig. I.6), which determine a certain flow rate inside the shield. Glawe et al. [18] suggested how to attain a well-designed probe in terms of vent holes geometry, size and position. The velocity error, which represents the ratio of the actual to the total thermal energy that will be available from the isentropic deceleration of the gas stream at the junction can be estimated referring to [19], [20] and [21].

Depending on their application, the probes can be affected also by other error terms. The most important errors are the conduction error and the radiation error; the radiation error, which is not important for the present application, becomes significant in gas turbine hot section measurements. References [19-21] show the basic approach for measurement errors calculation; reference [22] describes the validation of the model shown in [19].

The conduction error is induced by the thermal energy transfer by means of conduction along the thermocouple wires towards shield wall and probe stem. In order to reduce such an error, one can operate on probe geometry and sensor type. The conduction error can be reduced increasing the thermocouple length/diameter ratio, increasing the coefficient of convection heat transfer between the flow and the sensing element, decreasing the temperature difference between the sensing element and its support, and decreasing also the coefficient of thermal conductivity of the thermocouple wire [19-21].

For high temperature applications, engine parts surrounding the probe might have temperatures which are very different from that of the sensor; this condition results in a significant radiative heat transfer. The radiation error depends on wall emissivity, convective heat transfer between the thermocouple and the wall, and fourth power of junction and wall temperature [19-21]. The radiation error can be reduced by providing the sensors with radiation shields (Fig. I.7).

Figure I.6 represents a schematic cross section of a total temperature sensor:
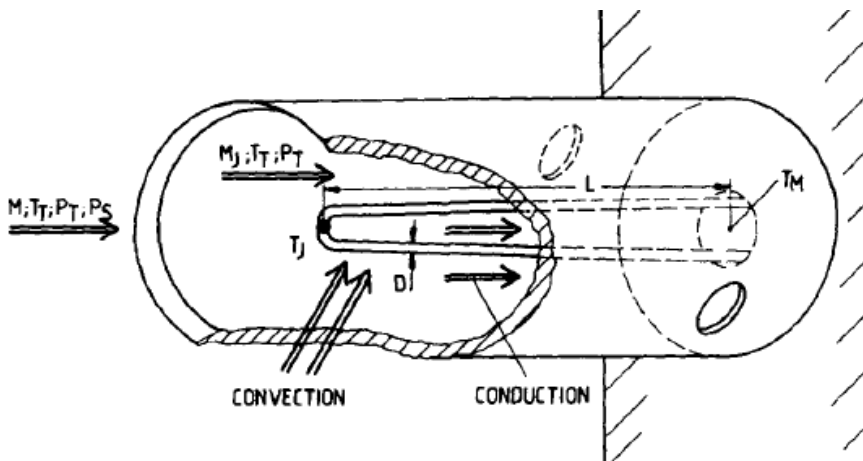
Figure I.6: Conceptual scheme of a general total temperature sensor [20]

Figure I.7 shows the effect of radiation shields on radiation errors.
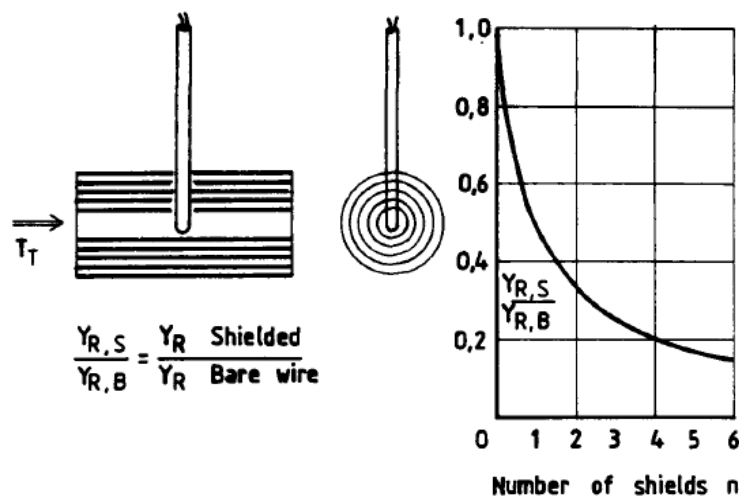
Figure I.7: Effects of radiation shields on radiation error [20].

Total pressure and total temperature probes described in this section can be provided with single or multiple sensors. In the second case they are called *rakes*. A rake is a probe

assembly containing two or more similar sensors or combination of sensors at different radial position. Each sensor is located inside a shield. Such probes offer several advantages, for example the capability to measure total pressure or total temperature profiles, together with the need of using a single support for all the shields. Several examples of rake design can be found in [20].

Wet tolerant probes: prior art

As emerges from what discussed above, the development of probes for the measurement of total pressure and total temperature in wet gas compressors is a new challenging topic. A wet gas compressor operates with a high pressure mixtures of hydrocarbon gases, liquids and water, with a pressure up to 80 bar at compressor inlet and 200 bar at compressor discharge. A well-designed probe for such an environment should tolerate large amounts of liquid without affecting the measurement accuracy for the gas stream, and should have a sufficiently high static and dynamic structural resistance under a harsh environment. The use of conventional probes [15-18, 20-21], for example Kiel probes and rakes, is not recommended in a wet environment.

In 1958, Dussourd and Shapiro [23] proposed a probe for the measurement of stagnation pressure of the gas phase in a stream of gas laden with liquid droplets or solid particles. The probe consists in a decelerating tube, with some pressure taps in its internal wall and a hole for its purging. The hole is located at the bottom of the probe and it has a passage area between three and five percent of the inlet area. A conceptual design of such a probe is represented in Fig. I.8:
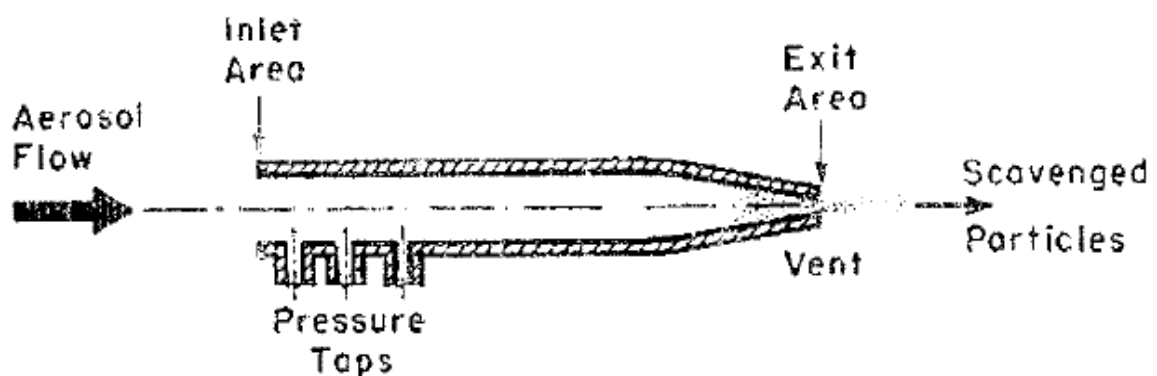
Figure I.8: Dussourd and Shapiro's probe conceptual design [23].

The probe was tested in a sub atmospheric tunnel with an air-water mixture as operating fluid and a maximum *LMF* of 25%. The solution presented in [23] is an interesting starting point. However, this design is not suitable for the present application, where the liquid content is very high.

In 1986, Murthy et al. [24] proposed a probe for the measurement of total pressure of both the gas phase and the mixture of a droplet-laden gas flow. The probe, whose conceptual design is represented in Fig. I.9, is based on the work of Dussourd and Shapiro [23].
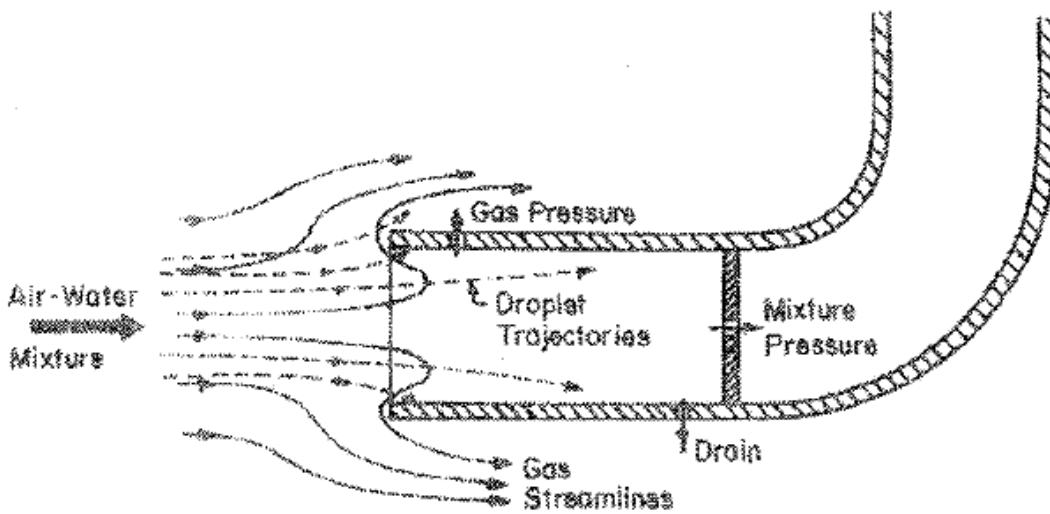
Figure I.9: Conceptual design of a probe for the measurement of stagnation pressure of gas phase and mixture of a droplet-laden gas flow [24].

It consists in a decelerating tube, which leads to total conditions for the gas phase in its internal region. The total pressure of the gas phase, as in [23], is measured by a pressure tap, located adjacent to the probe inlet. A second port is placed at the end of the tube. Because of the momentum exchange between the gas phase and the droplets in the internal region of the probe, the authors stated that it measures the total pressure of the mixture. Finally, a purging hole drains the system from any accumulating water. The probe, which was designed and tested for a LMF of approximately 5%, is unsuitable for a wet gas compressor.

Benton et Seay [25] patented a Pitot tube type apparatus adapted for measuring fluid flow rate in a gas flow containing entrained liquid droplets. The probe was specifically

designed for installations such as the spray towers of wet gas scrubbers. The probe, represented in Fig. I.10, has a total pressure sampling port, parallel to the flow, and a static pressure sampling port, opening normal to the flow and located downstream the other. In order to avoid any accumulating liquid into the transmitting lines, a flow of blow-back gas is intermittently passed through them. A significant element of Benton's probe is a flat plate, which extends in the plane of the static pressure port. The authors suggest that such a plate precludes droplets from blinding the static pressure port.
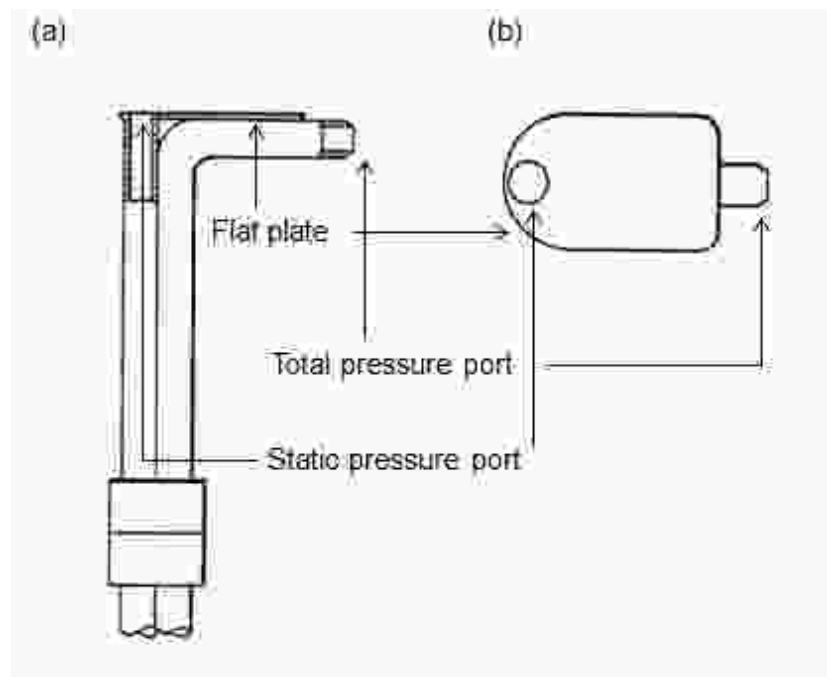
Figure I.10: Pitot tube type apparatus adapted for measuring fluid flow rate in a gas containing entrained liquid droplets (adapted from [25]): (a) cross-sectional, lateral view; (b) top view.

The probe proposed in [25] is not reliable for measurements in wet gas compressors. The structure of the probe is not appropriate for a harsh environment and the total pressure port is not optimized for wet conditions.

Colten et. al [26] have recently patented a new design of Pitot probe, optimized to prevent water blockage of the pressure orifice. The authors pointed that such probes are particularly useful for use on unmanned aerials vehicles (UAV) and other small aircrafts. The probes utilize passive methods in the form of geometrical and/or material configurations to prevent pressure orifice blockage by water droplets. Three configurations of such probes are represented in Fig. I.11. In the first configuration (*configuration a*) the

internal passage of the probe is provided with a coating of hydrophilic material. The hydrophilic material performs the functions of drawing water away from the orifice and collecting and holding water. When the material is saturated, the probe must be replaced with a new one.
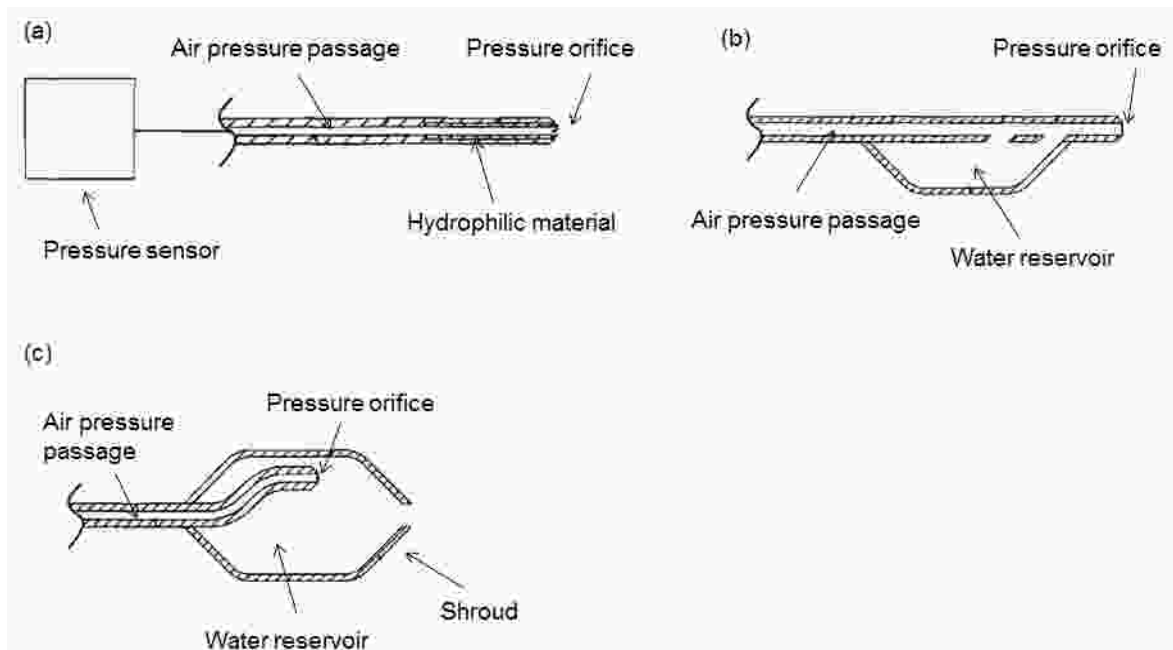
Figure I.11: Conceptual design of Pitot probes with water blockage prevention (adapted from [26]): (a) hydrophilic material; (b) water reservoir; (c) shroud and water reservoir.

In the second configuration (*configuration b*), the mean to prevent plugging of the orifice consists in an increased diameter of the internal passage, which forms a water reservoir. The reservoir collects the droplets and prevents the flooding of the air pressure passage. When the reservoir is filled with water, the probe must be replaced. The third configuration (*configuration c*) is equipped with a shroud, which prevents water droplets from directly impinging on the pressure orifice and forms a water reservoir. As in the previous configurations, the system has no means for water purging. When the reservoir is filled with water, the probe must be replaced. The solutions proposed in [26] are interesting, even if they are unsuitable for a wet gas environment, where the amount of liquid is very high.

The first design of a probe for the measurement of total temperature in wet conditions was proposed by Kovach et al. [27]. The probe was specifically designed for measurements in centrifugal compressors operating with water injection. The LMF ranged

from 2% to 5%. A conceptual design of the probe is represented in Fig. I.12. It consists in a shielded thermocouple, which prevents water droplets from coming in contact with the sensing element. Two holes, located at the bottom of the shield, induce a gas flow around the sensing element, which ensures a certain thermal exchange between the flow and the sensing element. The authors do not describe the shield material.
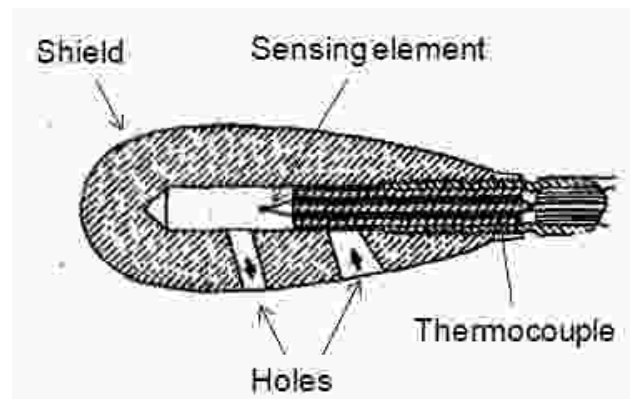
Figure I.12: Shielded thermocouple adapted for measurements of total temperature of gas phase in centrifugal compressors operating with water injection [27].

The probe proposed in [27] represents an interesting solution even if it is not well suited for a heavily wet environment. In such conditions, the vent holes operation is prevented by liquid droplets and liquid film on probe shield.

Another interesting approach for the measurement of temperature in two phase flows can be found in spray drying chambers application [28, 29]. It consists in protecting the sensor from being hit by particles by removing them from the gas stream. The way to separate the droplets from the gas is to utilize their difference in inertia. In 1997, Kievet et al. [28] proposed a micro-separator probe based on this principle (Fig. I.13).
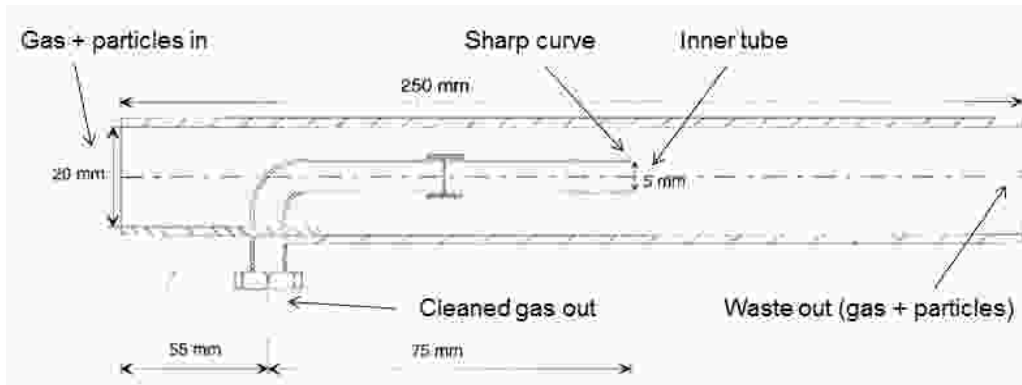
Figure I.13: Micro-separator probe for the measurement of temperature and humidity in a spray dryer chamber (adapted from [28]).

The probe consists in two coaxial tubes. Part of the flow is sucked into the inner tube (a vacuum pump is needed). When the flow is sucked into the inner tube, it has to make a complete U-turn change in direction. Due to their inertia, many of the particles cannot follow the reversed stream. A thermocouple can be located into the inner tube in order to measure the temperature of the gas.

Kock et al. [29] designed a gas probe for measuring gas temperature and humidity in a two-phase flow, based on the layout of Kievet et al. [28]. The probe is represented in Fig. I.14.
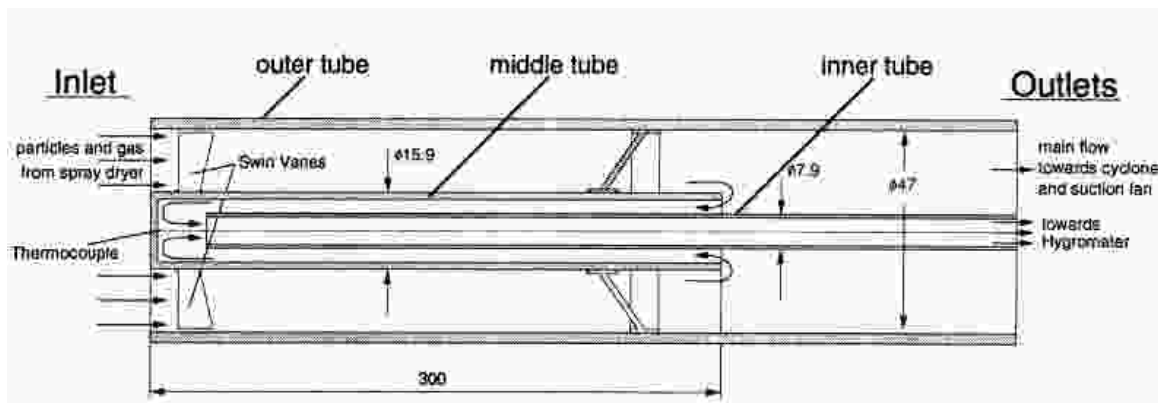
Figure I.14: Micro-separator probe for measuring temperature and humidity in a two-phase flow [29].

The probe consists of three coaxial tubes which form a microseparator. The flow is sucked into the outer tube of the probe by a fan, which is located at the outlet end. Some swirl vanes at the inlet set up a vortex, which forces the particles toward the wall. This is a modification respect to the design proposed in [28]. A portion of the flow is sucked into

the annulus between the middle and the inner tube, changing its direction. The particles, because of their inertia, cannot flow into the annulus. A thermocouple can be located into this region to measure the temperature of the gas. After the second flow reversal, the inner tube leads the flow to a hygrometer. The configurations of probe proposed in [28] and [29] are very interesting. However, they are not suited for total temperature measurements; the dimensions of such devices are also too high for stage measurements in centrifugal compressors.

Dimarzo and Ruffino [30] patented a probe for measuring the temperature of a hot stream laden with liquid droplets. The probe, which was specifically designed for measurements in fire detection systems (sprinklers), is based on an innovative approach. A basic configuration of the system is represented in Fig. I.15.
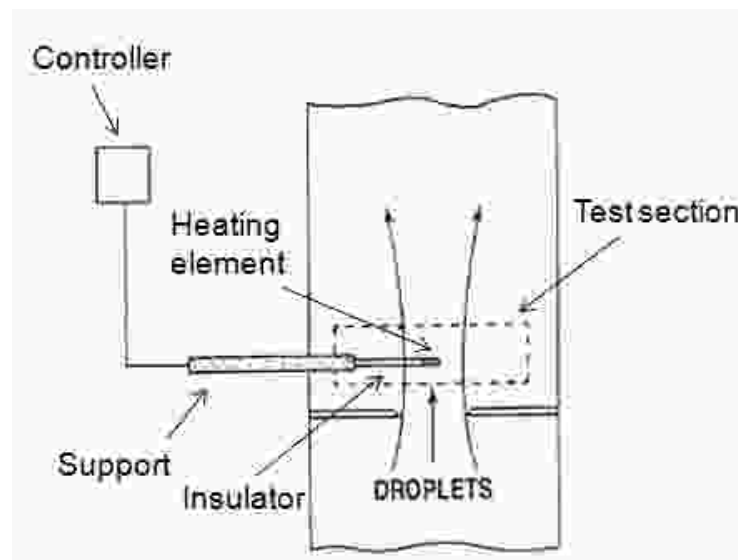
Figure I.15: Schematic drawing of a probe based on the Leidenfrost effect and located in the center of a test section (adapted from [30])

The probe includes a single or multiple heating elements, which are maintained above the Leidenfrost transition condition[1] for the droplets. This solution leads the droplets to slip away from the sensing element and minimizes the thermal exchange between them. During its operation, the heating element is maintained at a temperature which is higher than the

---

[1] The Leidenfrost effect occurs when a liquid droplet is in near contact with a surface, which temperature is significantly higher than the boiling temperature of the droplet. When this condition occurs, a vapor layer is established between the droplet and the surface. The vapor layer insulates the droplet, retards its evaporation and lets it slide away from the hot surface.

gas temperature and the Leidenfrost transition condition for the droplets. As the fluid gets in contact with the probe, there is a thermal exchange between the sensing element and the flow. The heat loss from the probe can be calculated from the power needed to maintain the heating element at a constant temperature. The heat transfer coefficient is determined by calibration. The gas temperature can be obtained by simple heat transfer principles. The advantage of such a solution is that the thermal exchange between the droplets and the sensor is negligible and the calculation of hot gas temperature becomes easier. The probe proposed in [30] is very innovative, even if it cannot be applied in the present application, where some problems of dimensions, thermal exchange and hydrocarbons flammability occur.

The results of the literature review represent a starting point for the present research activity. The works cited above show that a few attempts have been made in order to develop probes for measurements in wet environments. The physical principles and the technical solutions described above represent a starting point, even if the probes were not specifically designed for wet gas compression. For this reason, a new design of probe, optimized for wet gas compression, is needed.

Thesis outline

During this research activity the aspects related to the development of a validated methodology for the design and characterization of wet tolerant probes for the measurement of total pressure and total temperature of gas phase in wet conditions were analyzed. After a literature search, some conceptual designs of probe were developed, together with an analytical model for the mechanical and fluid dynamics detailed design. The model was then used to design some prototypes of probe, based on the operating conditions of a test rig located at Southwest Research Institute (SwRI, Texas). Since the analytical model cannot be considered a reliable instrument without an experimental validation, some prototypes were manufactured and preliminary tested from the structural and the fluid mechanics point of view. The first performance tests were executed in the aerodynamic facility of GE Oil & Gas (Florence). Then, some tests were also run in wet conditions, in the SwRI facility. Such a test rig was not specifically designed for probe validation, even if some interesting results were obtained. For this reason, a dedicated test

rig for an accurate probes validation is under development. After the testing and post processing activities, a study on technologies for the improvement and miniaturization of probes was performed. A research was conducted on super-hydrophobic materials for industrial application, which represent an important way to improve and miniaturize probes. The dissertation will be organized as follows:

Chapter 1. The development of probes specifically designed for wet gas compression involves some issues, related to their fluid dynamics and structural behavior. The most important aspects are described in this chapter, together with the conceptual designs developed during this research activity.

Chapter 2. The detailed design of probes is based on the conceptual design proposed in chapter 1. Starting from the conceptual design, an analytical model for the detailed design has been developed. The model is based on the specific application operating conditions and on a first attempt geometry. It provides a complete analysis of probe performance, from the fluid dynamics and the structural point of view. After the first guess, the user can change the value of the design parameters, until the required performance are reached. The model architecture, together with its input variables, main hypothesis and equations are discussed in chapter 2.

Chapter 3. The analytical model discussed in chapter 2 is run for a pressurized two phase flow, composed by air and water droplets, with a *LVF* up to 3%. The operating conditions are those of a test rig located at Southwest Research Institute (SwRI, Texas). The test rig operating conditions are presented, together with the main model results. A parametric analysis and a FEM static and modal analysis are also discussed.

Chapter 4. The detailed designs obtained with the model were manufactured with a Direct Metal Laser Sintering (DMSL) technique. In chapter 4 probes manufacturing is discussed. The results of some ping tests on the manufactured prototypes are also presented and compared with those of the numerical modal analysis.

Chapter 5. After probes design and manufacturing, some selected prototypes were tested. The first tests were run in dry conditions, in the aerodynamic facility of GE Oil & Gas (Florence), giving some interesting results. Then, some tests were run also in wet conditions, in the SwRI facility. The results obtained were interesting, even if this test rig

was not well suited for probes validation (the test conditions lead the measurement uncertainty to greatly affect the results). The results were not completely sufficient to validate the analytical model, even if they gave some indications, especially for total pressure probes. Since no wet test facility is suitable for wet tests on total pressure and total temperature probes, a new facility for wet probes calibration is under development. In chapter 5 the performed tests in dry and wet environment are discussed and compared with those of the model.

Chapter 6. After the first chapters related to probes design and testing, it is important to discuss how the probes can be improved and miniaturized in order to obtain the optimal solution. One of the most interesting approach for probes improvement and miniaturization is the use of superhydrophobic materials. This chapter is a general introduction to superhydrophobic materials for industrial application. After a first part, which deals with the basic principles of hydrophobicity, the main manufacturing approaches are described. This chapter is the basis for future developments, which focus on the research on these materials and their application on wet probes. The wet facility being developed will be a fundamental instrument for the investigation of new technologies and approaches for probes optimization.

Chapter 7. This chapter summarizes the main steps performed during this research activity, together with the main conclusions and recommendations for future developments.

Chapter 1

Conceptual design

The measurement of total pressure and total temperature of gas phase in wet gas conditions involves some issues. These are primarily:

- Total condition of flow around the sensing element
- Probe flooding
- Interaction between droplets and gas phase inside the probe
- Contact between droplets and sensor
- Structural resistance of the probe
- Great thermal exchange between the flow and the sensing element (total temperature probes)
- Aerodynamic interaction between the flow and the probe

A well designed probe for a wet gas environment should perform accurate measurements for the gas stream, without being affected by the large amount of liquid. The probe should also have sufficiently high static and dynamic structural resistance under a harsh environment. Starting from these considerations and from the literature review, some conceptual designs of probe were developed and patented [31] during this research activity. Such designs will be discussed in this chapter.

1.1 Total pressure probes

In standard Kiel probes [16, 20], the pressure or temperature sensing element is located inside a beveled shield, which ensures a great insensitivity of probe to changes in yaw angle and, depending on the probe, it decelerates the flow. This approach can be used also in a wet gas. However, the presence of droplets inside the gas flow creates a complex three dimensional flow field at probe inlet (Fig. 1.1).
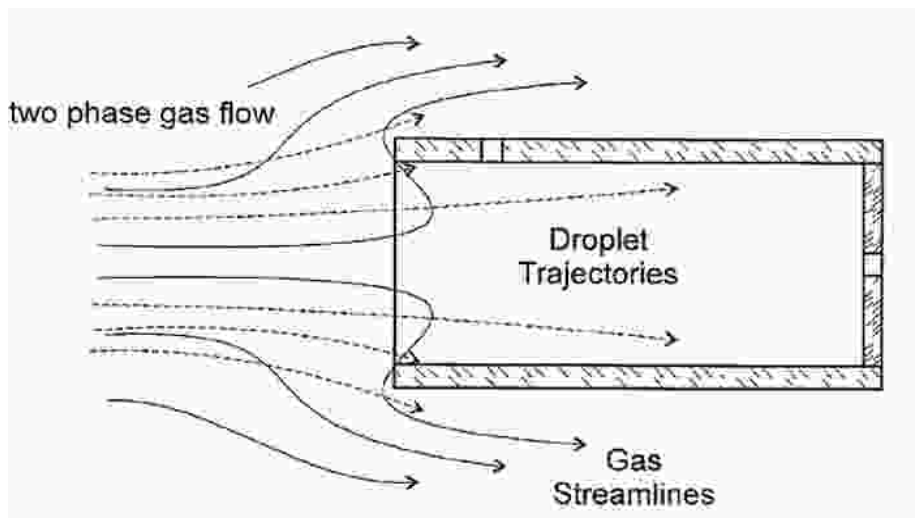
Figure 1.1: Schematic representation of a wet gas flow field near a decelerating probe inlet (adapted from [24]).

As shown in Fig. 1.1, the flow field at probe inlet is characterized by a complex interaction between the droplets and the gas phase. The interaction is accompanied by a momentum exchange between the droplets and the gas flow, which depends on probe geometry (internal and external diameter of the probe) and flow conditions (droplet size, velocity and density of gas and liquid). As the flow gets in contact with the probe, the droplets, which have their greater inertia, tend to continue in straight-line trajectories, with little change in velocity and trajectory. The droplets cross the gas streamlines and undergo a loss of momentum, causing an increase in the total pressure of the gas phase, which becomes different from what would be measured in the absence of liquid. In order to reduce probe disturbance field, Dussourd and Shapiro [23] suggested to minimize probe diameter. When probe diameter is very small, the droplets suffer only small changes in momentum and the gas pressure is relatively unaffected by them. The interaction between the droplets and the gas phase continues inside the shield. The droplets, moving into stagnant air, decelerate

and migrate from the axis of the probe, towards its internal wall (Fig. 1.1). There is a momentum exchange between the droplets and the gas phase in the probe internal region, which leads to an increase in the total pressure of gas phase inside the shield, along its longitudinal axis (Fig.1.2). Dussourd and Shapiro [23] pointed that the maximum pressure occurs at the point where the velocity of the droplets is reduced to that of the gas. In order to measure the total pressure of the gas phase, the sensor must be located near probe inlet, where the stagnation conditions of gas phase prevail.
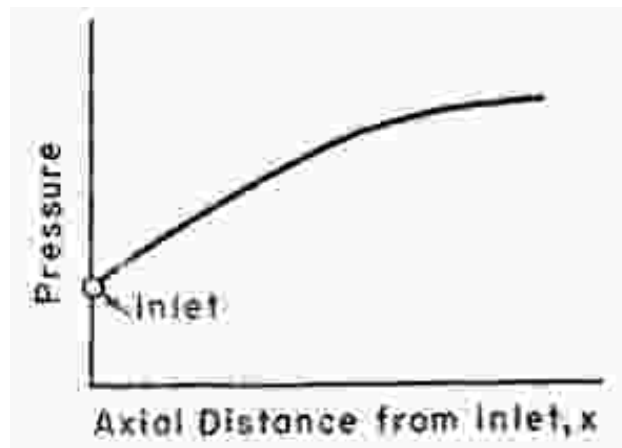
Figure 1.2: Schematic representation of the longitudinal pressure distribution inside probe shield [23].

Starting from the above considerations, a conceptual design of probe has been developed. The probe consists in a stem with a shield on its top. The shield decelerates the gas flow and leads to total conditions of gas phase in its internal region. The droplets tend to continue in straight-line trajectories and to flood the internal region. The flooding of the probe can be avoided by one or more dedicated purging holes, which work using the difference between total pressure inside the shield and static pressure outside. Fig. 1.3 is a schematic representation of shield operation. Fig 1.4 is a 3D CAD drawing of the shield conceptual design. As suggested from Dudziniski and Krause [15], the shield should be internally beveled. The internal bevel makes the shield insensitive to flow direction with certain limits.
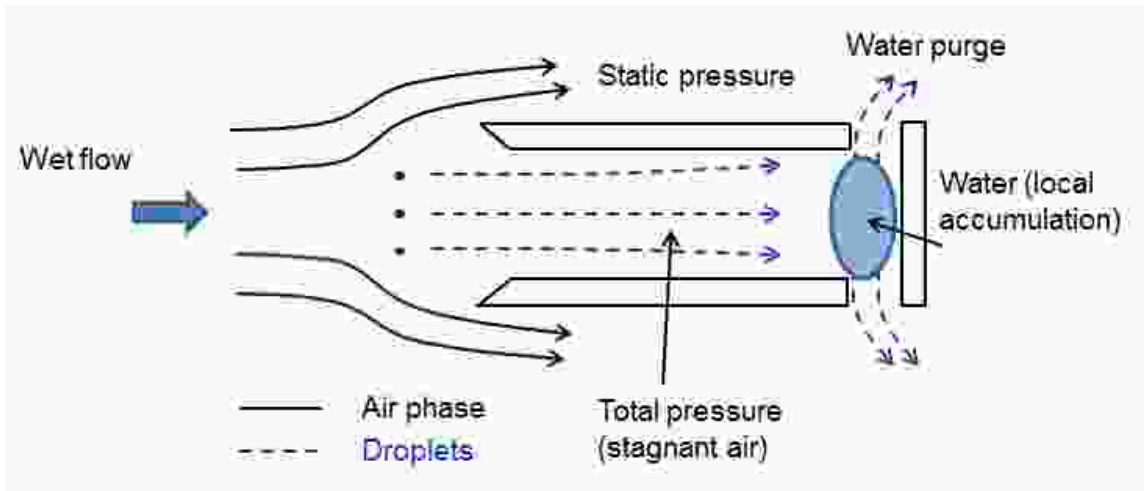
Figure 1.3: Wet gas probe conceptual design: schematic representation of shield functioning.
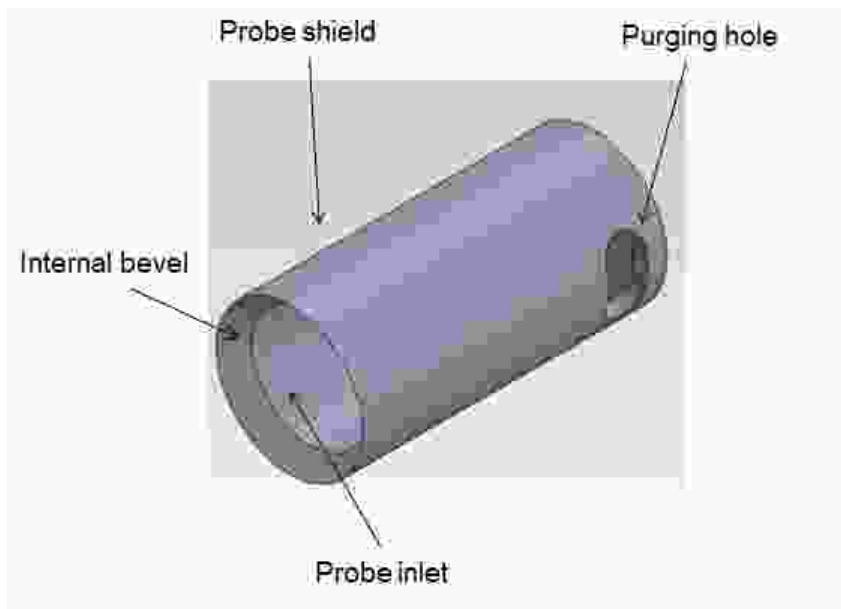
Figure 1.4: Conceptual design of the shield (3D CAD drawing). Axonometric view.

As previously described, a wet gas environment is characterized by large amounts of liquid. The design proposed above is not optimized for such an environment. The difference between total pressure in the internal region of the probe and static pressure outside requires a too large area for a complete probe purging. For this reason, a modification has been introduced to the basic design. In order to improve the purging system, one can increase the pressure difference between the internal region of the probe and the region outside. The pressure difference can be locally modified with a converging duct. The converging duct, expanding the flow, generates a local decrease of pressure,

increasing purging hole effectiveness. In order to achieve the maximum effect, the purging hole should be located immediately adjacent to the discharge section of the converging duct.

Basing on the above considerations, a first preliminary conceptual design of probe with a converging duct was developed. The converging duct is manufactured inside the stem, in its terminal part. Fig. 1.5 is a schematic representation of such probe and its functioning.
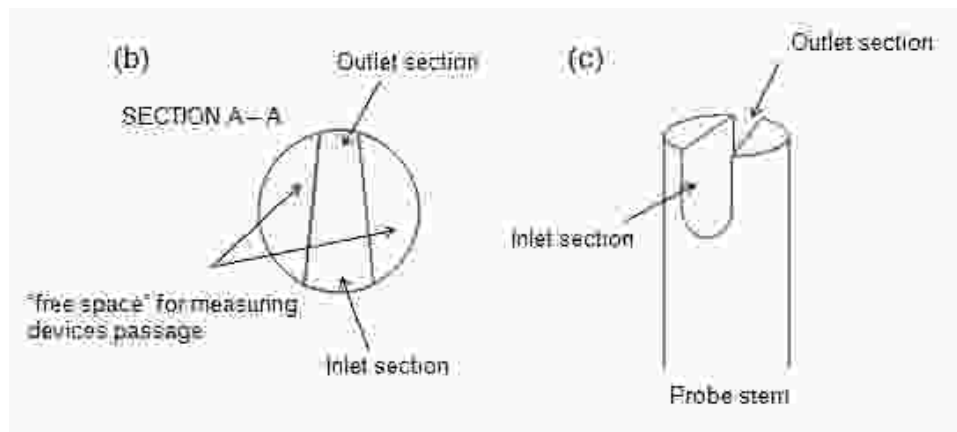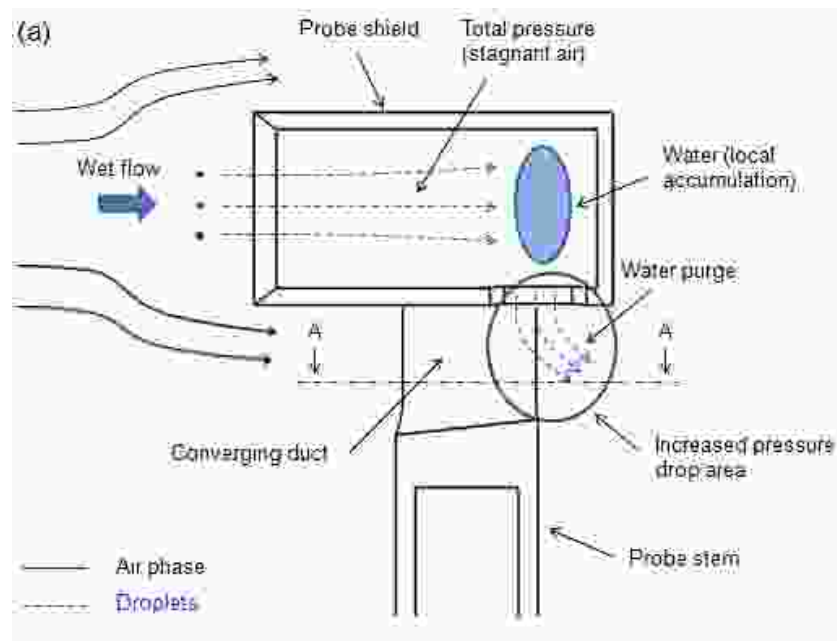
Figure 1.5: Conceptual design of a probe with a converging duct manufactured inside the stem: (a) schematic representation of probe functioning; (b) section A – A; (c) stem axonometric view.

Fig. 1.6 is a 3D CAD drawing of the probe conceptual design.
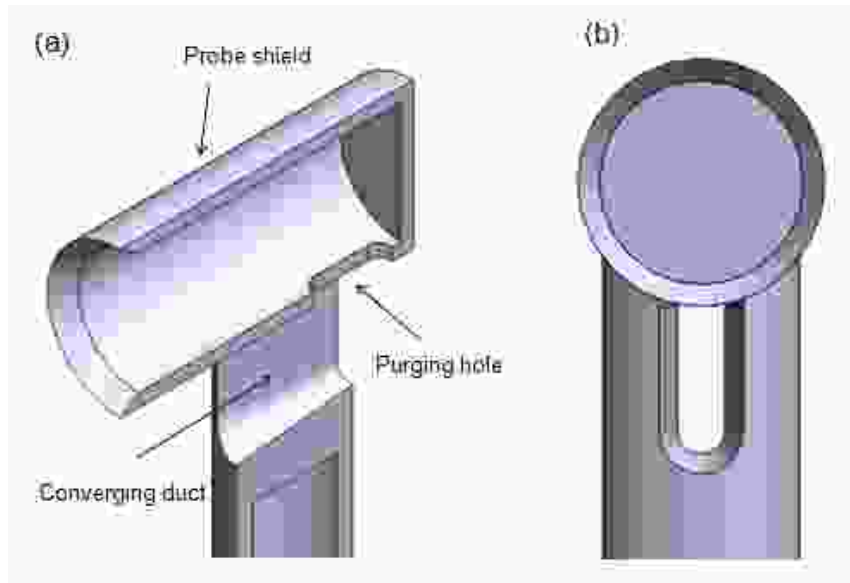
Figure 1.6: Conceptual design of a probe with a converging duct manufactured inside the shield (3D CAD drawing): (a) axonometric view, section; (b) front view.

The conceptual design represented in Figs. 1.5 and 1.6 presents some problems and constraints:

- The shape of the converging duct, together with its position and area ratio, are constrained by the stem geometry.
- The design allows for one single purging hole.
- The purging hole position is constrained by the geometry of the stem and by its position.
- The terminal section of the stem must be provided with some space for the passage of the measuring devices and sensors (Fig. 1.5 b).
- The reduced section of the stem in its terminal part can lead to some structural problems.

A lot of efforts and calculations are required in order to obtain the best solution in terms of area ratio, geometry of purging hole and manufacturing aspects. Furthermore, due to the stem shape and geometry, the probe is not suitable for a miniaturization (there is not enough space for measuring devices passage inside the stem). In order to overcome these limits, a new conceptual design of probe was developed.

The new conceptual design is based on the same principle of operation, even if the converging duct is located on the external wall of the shield, as an appendix. It can be welded to the shield or manufactured as a one piece, for example with a sintering process. The probe is designed with two symmetrical converging ducts and purging holes; this solution ensures satisfying structural and fluid mechanics stability. The new design offers several advantages:

- The shape of the converging duct and its area ratio are not constrained by the stem geometry.
- The purging holes number can be set to two (the probe can work with higher liquid amounts).
- The purging hole position is not constrained by the stem geometry.
- The stem can be a standard component, with an annular section (The internal part of the stem can be used for the passage of the measuring devices).
- The probe is more suitable for miniaturization.

Fig. 1.7 represents a schematic functioning of the new probe design.
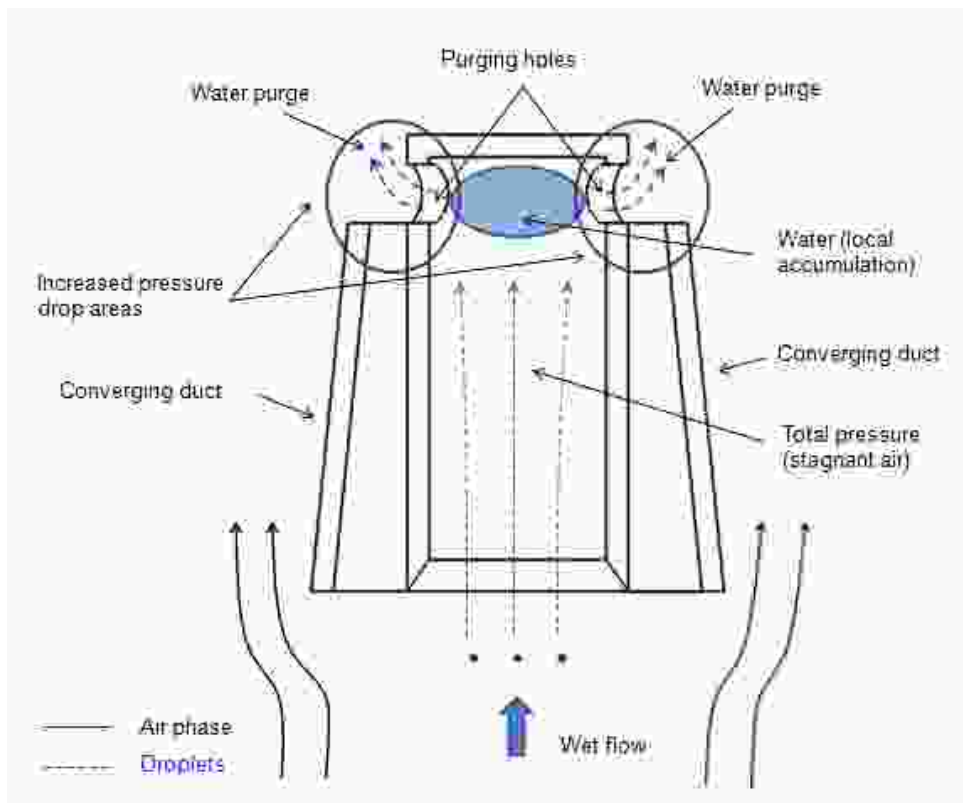
Figure 1.7: Schematic functioning of the probe with external converging ducts.

Fig. 1.8 represents a conceptual design of the new configuration of probe:
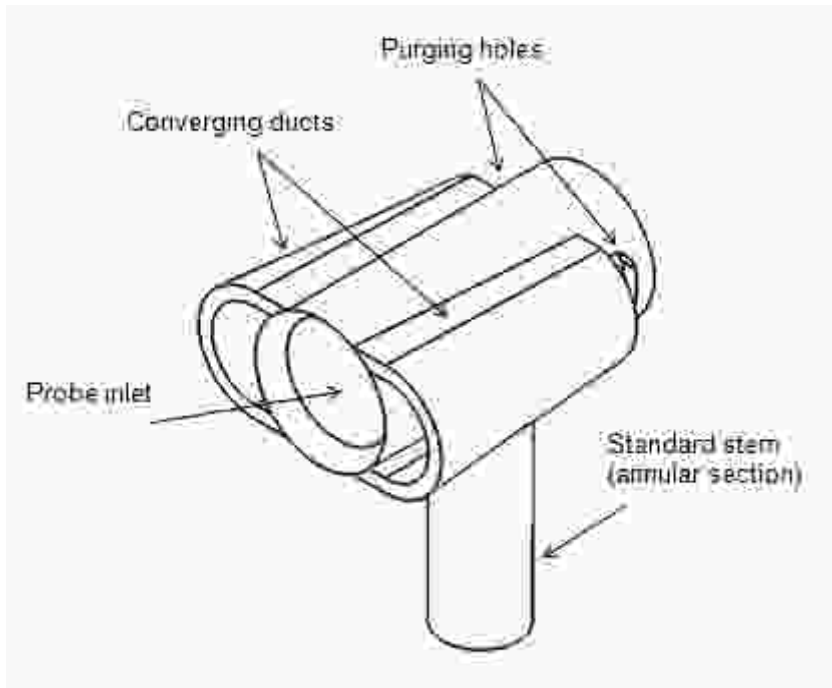
Figure 1.8: Conceptual design of the new configuration of probe.

As pointed above, the new design of probe offers several advantages. For this reason, this research activity focused mostly on this solution.

The converging ducts located on the external wall of the shield, as two appendices, represent a good solution; however, some structural or manufacturing problems may occur in the region where the converging ducts are joined to the shield, especially if the probe needs to be miniaturized. Starting from the new probe configuration, an alternative design was developed. The two probes work in the same way. The converging ducts are manufactured inside the shield, starting from an elliptical shape. This configuration of probe is easier to manufacture. The shield is manufactured as a one piece and the welded parts are avoided. However, the frontal area of the shield and its mass are greater than those of the other configuration. A higher value of the frontal area leads to higher values of mechanical stress. The blockage in the main flow is also greater. The mass of the shield is related to probe dynamical response. From these considerations it emerges that there is no best configuration for all the cases. Starting from the operating conditions and the manufacturing process, one can select the best design. Fig. 1.9 is a schematic comparison between the basic configuration of probe with external converging ducts and the alternative

design discussed above. Since the stems are standard components, only the shields are represented.
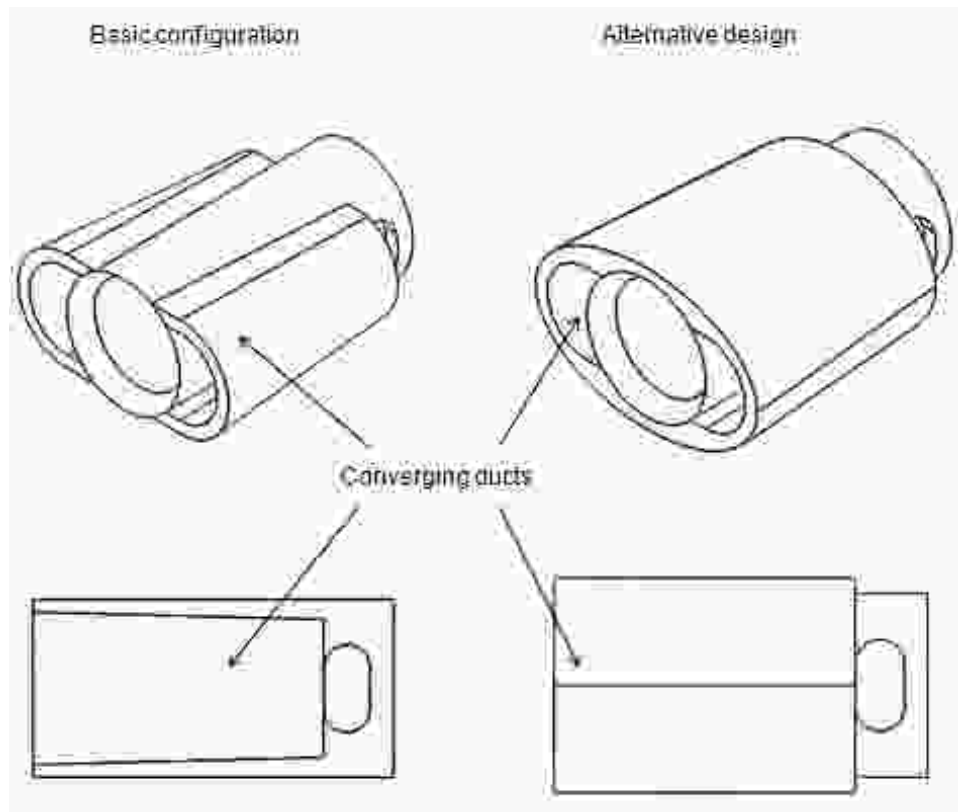
Figure 1.9: Comparison between basic and alternative probe design.

As emerges from fig. 1.9, the two designs are very similar. The only difference relates to how the converging duct concept is realized.

Once the conceptual design of the probe is clear, it's important to understand how the total pressure is measured. The total pressure of the gas phase can be measured by a pressure tube, located inside the shield, near probe inlet. The pressure tube performs a static measurement in total conditions. The total conditions of the gas phase are achieved through flow deceleration by the shield. In order to reduce tube flooding by droplets direct impact, the pressure tap is directed orthogonally to the flow. A pressurized gas flow, for example air or nitrogen, should also be periodically injected into the tube. This operation, which requires a temporary interruption of the measurement, ensures a complete tube purging. Fig. 1.10 represents a pressure probe shield, with a pressure tube in its internal region.
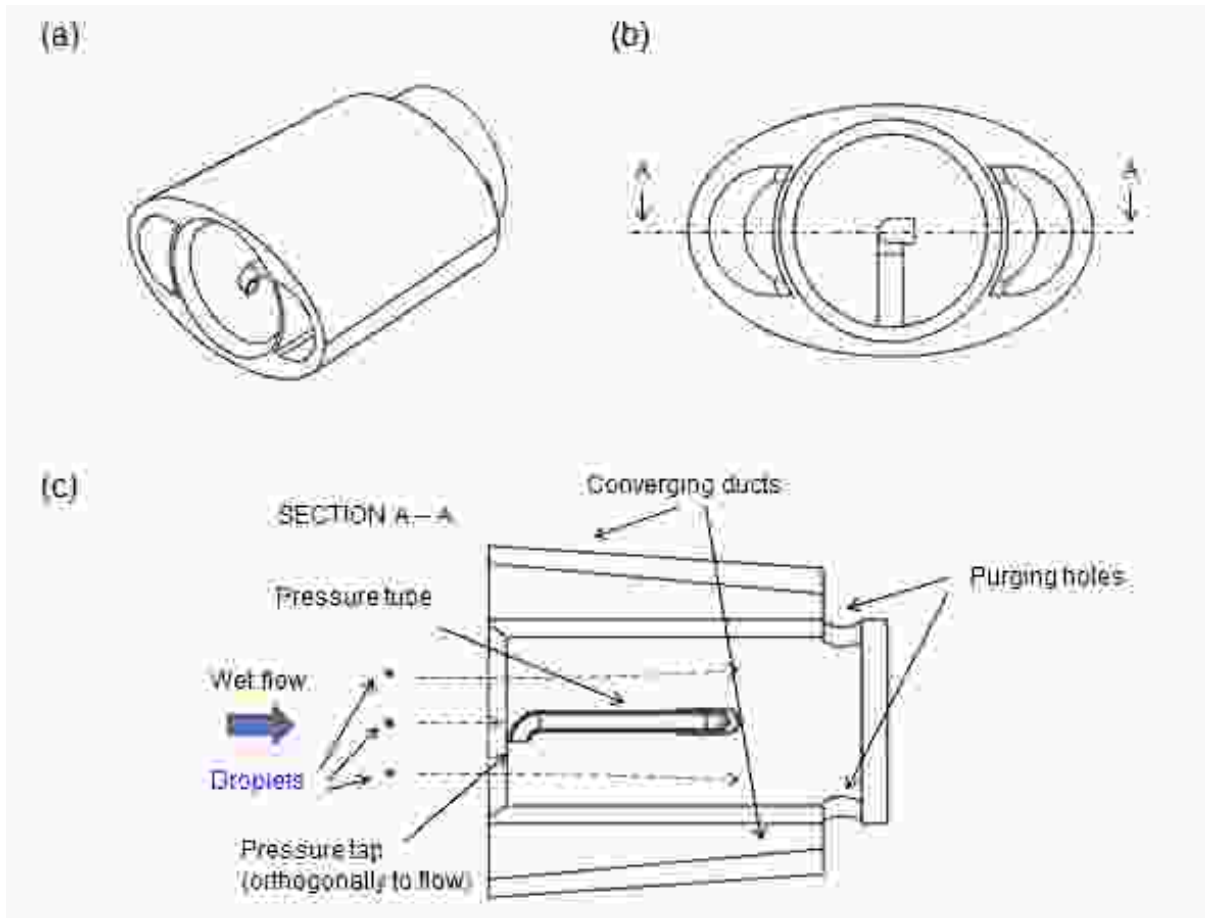
Figure 1.10: Conceptual design of a total pressure probe (shield) with the pressure tube in its internal region: (a) axonometric view; (b) front view; (c) section A – A.

As previously discussed, Dussourd and Shapiro [23] pointed that the momentum exchange between the droplets and the gas phase in the internal region of the probe leads to a longitudinal distribution of total pressure inside the shield (Fig. 1.2), which depends on probe geometry and flow conditions. In order to verify this effect, a second pressure tap can be located inside the shield, behind the other. Fig 1.11 represents a pressure probe shield, with two pressure tubes in its internal region. A probe with two or more pressure tubes inside is suitable to study such effect. However, some space for the tubes is required. For this reason, the probe results unsuitable for miniaturization.
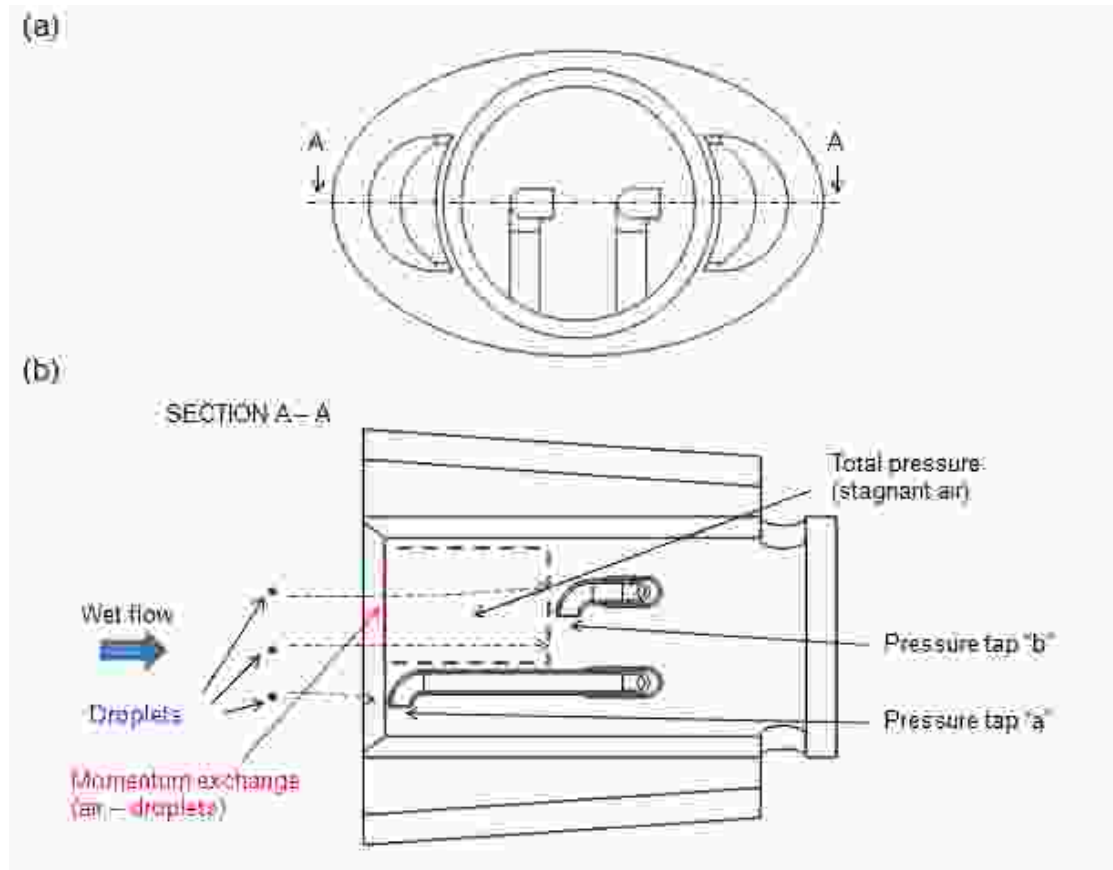
Figure 1.11: Conceptual design of total pressure probe (shield) with two pressure tubes in its internal region: (a) front view; (b) section A – A.

1.2 Total temperature probes

The conceptual design proposed for total pressure probes can be extended to total temperature probes, introducing some modifications. The measurement of total temperature requires stagnation conditions of gas phase around the sensing element but also a controlled and suitable thermal heat transfer between the gas flow and the sensor. This condition can be provided by one or more vent holes, which control the velocity of the gas phase inside the shield. Since the gas conductivity is relatively low, the vent holes must be designed in order to achieve a moderate velocity inside the shield. In such conditions the sensor exchanges effectively heat with the flow under forced convection condition; the total temperature error caused by the not stagnation conditions is minimized. A device is also required to protect the sensing element from droplets direct impact. If the sensing element comes in contact with the droplets, it will measure a temperature which

tends to the temperature of the liquid phase. A mini – shield or multiple mini – shields can be used at this proposal. The mini-shield is located in front of the sensor and it has a double function. It protects the sensor from droplets direct impact and it introduces some turbulence through a vortex shedding mechanism. The turbulence increases the thermal exchange between the sensor and the gas flow. The mini – shield, depending on its geometry, influences also the amount of water which flows into the shield. This effect must be considered during the probe detailed design. Fig 1.12 represents the conceptual design of a total temperature probe with two mini – shields.
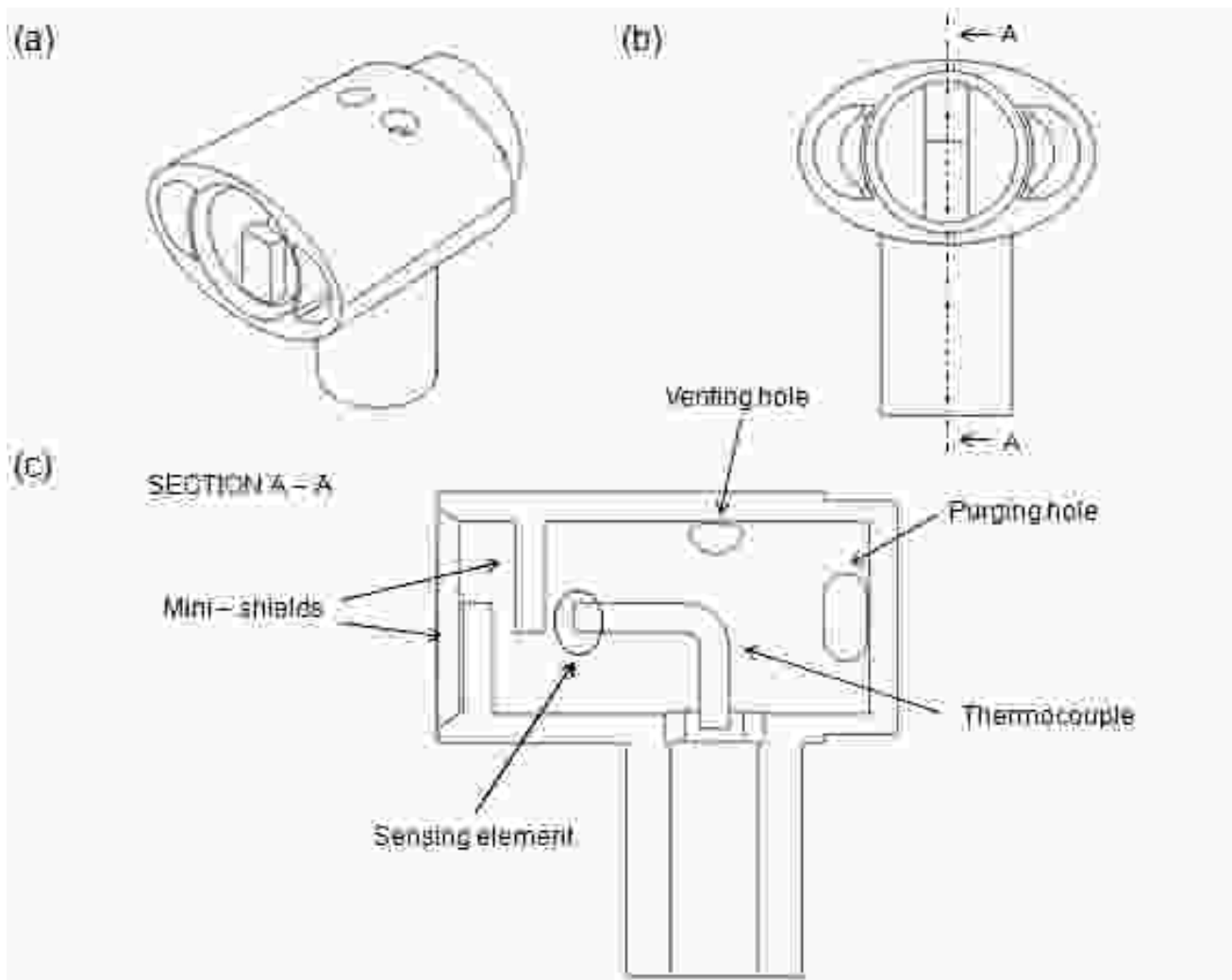
Figure 1.12: Conceptual design of a total temperature probe: (a) axonometric view; (b) front view; (c) section A–A.

Fig. 1.13 represents two alternative designs for the mini – shield. The probes represented in Fig. 1.13 have only one mini shield. This solution is more compact and suitable for probe miniaturization, even if it ensures a less protection of the thermal element.
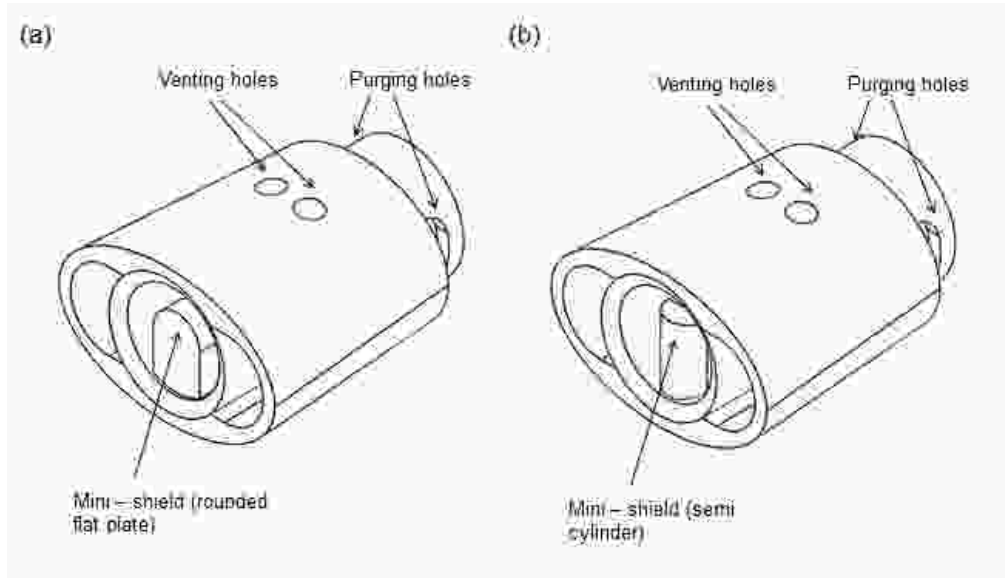
Figure 1.13: Alternative designs for mini – shield: (a) flat plate; (b) semi cylinder.

In the present chapter the most important aspects related to the design of total pressure and total temperature probes for wet gas conditions have been discussed. Basing on these considerations, some conceptual designs of probe have been presented. All the design discussed have also been patented [31]. The analytical model for probes detailed design will be discussed in Chapter 2.

Chapter 2

Step by step design

The conceptual design of probes discussed in the previous chapter is the starting point for the development of the detailed design. The detailed design is performed with an analytical model, which is the main topic of the present chapter. The model is based on the specific application operating conditions and on a first attempt geometry. It provides a complete analysis of the expected probe performance, from the fluid dynamics and the structural point of view. After the first iteration, the user can change the value of the design parameters, until the required performance are reached. The model has been implemented into an EES [32] code, which is provided with extensive and reliable libraries for ideal gases and real fluids properties. By this way it is possible to calculate the fluid properties (including speed of sound, density, viscosity, etc.) avoiding or reducing the use of ideal gas and real fluid relations. The design tool aims to become a reliable instrument for wet tolerant probes design. The model architecture, together with its input variables, main hypotheses and equations, are discussed in the present chapter.

2.1 Input variables

The fundamental input variables relate to wet gas operating conditions and probe geometry. This set is listed in Table 2.1.

Table 2.1: Wet gas operating conditions – Main input variables

Gas flow	
Total pressure	$P_{0,g}$
Total temperature	$T_{0,g}$
Mach number	Ma_g
Droplets	
Reference diameter	d_d
Mixture	
Liquid Volume Fraction	LVF

As in the literature on wet gas compression [4-6, 8, 11], the homogeneous flow model is used to define the properties of the mixture. The central assumption of this model is that the two fluids have the same velocity and mix well. They can be treated as if there is only one fluid. In the present work the temperature of the droplets is also assumed to be equivalent to that of the gas phase.

The most important geometrical features relate to the following elements (Fig. 2.1):

- Shield
- Stem
- Purging holes
- Converging ducts
- Vent holes (total temperature probe)
- Mini shield (total temperature probe)
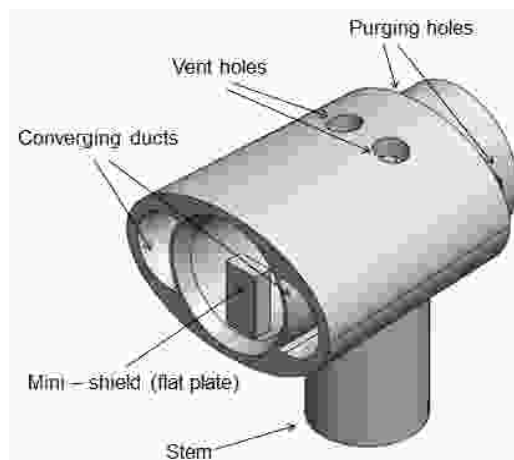
Figure 2.1: Wet tolerant probe (total temperature) – Overview

The most important parameters related to probe geometry are presented in table 2.2.

Table 2.2: Probe geometry – Main input variables

Shield (overview)	
Internal diameter	$d_{s,i}$
Length	L_s
Frontal area	$A_{s,fr}$
Lateral area	$A_{s,lat}$
Converging ducts	
Inlet area	$A_{cd,in}$
Outlet area	$A_{cd,out}$
Vent holes	
Number of vent holes	Z_{vh}
Diameter	d_{vh}
Purge holes	
Number of purge holes	Z_{ph}
Area	A_{ph}
Mini shield	
Frontal Area	A_{ms}
Stem	
External diameter	$d_{st,e}$
Internal diameter	$d_{st,i}$
Height	h_{st}
Pressure tube	
External diameter	$d_{ps,e}$
Internal diameter	$d_{ps,i}$
Thermocouple	
Diameter	d_{ts}

The geometrical parameters listed above are the basic inputs for probe calculation. Other input variables refer to mini shield shape and position, vent holes and purging holes position, etc. The parameters listed in table 2.2 refer to probe configuration with the standard stem and the converging ducts integrated in the shield. However, such parameters are suitable both for the basic and the alternative designs (Fig. 1.9). The other configuration of probe (converging duct integrated in the stem) represents a worse solution, even if the model can be simply adapted to it.

2.2 Fluid dynamics model of the gas-liquid flow

The present section describes the main steps of probe calculation from the fluid dynamics point of view. Starting from the operating conditions, one can calculate the main physical properties of the gas phase and the droplets, together with those of the mixture. The physical properties of the fluids and the mixture, together with the first attempt geometry, lead to the calculation of probe performance. After the first iteration, the user can change the value of the design parameters until the required performance are reached. Once the geometry has been obtained, one can perform a parametric analysis in order to characterize probe performance in off design conditions. The most important steps of probe calculation are the following:

- Physical properties of flows and mixture
- Liquid amount inside the shield
- Purging holes capability
- Vent hole sizing
- Gas velocity inside the shield
- Recovery factor of probe

2.2.1 Physical properties of flows and mixture

The physical properties of the two flows and the mixture can be calculated from the input operating conditions. Starting from the total pressure, the total temperature and the Mach number of the gas phase, one can calculate its static pressure and its static temperature with the classical relations of compressible flows [33-35]:

$$\frac{P_{0,g}}{P_g} = \left[1 + \frac{\gamma-1}{2} Ma_g^2\right]^{\frac{\gamma}{\gamma-1}} \tag{2.1}$$

$$\frac{T_{0,g}}{T_g} = 1 + \frac{\gamma-1}{2} Ma_g^2 \tag{2.2}$$

Referring to equations 2.1 and 2.2, the pressure must be expressed in Pascal and the Temperature in Kelvin. The static pressure is the same for the two phases. The static

temperature of the liquid phase is assumed to be equivalent to the gas phase one. The density of the two fluids can be computed with the internal libraries of EES. The required inputs are the type of fluid, the static pressure and the static temperature. Once the density of the two fluids has been estimated, one can calculate the density ratio δ, which is a significant parameter:

$$\delta = \frac{\rho_l}{\rho_g} \tag{2.3}$$

The density ratio indicates how the flow is homogeneous. δ and *LVF* can be used to compute the *LMF* of the mixture:

$$LMF = \frac{LVF \cdot \delta}{1 + (\delta - 1) \cdot LVF} \tag{2.4}$$

Starting from *LVF* and density of the two phases, one can calculate the density of the mixture ρ_h:

$$\rho_h = GVF \cdot \rho_g + (1 - GVF) \cdot \rho_l \tag{2.5}$$

The velocity of the gas phase can be computed from the Mach number, which is an input variable, and from the speed of sound, which can be estimated with the standard equations of compressible flows [33, 34] or with the EES internal libraries:

$$v_g = Ma_g \cdot a_g \tag{2.6}$$

Since the homogeneous flow model is used to characterize the mixture [4-6, 8, 11], the velocity of the liquid phase is assumed to be equivalent to that of the gas phase. As suggested in [4-6, 8, 10-11], the speed of sound of the mixture can be calculated from Wood's correlation [7]. It depends on *GVF, a_g* and δ:

$$a_h = \frac{a_g}{1 - LVF} \sqrt{\frac{1 - LVF}{1 + LVF(\delta - 1)}} \tag{2.7}$$

Once the sound speed of the mixture has been calculated, one can estimate its Mach number Ma_h:

$$Ma_h = \frac{v_h}{a_h} \tag{2.8}$$

Starting from the physical properties calculated above, one can perform probe design.

2.2.2 Liquid amount inside the shield

The liquid amount that flows into the shield depends on probe geometry and flow conditions. It can be calculated as follows:

$$\dot{m}_{l,s} = LVF \rho_l v_h A_s kf \tag{2.9}$$

The shield internal area A_s can be computed from its internal diameter, which is an input variable. The correction factor f is introduced to take into account the presence of the mini-shield for total temperature probes. It will be discussed in the following pages. The collection efficiency k is the ratio between actual and ideal capture rate of droplets. The ideal capture rate assumes that droplets trajectories are straight lines. k is defined as follows:

$$k = \frac{N_{actual}}{N_{ideal}} \tag{2.10}$$

Dussourd and Shapiro [23] pointed that the collection efficiency depends on two dimensionless parameters, related to probe geometry and flow conditions. In the present work the first parameter is called Shapiro's Reynolds number Re_{Sh}. It is defined as follows:

$$Re_{Sh} = \frac{\rho_l v_l d_d}{\mu_g} \tag{2.11}$$

The second parameter, the Obedience number Ob, is a measure of how closely the droplets trajectory obeys the gas motion:

$$Ob = \frac{3\rho_g d_s}{4\rho_l d_d} \tag{2.12}$$

Dussourd and Shapiro proposed an interesting diagram. They plotted the complement to unity of the collection efficiency (*1-k*) as a function of the two dimensionless numbers described above (Fig. 2.2). They distinguished between the case of a thin walled tube and a thick walled tube. The first means that the ratio between the internal and the external diameter of the shield tends to a unit value. The second means that such parameter tends to be 0. The present work refers to the first case
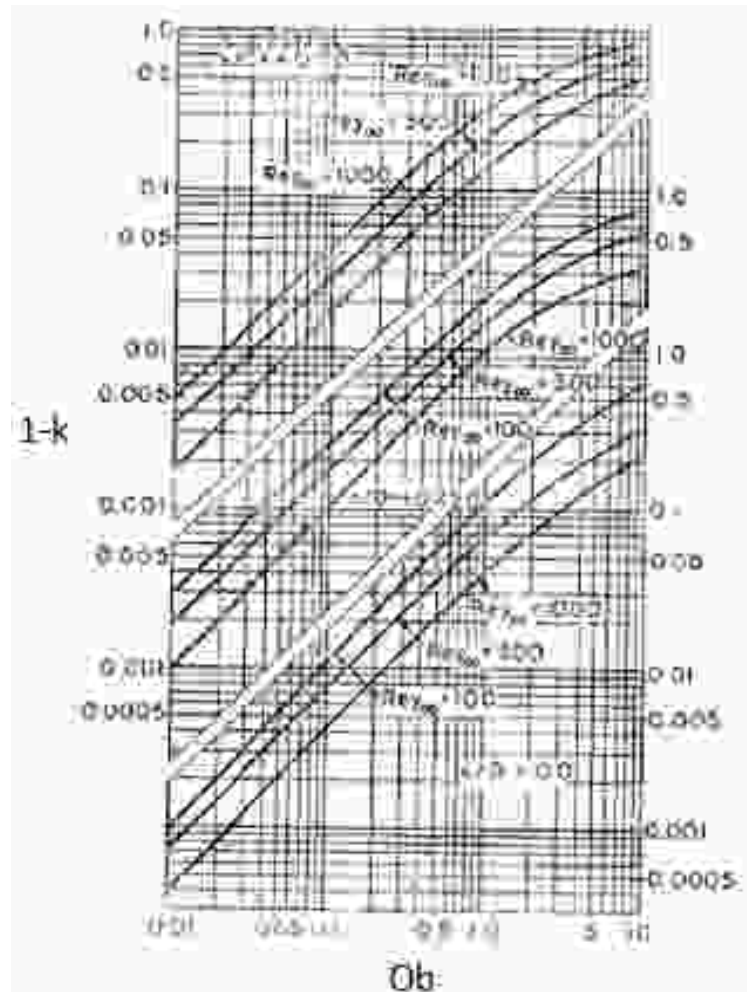
Figure 2.2: Uncaptured fraction of droplets (1-k) as a function of Re_{sh}, Ob and axial position inside the shield – Thin walled tube (adapted from [23]).

In order to better understand Fig. 2.2, the symbol $Re_{y\infty}$ corresponds to Re_{Sh}, which has been previously defined. *x/D* represents the longitudinal distance between a general position inside the shield and probe mouth. The present application focuses on the value of *k* at probe inlet (*x/D≈0*). From Fig 2.2 emerges that *k* increases if Re_{Sh} increases too. This is due to the fact that a higher Re_{Sh} leads to a larger droplets inertia. The droplets with high inertia

tend to maintain their straight trajectories without being affected by the gas phase. The value of *k* decreases if *Ob* increases. In fact, higher values of *Ob* correspond to both high shield and low droplets diameters. In the present work, the operating conditions and the geometry of probes lead to unit values of *k*. The same results can be obtained using another approach, based on Stokes number [36]

A correction factor *f* is also introduced in the calculation of $\dot{m}_{l,s}$ to take into account the presence of the mini shield for total temperature probes. Depending on its shape, the mini shield reduces the amount of water that flows inside probe shield (Fig. 2.3)
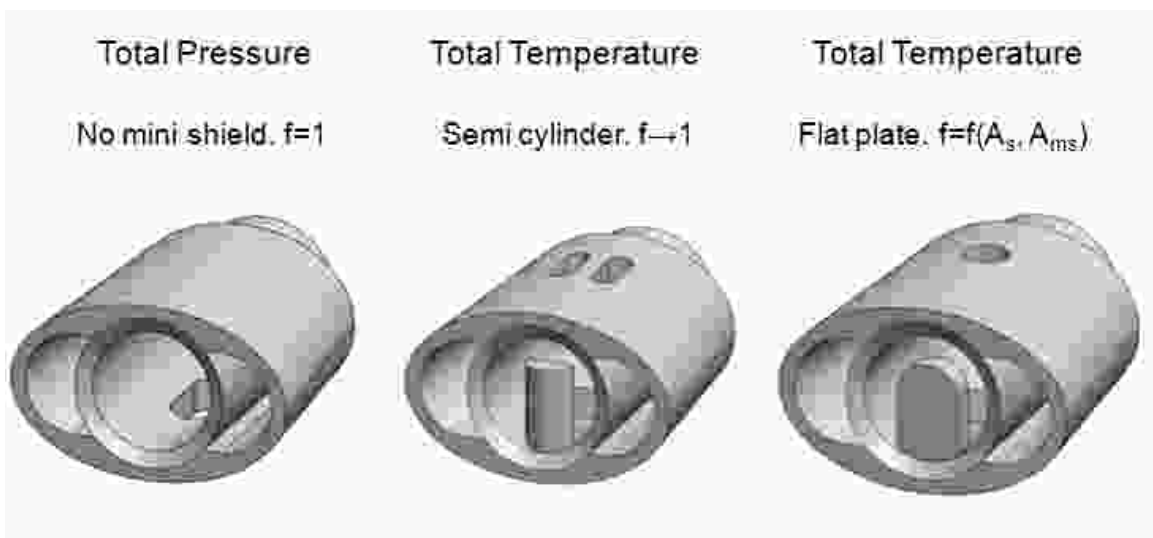
Figure 2.3: Mini shield shape and associated correction factor: examples.

A semi-cylindrical shape has the effect of driving droplets inside the shield. In this case, *f* tends to assume a unit value. If the mini shield has a flat-plate shape, a fraction of droplets is not captured by the shield (*f<1*). Since the collection efficiency tends to a unit value and the droplets have right trajectories, one can preliminary evaluate the correction factor as a function of the ratio between mini shield and probe inlet area. A more accurate estimation of *f* can be performed with an experimental characterization of the shield or with a numerical analysis.

2.2.3 Purging hole capability

The captured mass flow rate of water is a fundamental parameter for probe design. After calculating it, one can evaluate the purging capability of the probe. The first step is

the calculation of static pressure at converging ducts outlet. The nozzle calculation refers to the classical equations of isentropic flows in variable area ducts [33-35]. Once the static pressure at nozzle discharge has been calculated, one can compute the pressure difference between the internal and the external region of the shield ΔP_{suc}, where the purging hole is located.

$$\Delta P_{suc} = P_{0,g} - P_{cd,out} \tag{2.13}$$

Once ΔP_{suc} is known, one can estimate the purging capability similarly to the case of water discharge from a tank. The calculated pressure drop (eq. 2.13) can be converted into an equivalent water column height:

$$h_l = \frac{\Delta P_{suc}}{g \rho_l} \tag{2.14}$$

The liquid discharge velocity can be computed with the Torricelli's law:

$$v_{dis} = \sqrt{2 g h_l} \tag{2.15}$$

The water flow rate that can be purged from the shield, which is called purging capability $\dot{m}_{l,ph}$, depends on the number of purging holes and their area, the liquid discharge velocity, the liquid density and a discharge coefficient:

$$\dot{m}_{l,ph} = Z_{ph} C_{l,ph} \rho_l v_{dis} A_{ph} \tag{2.16}$$

As discussed in the previous chapter, Z_{ph} is set to two. Concerning $C_{l,ph}$, a standard value of 0.60 [37-38] is assumed.

In order to define the purging characteristic of the probe, a non-dimensional coefficient is introduced. The purge coefficient *PC* represents the ratio between the purging capability and the amount of water that flows into the shield:

$$PC = \frac{\dot{m}_{l,ph}}{\dot{m}_{l,s}} \tag{2.17}$$

PC, which depends on probe geometry and operating conditions, assumes a value between 0 and 1. A unit value denotes a complete elimination of liquid from the shield. If *PC* is lower than 1, the purging capability of the probe is not sufficient and the shield becomes flooded. If the purging capability is too high, the purge is complete (*PC=1*), but a certain amount of gas flows through the purging hole. The velocity of the gas into the shield increases, leading the sensing element to measure values closer to the static pressure or temperature, instead of the total value. The model has an internal routine for the calculation of *PC*, which limits its value to 1 and gives a warning message if the purging system is oversized. The routine has the following architecture:

$$if \begin{cases} \dot{m}_{l,ph} \leq \dot{m}_{l,s} \Rightarrow PC = \dfrac{\dot{m}_{l,ph}}{\dot{m}_{l,s}} & (2.18a) \\[3mm] \dot{m}_{l,ph} > \dot{m}_{l,s} \Rightarrow PC = 1 & (2.18b) \end{cases}$$

If the purging hole is oversized (eq. 2.18b), the internal routine imposes the following condition:

$$\dot{m}_{l,ph} = \dot{m}_{l,s} \qquad (2.19)$$

In such conditions, it is important to calculate the amount of gas flowing into the shield, which affects the recovery factor. The first step is the calculation of the purging hole net area for liquid phase passage:

$$A_{l,ph} = \frac{\dot{m}_{l,ph}}{Z_{ph} C_{l,ph} \rho_l v_{dis}} \qquad (2.20)$$

Since the purge hole is oversized, a net passage area is available for the gas phase:

$$A_{g,ph} = A_{ph} - A_{l,ph} \qquad (2.21)$$

Finally, one can calculate the gas mass flow rate through the purge hole using the classical relations for isentropic nozzle gas flow [33-35]:

$$\dot{m}_{g,ph} = C_{g,ph} A_{g,ph} \rho_{cd,out} \sqrt{2\left(\frac{\gamma}{\gamma-1}\right)\frac{P_{0,g}}{\rho_{0,g}}\left(1 - \frac{P_{cd,out}}{P_{0,g}}^{\frac{\gamma-1}{\gamma}}\right)} \qquad (2.22)$$

The discharge coefficient of the gas phase $C_{g,ph}$ is influenced by the flow conditions inside the shield and in the local external area around the purge hole. The literature about discharge coefficients of film cooling holes applied in the gas turbine hot sections [39-43] gives some useful indications to select suitable values.

2.2.4 Vent holes sizing

Total temperature probes must be provided with one or more vent holes, which control the velocity of the gas phase inside the shield. For standard probes, NASA [18] suggests a value of 0.5 for the ratio between vent holes and shield inlet area. The value proposed by NASA was considered too high for wet tolerant probes, where one must also take into account the amount of air that flows through the purging hole during off-design conditions. For this reason, lower values (between 0.25 and 0.35) should be used. After setting this parameter, one can calculate the total vent area and the gas mass flow induced into the shield by vent holes:

$$\dot{m}_{g,vent} = C_{vh} Z_{vh} \rho_g v_h A_{vh} \qquad (2.23)$$

As previously pointed, C_{vh} can be estimated referring to discharge coefficients of film cooling holes applied in the gas turbine hot sections [39-43]. As suggested in [21], the undisturbed velocity and the density of gas phase can be used to calculate $\dot{m}_{g,vent}$.

2.2.5 Gas velocity inside the shield

One of the most significant parameters for probe characterization is the velocity of the gas phase inside the shield $v_{g,s}$, which influences the recovery factor. It depends on probe type, probe geometry and operating conditions. In order to perform a correct evaluation of this parameter, one must distinguish between total pressure and total temperature probes. In the first case there are no vent holes; the only amount of gas flow inside the shield comes from the suction effect of purging holes in off-design conditions. In the other case, the effect of the vent holes must also be considered. If a total temperature

probe works in off-design conditions, the effects of vent holes and purging holes can lead to high values of gas velocity inside the shield. This condition causes a decrease of probe performance, from the recovery factor point of view. The calculation of $v_{g,s}$ is performed by an internal routine, with the following architecture:

$$if \begin{cases} x = TPP \Rightarrow \dot{m}_{g,s} = \dot{m}_{g,ph} & (2.24a) \\ x = TTP \Rightarrow \dot{m}_{g,s} = \dot{m}_{g,ph} + \dot{m}_{g,vent} & (2.24b) \end{cases}$$

x is a string variable which makes the model able to distinguish between total pressure and total temperature probes. If $x=TPP$, the model refers to a total pressure probe. If $x=TTP$, it refers to a total temperature probe. Once the value of $\dot{m}_{g,s}$ has been calculated, one can estimate $v_{g,s}$:

$$v_{g,s} = \frac{\dot{m}_{g,s}}{\rho_{0,g} A_{s,g,net}} \tag{2.25}$$

Since total conditions of gas phase inside the shield occurs, the density of gas phase at shield inlet can be approximated with the total value. This approximation works well when the probe operates in design conditions or near them, and the gas velocity inside the shield assumes low values. If $v_{g,s}$ becomes high, the static density or an average value between total and static conditions is more suitable for the calculation.

The parameter $A_{s,g,net}$ represents the net passage area of gas phase across the shield. In order to calculate it, two steps are required. First, the sensor area must be subtracted from the shield internal area:

$$A_{s,net} = A_s - A_{bk,sens} \tag{2.26}$$

The second step relates to the calculation of a net passage area for the gas phase. $A_{s,net}$ can be theoretically divided into a passage area for the gas phase and another for the liquid phase. The homogenous flow model [4-6, 8, 11] can be used for this calculation:

$$\begin{cases} A_{s,net} = A_{s,g,net} + A_{s,l,net} & (2.27a) \\ LVF = \dfrac{A_{s,l,net} v_h}{A_{s,l,net} v_h + A_{s,g,net} v_h} & (2.27b) \end{cases}$$

Once $v_{g,s}$ has been calculated, one can compute the recovery factor.

2.2.6 Recovery factor

The recovery factor r [20, 21] is the most-important parameter for the characterization of fluid mechanics measurement probes. It is defined as the ratio between the recovered energy and the maximum energy which could be obtained from the isentropic deceleration of the gas stream. Equations 2.28 and 2.29 show the formulas for the respective cases of total pressure and total temperature probes:

$$r_{TPP} = 1 - \frac{0.5\rho_0 v_{g,s}^{\,2}}{P_{0,g} - P_g} \tag{2.28}$$

$$r_{TTP} = 1 - \frac{0.5 v_{g,s}^{\,2} / cp_0}{T_{0,g} - T_g} \tag{2.29}$$

Since total conditions of gas phase inside the shield occurs, the density and the specific heat of gas phase at shield inlet can be approximated with the total values. As for the computation of $v_{g,s}$, this is a good approximation if the probes work around design point. Otherwise, the corresponding values in static conditions or between static and total conditions are recommended.

The above paragraphs describe the most significant steps for fluid mechanics probes design. In order to design well suited probes for a wet gas environment, one must also perform a complete structural analysis, from the static, the dynamic and the fatigue point of view. The structural analysis will be discussed in the following section.

2.3 Structural calculation

The probes described in the present work operate under a harsh environment. They are subjected to static loads but also to dynamic loads, induced by vortex shedding and droplets impact. For this reason, they should have a sufficiently high static and dynamic resistance. The analytical model performs a complete structural probes verification. The most important steps of the structural analysis are the following:

- Static analysis

- Fatigue analysis

- Dynamic analysis

In order to be preliminary validated, the results of the static and the dynamic analysis need to be compared at least with a numerical calculation, which was performed during the research activity.

2.3.1 Static analysis

During its operation, the probe faces with a pressurized wet flow in motion. The flow is characterized by a certain pressure, temperature, density, velocity and liquid volume fraction. In order to avoid an excessive deformation of the probe or its breakage, a static calculation is needed. Fig. 2.4 represents a conceptual scheme of a probe during its operation.
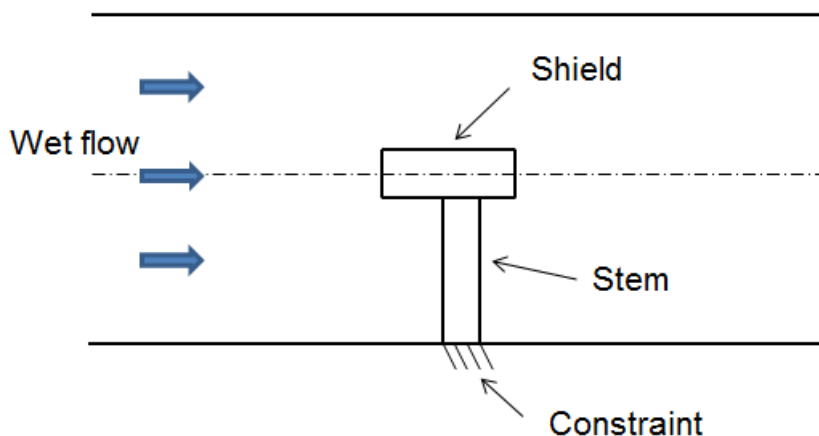
Figure 2.4: Conceptual scheme of a probe during its operation.

Fig. 2.5 represents a reference scheme for static calculation in the case of a probe parallel to flow.
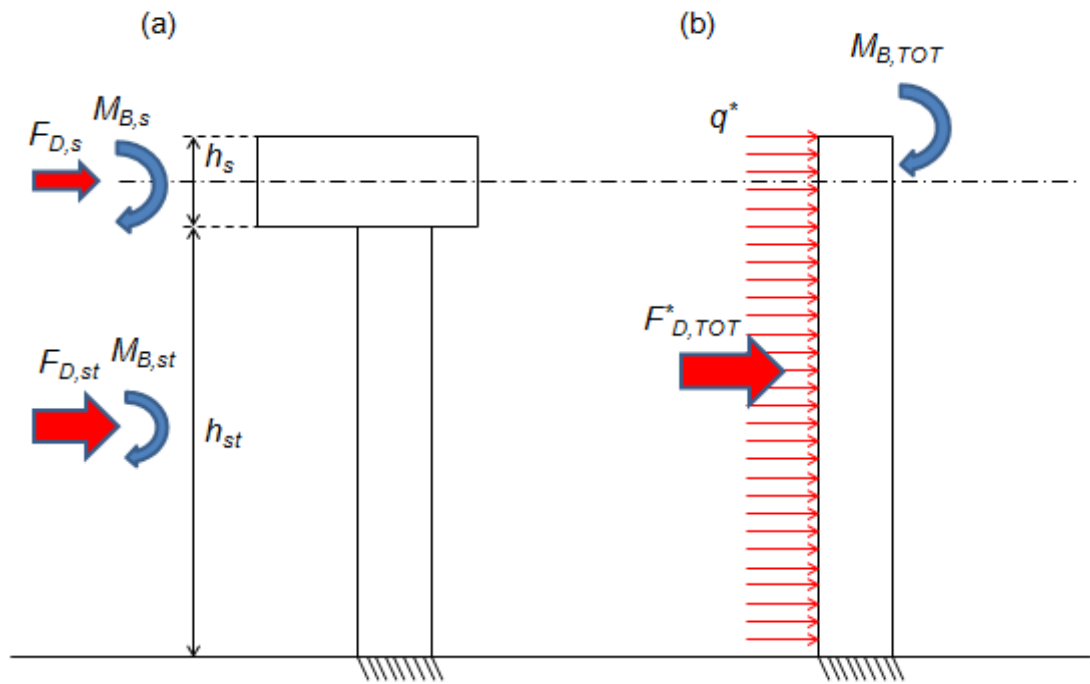
Figure 2.5: Reference scheme for static calculation, probe parallel to flow. (a) Drag forces and bending moments; (b) schematization of the probe as a jointed beam with uniformly distributed load.

The first step is the calculation of drag forces induced by the flow on the shield and on the stem (Fig. 2.5a). The classical definition of drag force can be used [33-34]:

$$F_{D,s} = \frac{1}{2} \rho_h v_h^2 C_{D,s} A_{s,fr} \tag{2.30}$$

$$F_{D,st} = \frac{1}{2} \rho_h v_h^2 C_{D,st} A_{st,fr} \tag{2.31}$$

The shield frontal area $A_{s,fr}$ is an input variable. The stem frontal area $A_{st,fr}$ can be simply calculated from its height and its external and internal diameters. A precautionary value of 1.2 can be used for stem drag coefficient [44] and a precautionary value of 2.0 for the shield, which has a not standard shape. The density of the mixture is recommended for drag forces calculation. The drag forces induce the bending moments, which are the most significant terms of mechanical stress:

$$M_{B,s} = F_{D,s} \cdot \left(h_{st} + \frac{h_s}{2} \right) \tag{2.32}$$

$$M_{B,st} = F_{D,st} \cdot \frac{h_{st}}{2} \tag{2.33}$$

In order to simplify the problem, the probe can be modeled as a cantilever beam, subjected to a fictitious uniformly distributed load q^* (Fig. 2.5b). The value of q^* can be computed from the total bending moment $M_{B,TOT}$, which is the sum between $M_{B,s}$ and $M_{B,st}$:

$$q^* = \frac{2 \cdot M_{B,TOT}}{(h_{st} + h_s)} \tag{2.34}$$

The corresponding fictitious drag force $F^*_{D,TOT}$ is defined as follow:

$$F^*_{D,TOT} = q^* (h_{st} + h_s) \tag{2.35}$$

The approach described above simplifies the problem and provides a slightly protective condition ($F^*_{D,TOT}$ is from 5 to 10% greater than the actual value).

Once $F^*_{D,TOT}$, q^* and $M_{B,TOT}$ have been estimated, one can calculate the associated structural tensions:

$$\sigma_{B,max} = \frac{M_{B,TOT}}{W_{st}} \tag{2.36}$$

$$\tau_{sh,max} = \frac{2 \cdot F^*_{D;TOT}}{A_{st}} \tag{2.37}$$

In order to verify probe structural resistance, the bending stress and the shear stress must be compared with the allowable stress of the material. The Von Mises yield criterion [45] can be used to combine the structural tensions. In the present case the equivalent tension in calculated as it follows:

$$\sigma_{VM} = \sqrt{\sigma_{B,max}^2 + 3 \cdot \tau_{SH,max}^2} \tag{2.38}$$

The allowable stress is obtained from the yield stress of the material and a Factor of Safety. In the present case, the reference material for the stem is the stainless steel AISI 304,

which mechanical properties can be found in [46]. In order to avoid any risk of breakage, a value of 3 is assumed for the Safety Factor.

$$\sigma_a = \frac{\sigma_{yld}}{FoS} \tag{2.39}$$

Finally, a Stress Factor *SF* is introduced to verify the probe static resistance:

$$SF = \frac{\sigma_{VM}}{\sigma_a} \tag{2.40}$$

The model has an internal routine which calculates the stress factor and gives a warning message if it assumes a value greater than 1. In this case one must modify the stem geometry in order to ensure probe structural resistance. After calculating the stress factor, it's important to compute also the probe maximum displacement dis_{max}:

$$dis_{max} = \frac{q^*(h_{st} + h_s)}{8EI_{st}} \tag{2.41}$$

The moment of inertia I_{st} can be calculated from the stem geometry, which has a standard annular section.

During its operation, the probe can work in a position parallel to flow or oriented with a yaw angle θ, which assumes a value between $\pm$ 35°. In order to ensure the structural resistance of the probe in all the positions, a structural verification must be performed considering its orientation. Fig. 2.6 represents three different probe positions. In the present case the stem has a symmetric geometry (annular section) and the torsion contribution is negligible for the static calculation. For these reasons, the analysis can be simplified and only two positions can be verified to ensure the static resistance of the probe in all the positions. The structural calculation was performed for the cases of probe parallel to flow and orthogonal to flow. The last condition, which is not a real case, represents the worst configuration for structural stress. If the stress factor is lower than 1 in both the cases, the static resistance of the probe is ensured.
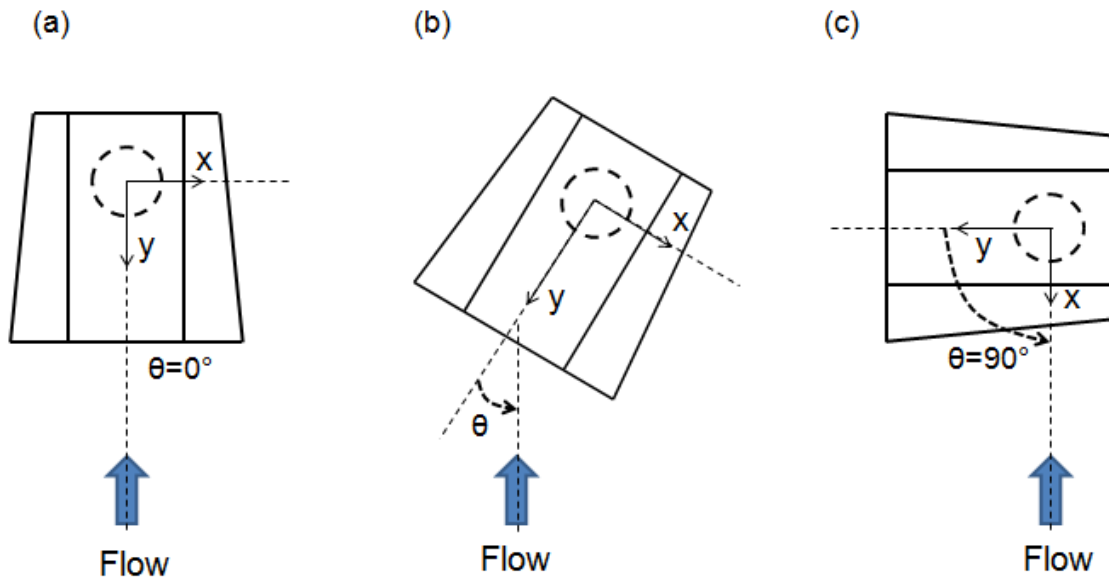
Figure 2.6: Yaw angle and probe positions. (a) Probe parallel to flow; (b) Probe oriented with a yaw angle; (c) Probe orthogonal to flow (θ=90°)

After discussing the probe static analysis, it's important to underline that also the mini shield and the sensors must be evaluated from the structural point of view. A pressurized wet flow induces high stresses and all the components must be verified. For this reason, the model performs also a simple static analysis of the mini shield and the sensors. Since the calculations are very similar to those presented above, they are not being discussed in the present work.

2.3.2 Fatigue analysis

The static analysis discussed above cannot ensure the structural resistance of the probe under dynamic loads. For this reason, a fatigue analysis is required. Probe orientation (yaw angle) has a great importance in the fatigue analysis. In fact, if θ is different from 0, the flow induces some torsion stress, which leads to a decrease in the fatigue limit of the material. The analytical model performs a complete probe fatigue analysis. It refers to the standard criteria of mechanical design under fatigue loads [45, 47-48].

Starting from the simple case of probe parallel to flow, the first step is the characterization of the fatigue load, which is a consequence of the dynamic effects induced

by the compressor. The probe is subjected to an oscillating load with a static component, which induces a fatigue stress (Fig 2.7).
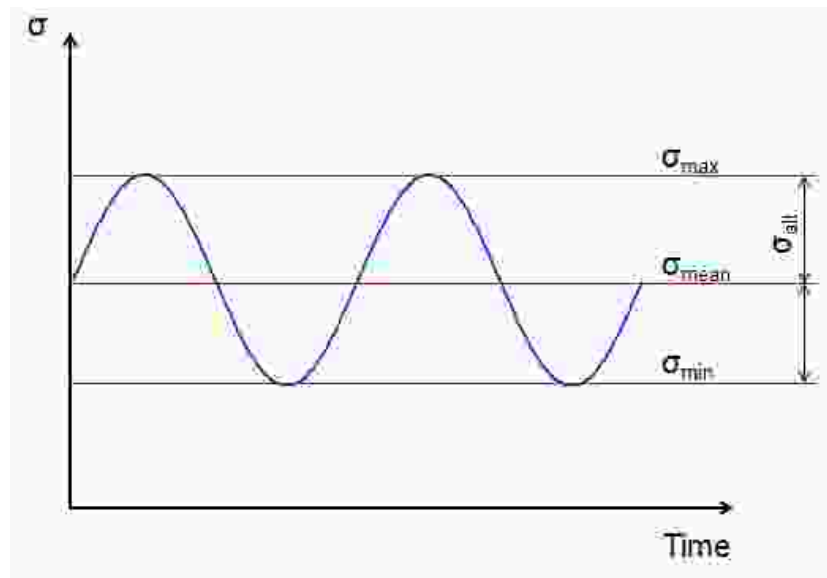
Figure 2.7: Fatigue stress induced by an oscillating load with a static component.

As suggested by GE, the maximum and minimum loads for the fatigue cycle in this case can be calculated from the nominal values of the drag forces (static calculation), increasing and decreasing them by a precautionary value of 25%. From the values of the maximum and the minimum loads one can calculate the corresponding mechanical stresses with the procedure discussed for the static calculation:

$$F_D \Rightarrow \begin{cases} F_{D,max} \Rightarrow \sigma_{max}, \tau_{max} & (2.42a) \\ \\ F_{D,min} \Rightarrow \sigma_{min}, \tau_{min} & (2.42b) \end{cases}$$

The mean and alternate components of the oscillating load can be estimated as follows:

$$\sigma_{mean} = \frac{\sigma_{max} + \sigma_{min}}{2} \qquad (2.43a)$$

$$\sigma_{alt} = \frac{\sigma_{max} - \sigma_{min}}{2} \qquad (2.43b)$$

$$\tau_{mean} = \frac{\tau_{max} + \tau_{min}}{2} \qquad (2.44a)$$

$$\tau_{alt} = \frac{\tau_{max} - \tau_{min}}{2} \tag{2.44b}$$

Bending stress and shear stress can be combined with the criterion of Von Mises, which leads to the calculation of an equivalent fatigue load:

$$\sigma_{eq,mean} = \sqrt{\sigma_{mean}^2 + 3 \cdot \tau_{mean}^2} \tag{2.45a}$$

$$\sigma_{alt,mean} = \sqrt{\sigma_{alt}^2 + 3 \cdot \tau_{alt}^2} \tag{2.45b}$$

Once the values of the mean and alternate equivalent loads have been calculated, one should compare them with the fatigue allowable stress of the stem, which can be computed from the fatigue endurance limit of the material $\sigma_{f,el}$ and some empirical coefficients K [45, 47-48]:

$$\sigma_{f,a} = \frac{\sigma_{f,el} K_a K_d K_l}{FoS_f K_s} \tag{2.46}$$

A value of 3 was selected for the fatigue factor of safety FoS_f. Depending on the case, the empirical coefficients assume different values [45, 47-48]. The coefficient K_a depends on the surface roughness of the part. In the present case, a value of 0.80, proper for machined parts, was selected. K_d represents a size factor. Since the stem has a very small diameter, a value of 1 was used. K_l depends on load type. In the present case, the probe faces with an alternate bending load, with a very small shear component. A value of 0.90 was used for this coefficient. Finally, the value of the fatigue notch factor K_s was set to 1. Starting from a 240 N/mm^2 value of $\sigma_{f,el}$, a value of 57.60 N/mm^2 was obtained for $\sigma_{f,a}$. In order to verify the probe structural resistance under fatigue loading conditions, one can use the Goodman Smith or the Haigh diagram. The results of the fatigue analysis for a practical case will be discussed in the following chapter.

As previously introduced, probe orientation must be considered in the fatigue analysis. If the yaw angle is different from 0, the flow induces some torsion stress on the probe. This condition leads to a different value of the empirical coefficient K_l, which decreases. In the present case K_l assumes a value of 0.55, leading to a $\sigma_{f,a}$ of 35.2 N/mm^2.

Since the steps of the analysis are the same as the previous one, only the calculation of loads will be discussed. In order to calculate the drag forces and the mechanical stress, the following considerations can be done:

- The drag force on the stem doesn't depend on the yaw angle. The stem is completely symmetric and its area is the same for each angle of orientation.
- The drag force on the shield depends on the yaw angle. It can be calculated as the resultant of its components parallel and orthogonal to the probe.

In order to better understand drag forces calculation, one should refer to Fig. 2.8:
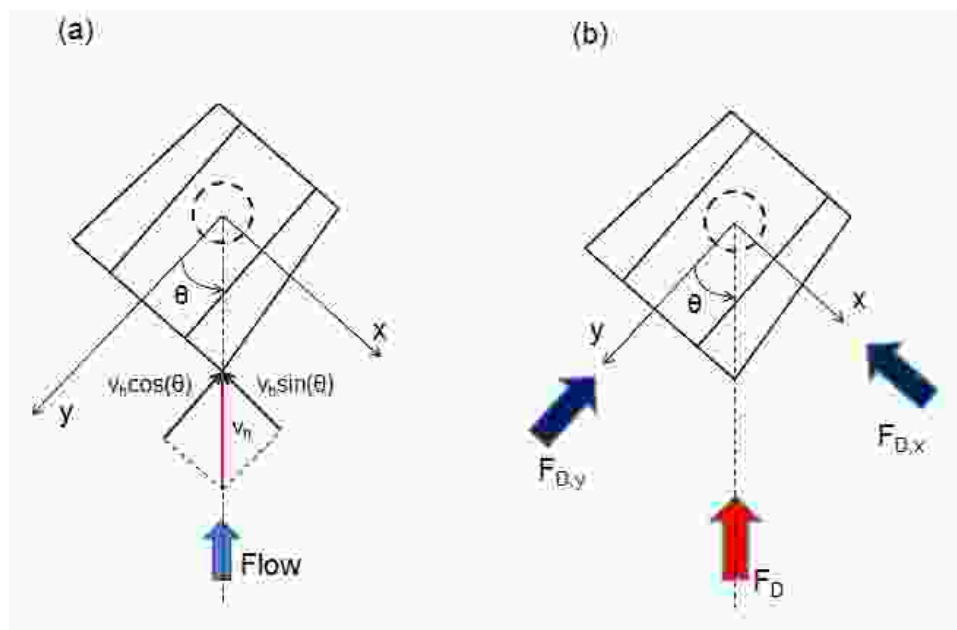
Figure 2.8: Probe oriented with a yaw angle. (a) Flow velocity and its components; (b) Drag force and its components.

The velocity of flow can be divided into a component parallel to the probe and a component orthogonal to the probe (Fig. 2.8a):

$$v_{h,y} = v_h \cos(\vartheta) \tag{2.47a}$$

$$v_{h,x} = v_h \sin(\vartheta) \tag{2.47b}$$

The velocity components calculated above lead to the computation of the corresponding drag forces:

$$F_{D,y} = \frac{1}{2} \rho_h v_{h,y} C_{D,fr} A_{fr} \qquad (2.48a)$$

$$F_{D,x} = \frac{1}{2} \rho_h v_{h,x} C_{D,lat} A_{lat} \qquad (2.48b)$$

A drag coefficient of 1.2 can be used for the shield lateral area and a value of 2.0 for its frontal area. The total drag force, which is parallel to the flow, is the resultant between its components:

$$F_D = \sqrt{F_{D,x}^2 + F_{D,y}^2} \qquad (2.49)$$

Since the center of mass of the shield doesn't coincide with stem axis, a torsion torque is generated (Fig. 2.9).
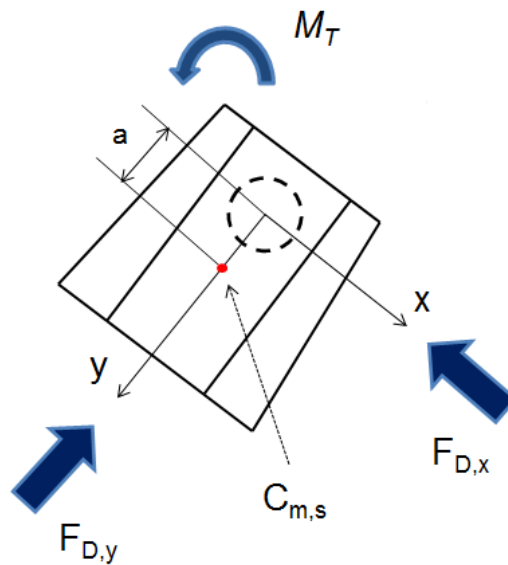
Figure 2.9: Probe oriented with a yaw angle, torsion torque.

The torsion torque depends on probe geometry and drag force:

$$M_T = F_{D,x} \cdot a \qquad (2.50)$$

From the drag forces, the bending moments and the torsion torque one can calculate the mechanical stress and verify probe mechanical strength. Since the steps of the analysis are similar to those of the previous one, they can be omitted in this section.

2.3.3 Dynamic analysis

During its operation, the probe is subjected to dynamic loads, induced by droplets impact and vortex shedding. If the frequency of these loads matches with one of the probe natural frequencies, large amplitudes can result and mechanical damage may occur. The model performs a complete dynamic analysis. The main calculations are the following:

- Frequency of vortices shed by probe shield and stem
- Frequency of droplets impact
- Natural frequency of the probe

In order to calculate the frequency of **vortices shed by the stem**, one can refer to the standard case of a circular cylinder parallel to flow [44]. The frequency of vortices depends on the velocity of flow, a characteristic dimension, and the Strouhal number *St*, which depends on Reynolds number *Re*. The calculation is referred to the gas phase:

$$\mathrm{Re}_{st} = \frac{\rho_g v_h d_{st,e}}{\mu_g} \tag{2.51}$$

In the present case the values of Reynolds number are below 200000 for probe range of operation. In such conditions, the Strouhal number can be approximately considered constant [44]. It assumes a value of 0.21. Once the Strouhal number has been calculated, one can estimate the frequency of vortices:

$$fr_{vs,st} = \frac{St_{st} v_h}{d_{st}} \tag{2.52}$$

The frequency of **vortices shed by the shield** can be calculated with the procedure described for the stem. However, due to its shape, the shield requires more attention. In order to calculate the frequency of the vortices, one can refer to the case of a rectangular cylinder. Referring to the shield with internal converging ducts, two kinds of vortices should be considered (Fig. 2.10):
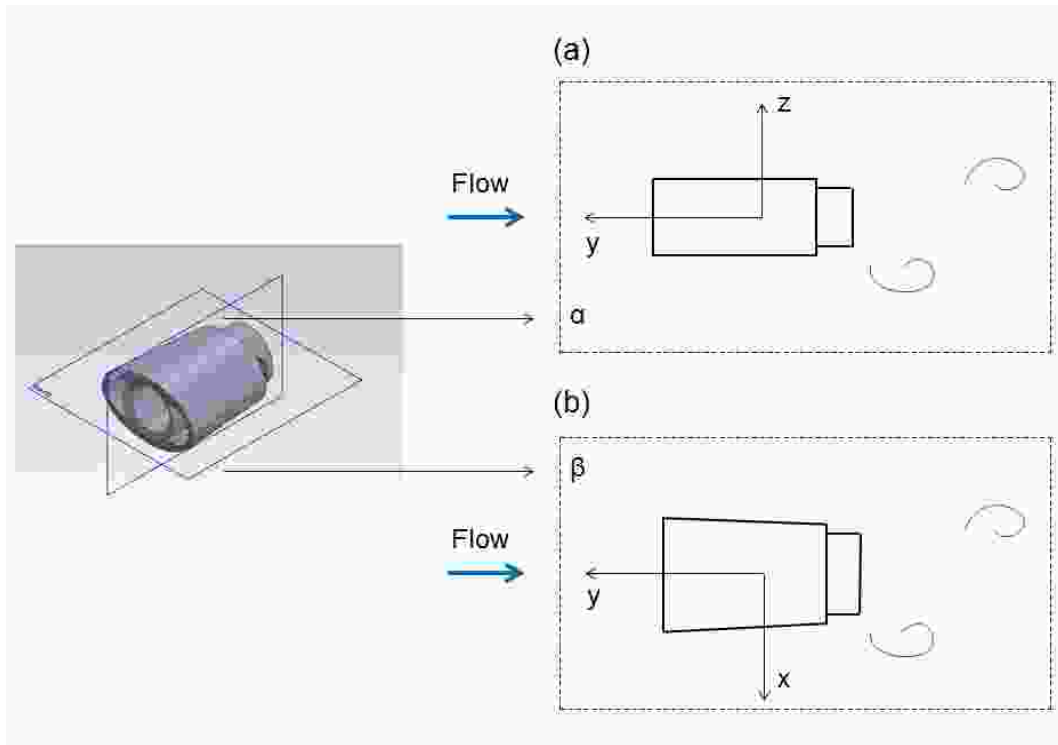
Figure 2.10: Vortices shed by the shield. (a) Plane α; (b) Plane β.

The frequency of vortices for rectangular cylinders depends on geometry and flow conditions. The most important parameter is the aspect ratio *AR,* which is the ratio between the length of the cylinder and its diameter. The Strouhal number is inversely proportional to *AR*. Once *Re* and *AR* have been calculated, one can estimate the Strouhal number [49-51], which leads to the calculation of the vortices frequency. Fig. 2.11 shows the reference parameters and the calculation of *Re* and *AR* for the vortices shed by the shield.
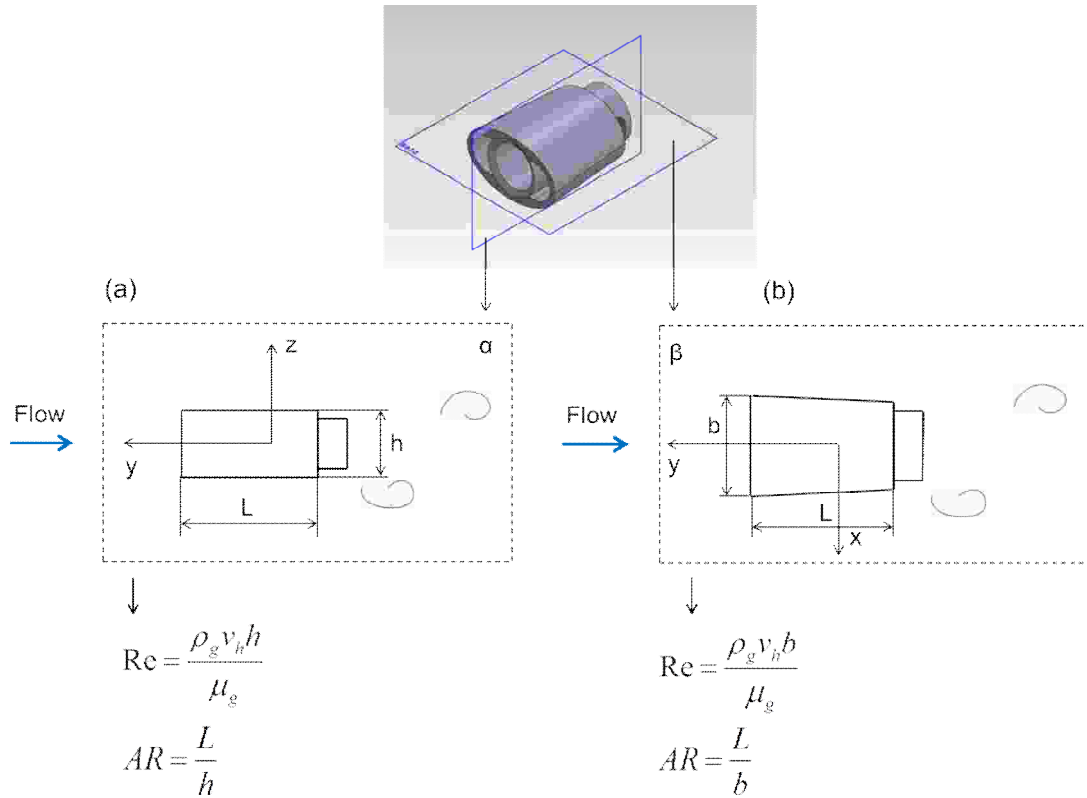
Figure 2.11: Vortex shedding induced by the shield: reference parameters calculation. (a) Plane α; (b) Plane β.

After the analysis of vortex shedding, one should consider the effects of droplets impact. Since the operating flow has a very high liquid content, one can expect a corresponding high frequency of droplets impact, far from the first natural frequency of the probes.

The **frequency of droplets impact** depends on probe geometry, liquid content and droplet diameter. Referring to a uniform droplet distribution, the frequency of droplets impact can be calculated from the amount of water that flows across a fictitious section, equivalent to probe frontal area:

$$\dot{Q}_{l,di} = LVF v_h A_{fr,di} k \qquad (2.53)$$

The frontal area $A_{fr,di}$ is the sum between the frontal areas of the shield and the stem. Starting from the value of $\dot{Q}_{l,di}$, one can estimate the droplets number impacting on the probe N_d:

$$N_d = \frac{Q_{l,di}}{Vol_d} \qquad (2.54)$$

In order to calculate the frequency of droplets impact one can assume that the droplets don't hit the probe randomly but in synchronous waves (Fig. 2.12). Each wave is composed by the maximum number of droplets which can simultaneously hit the probe. This hypothesis, which is precautionary, represents the worst condition that can occur in droplets impact.
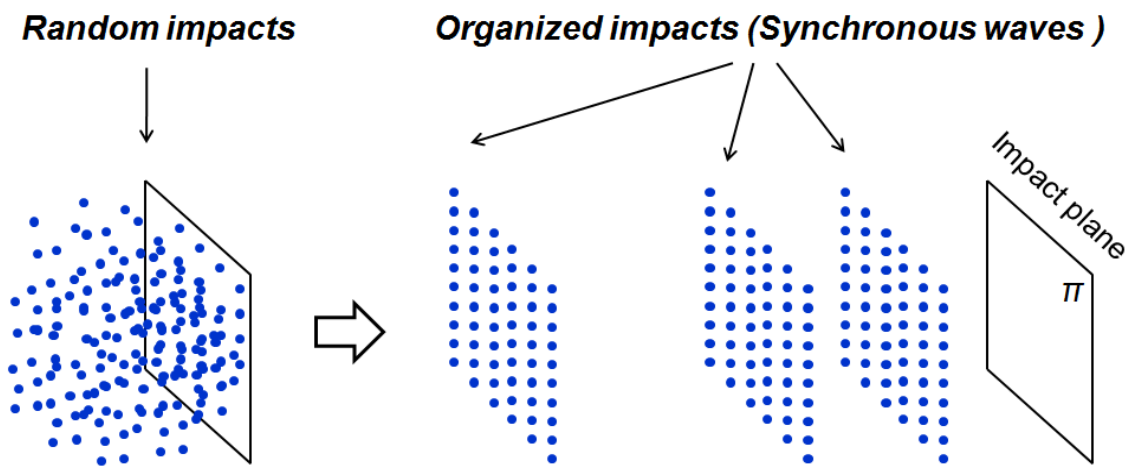
Figure 2.12: Droplets impact schematization.

The maximum droplets number of a singular wave $N_{d,wave}$ and the frequency of droplets impact fr_{di} can be estimated as follows:

$$N_{d,wave} = \frac{A_{f,di}LVF}{A_d} \qquad (2.55)$$

$$fr_{di} = \frac{N_d}{N_{d,wave}} \qquad (2.56)$$

In order to complete the dynamic analysis one must calculate the **natural frequencies of the system** and compare them with those obtained above. The probe can be approximated as a uniform cantilever beam with a mass on its end. The first natural frequency fr_{nat} can be computed as follows [52, 53]:

$$fr_{nat} = \frac{\omega_{nat}}{2\pi} \tag{2.57}$$

$$\omega_{nat} = \frac{k}{M + 0{,}23m} \tag{2.58}$$

In the present application, *m* represents the mass of the stem and *M* is the mass of the shield. The beam *stiffness k* can be calculated as follows:

$$k = \frac{3EI}{L^3} \tag{2.59}$$

The approach used for the calculation of probe first natural frequency is very simple and it gives approximated results. Since the present case is simple, one can easily perform a FEM modal analysis of the system to calculate its modal response. The results of some FEM analyses on a practical case will be discussed in the following chapter.

In the present chapter the most important steps of probe detailed design were discussed. The analytical model performs a complete design and analysis of probe performance, from the fluid dynamics and the structural point of view. The following chapter describes the results of the model for a specific application. The reference test conditions are shown, together with the main results of the model. Probes manufacturing, together with FEM analyses and ping tests results are also discussed.

Chapter 3

Analytical model

The analytical model discussed in the previous chapter was run for a pressurized two phase flow, composed by air and water, with a LVF up to 3%. The operating conditions corresponded to those of a test facility located at SwRI (Southwest Research Institute, Texas), where the probes have been subsequently tested. The present chapter shows the main results of the model, together with those of some FEM static and modal analyses. Probes manufacturing is also discussed, together with the results of some ping tests.

3.1 Analytical model: simulation and results

The analytical model for probes design was run with the operating conditions listed in Table 3.1. These conditions were provided by GE Oil & Gas and correspond to those of a test facility located at Southwest Research Institute (SwRI). They represent the properties of a pressurized wet flow, composed by air and water. Since the values change from test to test, GE selected two operating conditions among those in table 3.1 as reference points for probes design.

Table 3.1: Operating conditions for probe design: SwRI facility

Gas flow	
$P_{0,g}$ [bar]	15-25
$T_{0,g}$ [°C]	25-70
v_g [m/s]	5-30
Droplets	
d_d [μm]	100-400
Mixture	
LVF [%]	0-3

From the table above it emerges that the operating conditions for probes design are not typical of a probes calibration facility in terms of velocity (Ma<0.1). In these conditions, the pressure and temperature kinetic contributions are very low and the results are heavily affected by the sensors uncertainty. This is due to the fact that the SwRI facility was not designed for probes calibration but for wet tests on centrifugal compressors. After probes testing, a post-processing activity was performed and the model was improved. From the results of these tests, new concepts and ideas were also studied in order to optimize and minimize probes. Finally, the lack of suitable facilities for wet probes calibration gave an impulse for the development of a new facility. The dedicated test rig, which is under assembly, will be a useful instrument for the validation of probes and the investigation of new solutions to improve their design. The development of such a facility is not discussed in the present work.

Referring to test conditions (Table 3.1) and to the probes type shown in Fig 1.9, the model was used to design several probes configurations. Each probe was identified with a tag, composed by three letters and one number:

$$L_1 \, L_2 \, L_3 \, N_1$$

Table 3.2 explains the tag symbols:

Table 3.2: Tag symbols legend

ID Symbol	Value	Explanation
L_1	*P*	Total pressure probe
	T	Total temperature probe
L_2	*S*	Compressor suction
	D	Compressor discharge
L_3	*A*	Shield standard shape (Fig. 1.9)
	B	Shield alternative design (Fig. 1.9)
N_1	*1*	Number of purging holes set to 1
	2	Number of purging holes set to 2

Apart from the shield shape (standard shape or alternative design), the most important difference among the above configurations is represented by the size of the purge holes. This is a consequence of the different operating conditions between compressor suction and discharge and by the different amount of liquid that flows into the shield for total pressure and total temperature probes. In the present work, the results of the analytical model for *PSA2* and *TSA2* probes are presented. Table 3.3 is an overview of probe design main results. As emerges from table 3.3, total pressure and total temperature probes are very similar, except for some details in shield design. The total purging hole area $A_{ph,tot}$ is lower for total temperature probes, where the mini shield influences the liquid amount that flows into the shield. The first natural frequency is lower for total temperature probes, even if the difference between the two probes is insignificant. The most important difference relates to the value of the recovery factor, which is lower for total temperature probes. This is a consequence of the vent holes, which induce a gas flow into the shield, in order to ensure a great value of the thermal exchange between the flow and the sensor.

Table 3.3: Probes design: main results

	PSA2	TSA2
Geometry		
Shield (overview)		
$d_{s,i}$ [mm]	6.6	6.6
$d_{s,e}$ [mm]	8.0	8.0
L_s [mm]	16	16
Converging ducts		
$A_{cd,in}/A_{cd,out}$	2.25	2.25
Purge holes		
Z_{ph}	2	2
$A_{ph,tot}$ [mm^2]	5.9	5.1
Vent holes		
Z_{vh}	-	4
d_{vh} [mm]	-	1.8
$A_{vh}/A_{s,i}$	-	0.3
Stem		
$d_{st,e}$ [mm]	6.35	6.35
$d_{st,e}$ [mm]	4.59	4.59
Structural perf.		
SF	0.42	0.42
dis_{max} [mm]	0.11	0.11
$fr_{nat,I}$ [Hz]	449	446
Fluid mechanics perf.		
PC	1	1
r	0.99	0.93

Figs. 3.1 and 3.2 respectively show an overview of probes PSA2 and TSA2 for SwRI tests. In both the cases, the whole stem is represented only in the isometric view.

Isometric view   Front view   Left view

Top view   Section A-A
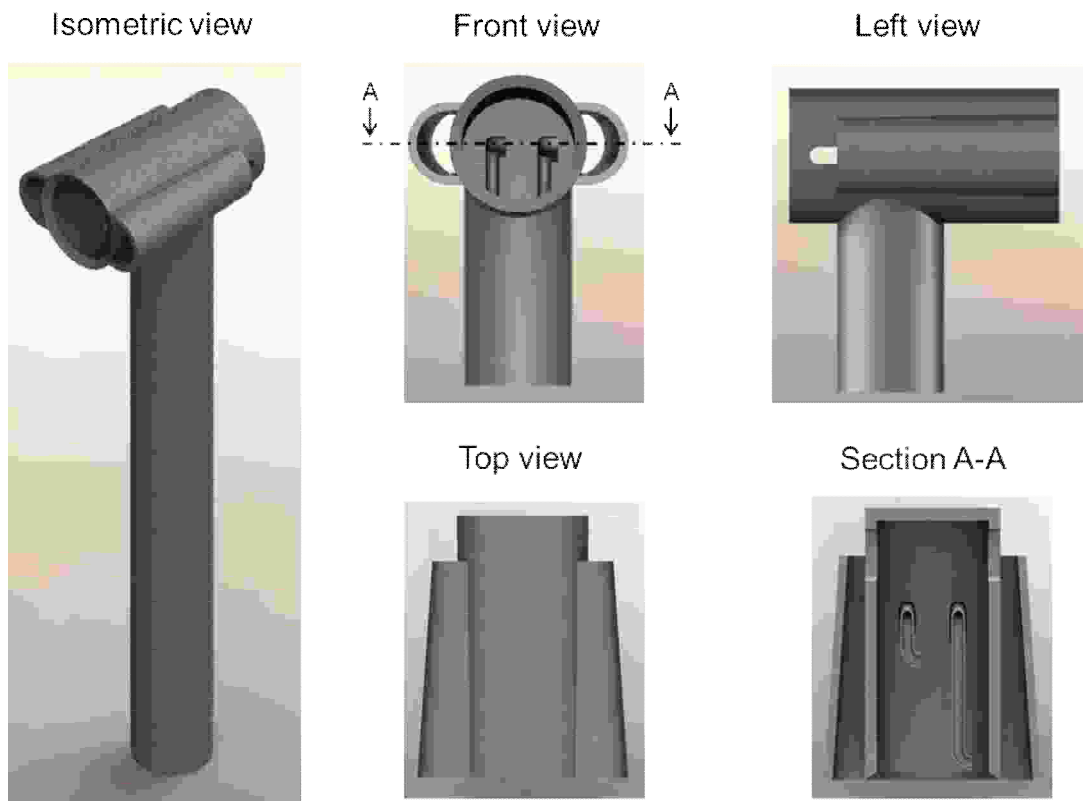
Figure 3.1: Overview of PSA2 probe.

Isometric view   Front view   Left view

Top view   Section A-A
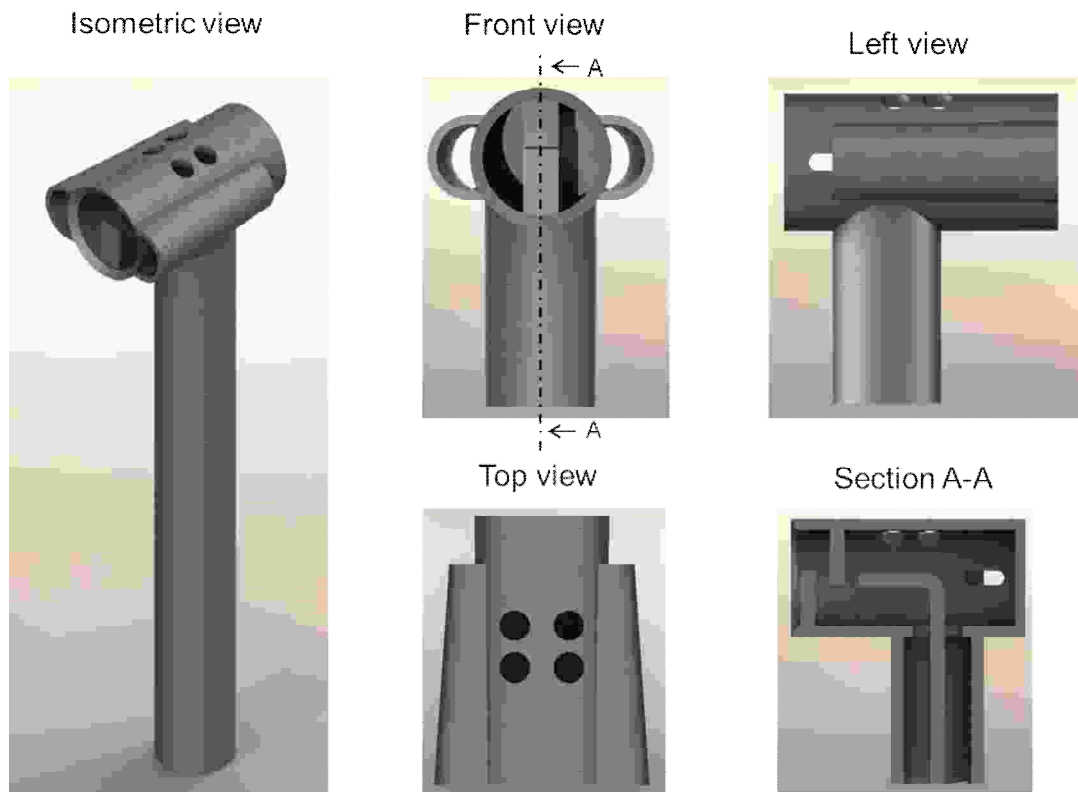
Figure 3.2: Overview of TSA2 probe.

3.2 Analytical model: parametric analysis

In order to assess probes behavior, a parametric analysis was performed as a function of the most important design variables. Each parameter was varied individually. This paragraph presents some significant results of the analysis, from the structural and the fluid mechanics point of view.

3.2.1 Structural analysis

Starting from probes structural behavior, Fig. 3.3 shows the influence of **Liquid Volume Fraction** on Stress factor and maximum displacement. As emerges from Table 3.3, the structural behavior is the same for total pressure and total temperature probes. The following results refer both to probe PSA2 and TSA2.
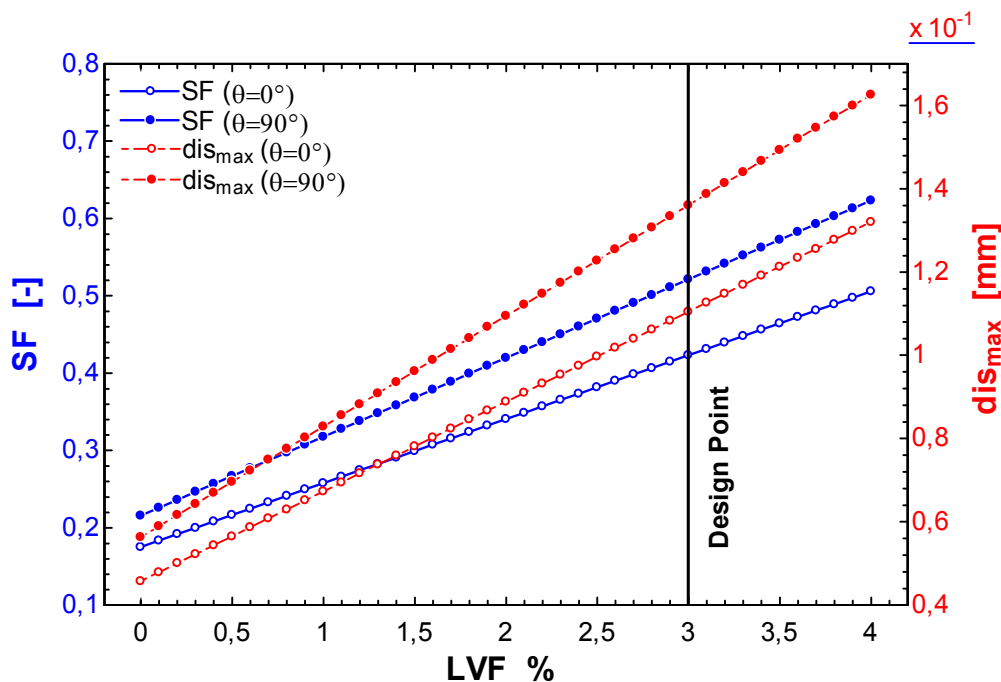
Figure 3.3: SF and dis$_{max}$ as a function of LVF.

As emerges from the figure above, *SF* and *dis$_{max}$* are proportional to *LVF*. In fact, an increase in *LVF* leads to an increase in the mixture density. The probes show a good static behavior in both the cases of θ=0° and θ=90° for all the values of *LVF*.

The influence of **Mach number** and **total pressure of gas phase** on the probe static behavior is shown in Figs. 3.4 and 3.5:
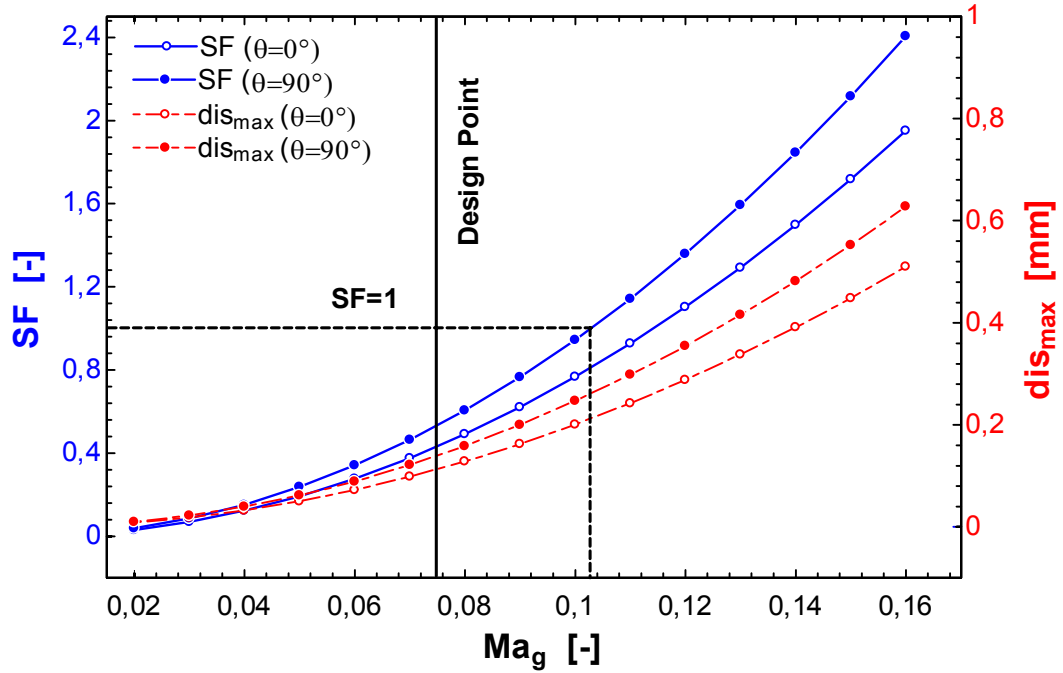
Figure 3.4: SF and dis_max as a function of Ma_g.
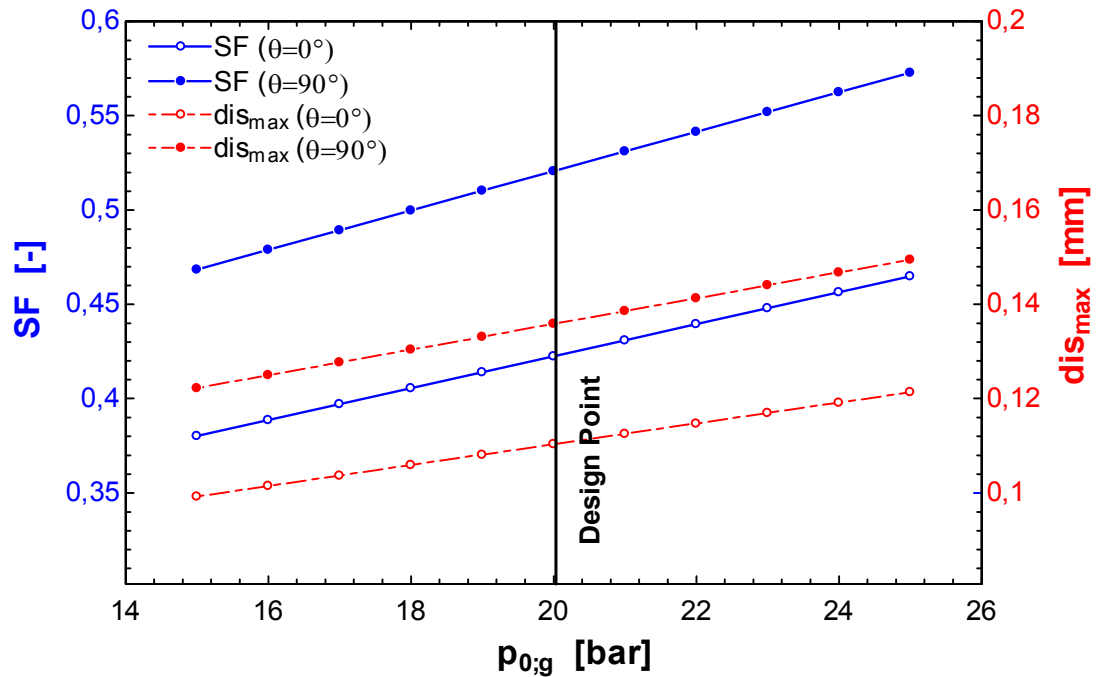
Figure 3.5: SF and dis_max as a function of P_0,g.

Mach number has a great influence on probes structural behavior (Fig. 3.4). Since the drag forces depend on the square of the velocity (eqs. 2.30, 2.31), an increase in Ma_g leads to an increase in *SF* and *dis_max*. The probes show a good structural behavior for all the test

conditions (Ma<0.09). If the Mach number increases (this is not the case of SwRI test rig), the probes present some structural problems. During this research activity there was no test rig available to simultaneously achieve high values of pressure, LVF and Mach number.

The influence of $P_{0,g}$ on *SF* and dis_{max} is lower than those of *LVF* and Ma_g. Since the value of Ma_g is fixed, an increase in $P_{0,g}$ leads to an increase in P_g and ρ_g. The value of ρ_h increases too, leading to higher values of *SF* and dis_{max}. As emerges from Fig. 3.5, probes structural behavior is satisfied for all the test conditions.

Since the influence of $T_{0,g}$ on probes structural behavior is very weak, it is not represented in the present work.

After analyzing probes structural behavior from the static point of view, it's important to discuss their dynamic behavior. The frequency of vortices generated by the shield and the stem and that of droplets impact depends mostly on Mach number and temperature, which influence velocity, density and viscosity of the gas phase. The most important effects of vortices are related to probe stem. Figs 3.6 and 3.7 represent the influence of **Mach number** and **total temperature** on the frequency of stem vortices, comparing it with the first natural frequency of the probe, which is the most critical from the structural point of view. The value of $fr_{vs,st}$ has a great dependence on Ma_g (Fig. 3.6). If Ma_g increases, $fr_{vs,st}$ increases too, until Ma_g becomes 0.12. If $Ma_g>0.12$, Re_s becomes higher than 300000, corresponding to the region where the Karman vortex street is not regular [44]. The probe has a good dynamic behavior at the design point and for most Ma_g values. However, some problems may occur for Ma_g around 0.04, where $fr_{vs,st}$ matches the first natural frequency of the probe. Since the exiting forces related to vortices are very low in this case, they won't lead to a structural damage even if a resonance occurs. However, if some tests at these conditions are required, a possible solution consists in changing the stem height, which has a great influence on probe dynamic response.
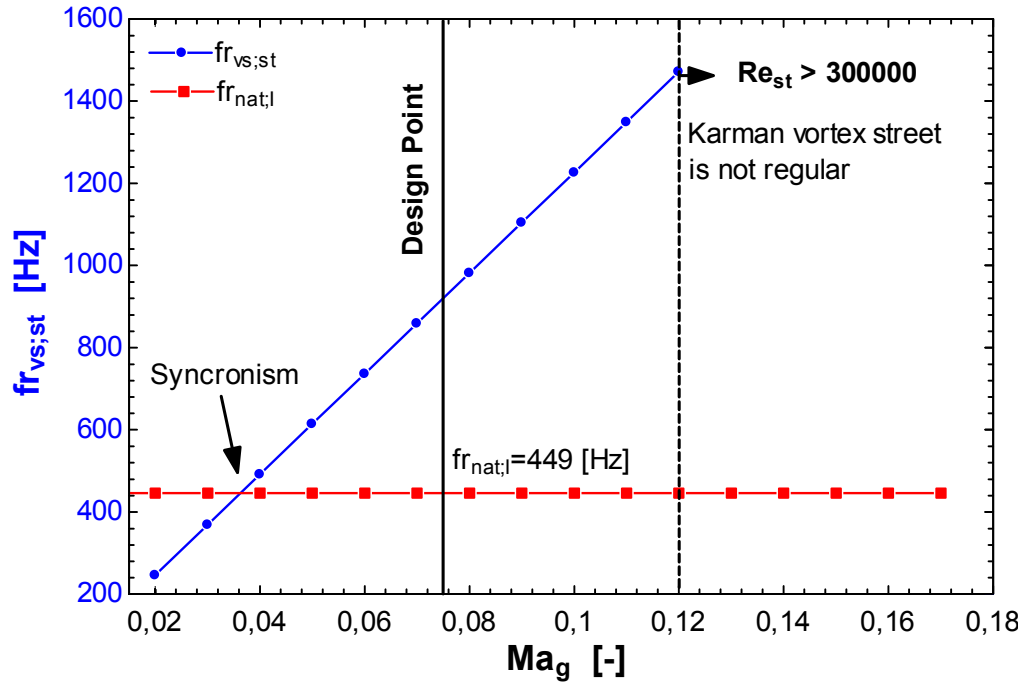
Figure 3.6: $fr_{vs,st}$ as a function of Ma_g.
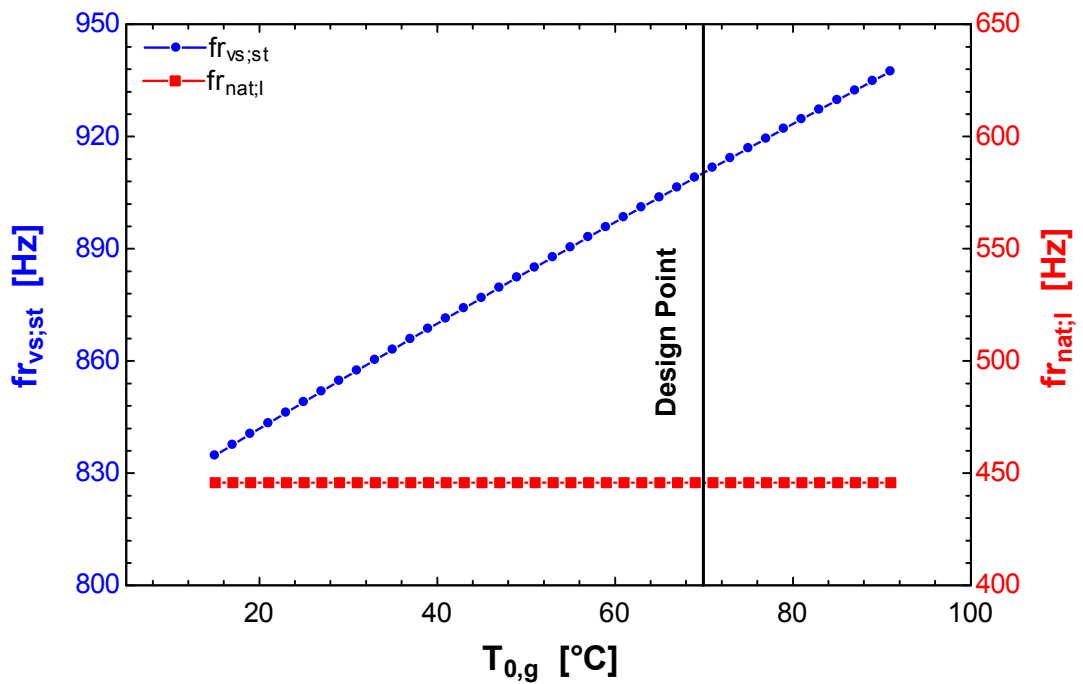
Figure 3.7: $fr_{vs,st}$ as a function of $T_{0,g}$.

$T_{0,g}$ has a weak influence on $fr_{vs,st}$ (fig. 3.7). From the figure above emerges that the probe has a good dynamic behavior for all the temperature conditions.

The influence of **Mach number** and **total temperature** on droplets impact frequency is represented in Figs 3.8 and 3.9:
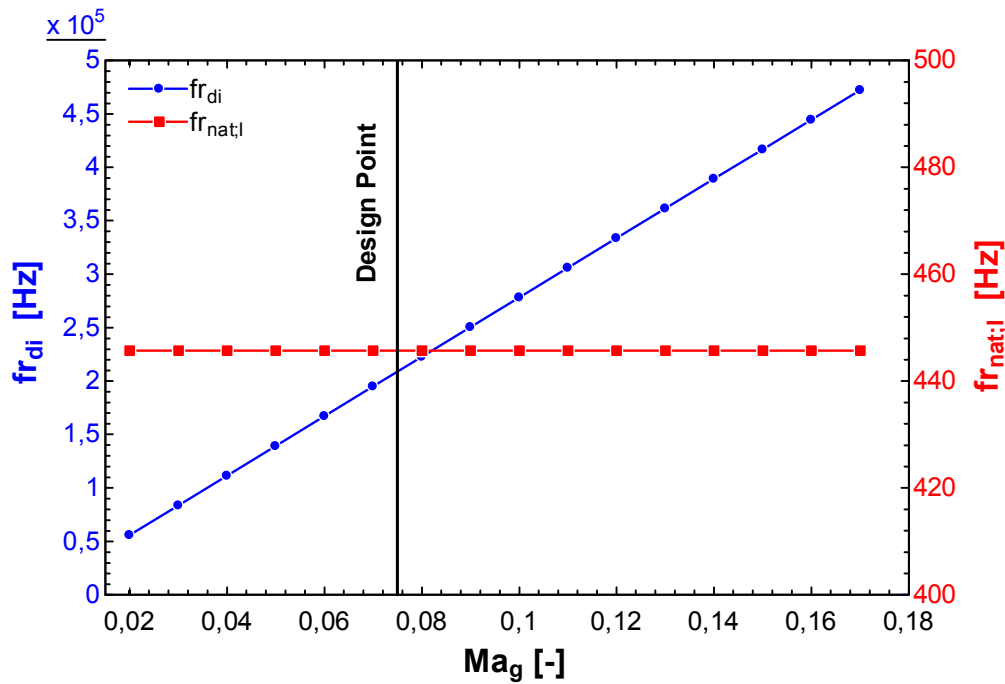
Figure 3.8: fr_{di} as a function of Ma_g.
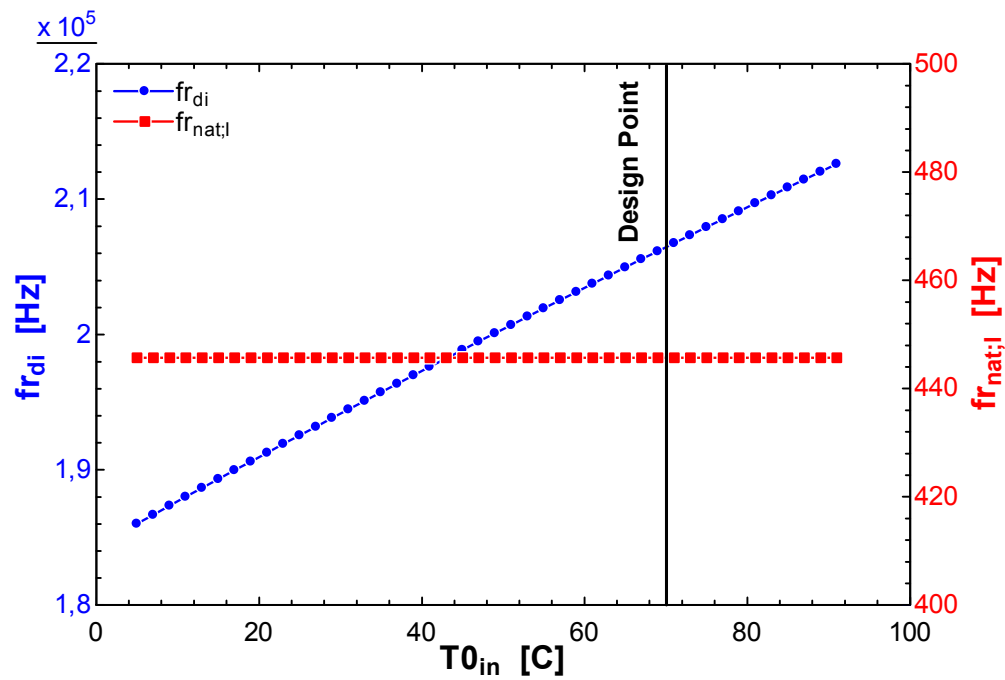
Figure 3.9: fr_{di} as a function of $T_{0,g}$.

As for the frequency of the vortices, Ma_g has a great influence on fr_{di}, while the influence of $T_{0,g}$ is weak. From Figs. 3.8 and 3.9 emerges that droplet impact doesn't lead to any risks for probes structural behavior. Droplets impact frequency is at least 2 order of magnitude higher than the probes first natural frequency.

After discussing the probe static and dynamic behavior it is important to present also the results of the fatigue analysis. The most interesting results relate to the case of probe oriented with a yaw angle. The parametric analysis can be performed as a function of the yaw angle. The first step is the drag forces and moments calculation as a function of this parameter. Then, the associated stress can be calculated. Finally, one must verify probe resistance under fatigue loads using the Goodman-Smith and Haigh's diagrams.

Figs 3.10 and 3.11 show the drag forces and the moments as a function of the **yaw angle**.
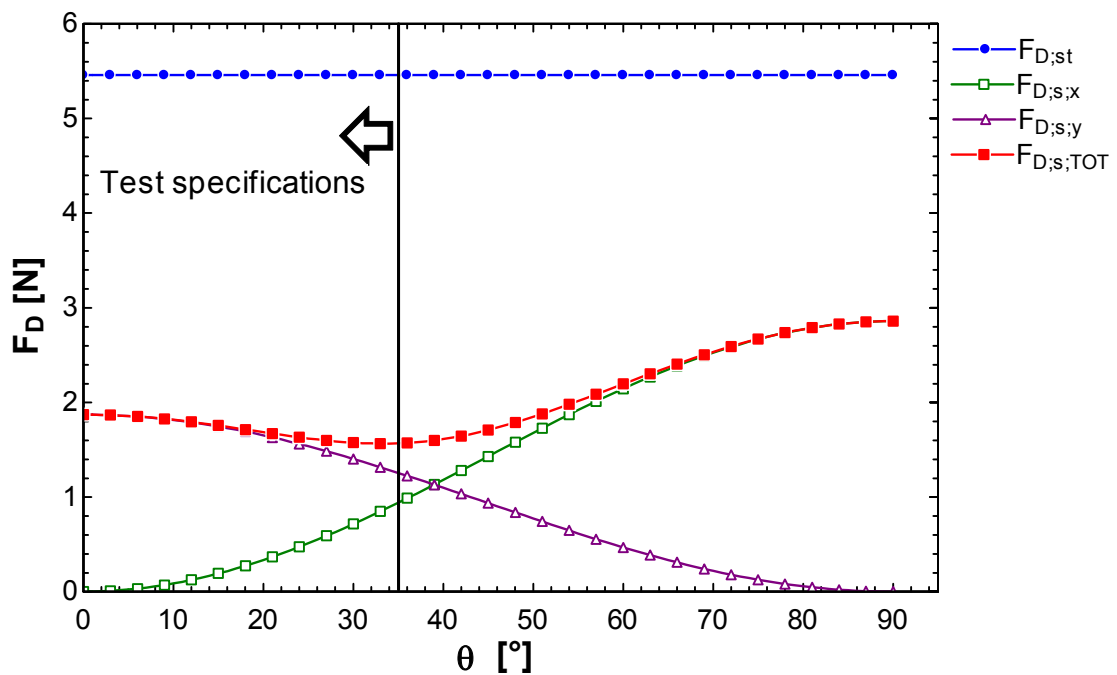
Figure 3.10: F_D as a function of θ.
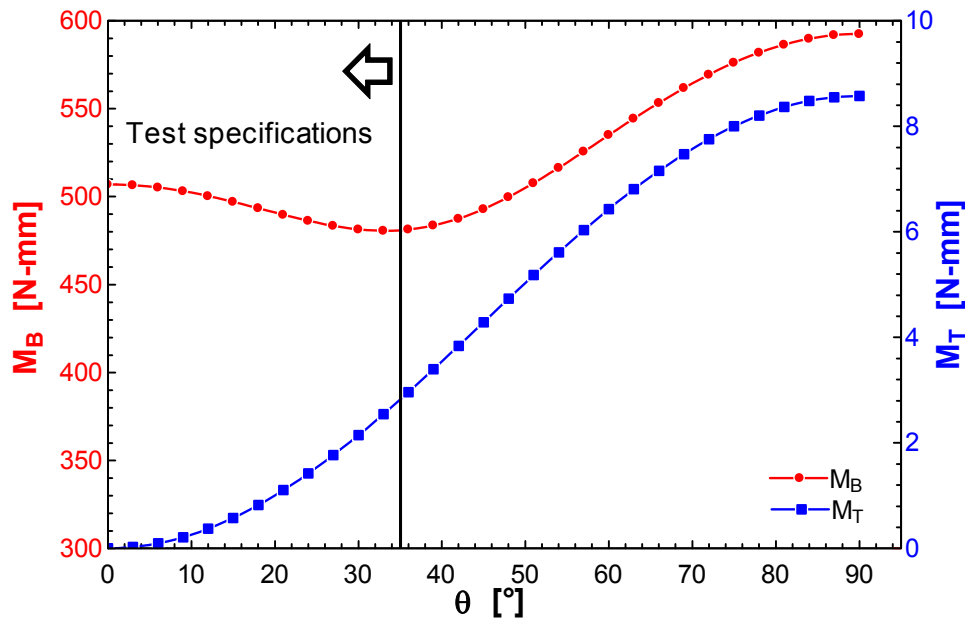
Figure 3.11: M_B and M_T as a function of θ.

Since the stem is an annulus cylinder, $F_{D,st}$ doesn't depend on θ (Fig 3.10). As expected from the previous chapter, $F_{D,s,TOT}$, which is the resultant between $F_{D,s,x}$ and $F_{D,s,y}$, depends on θ. The drag forces trend influences the moments one (Fig. 3.11).

From drag forces and moments value, the corresponding values of structural stress can be calculated. Fig. 3.12 represents σ_{VM}, τ_{sh} and τ_T as a function of θ. σ_{VM} is obtained from σ_B, τ_{sh} and τ_T. From the values of stress obtained and represented, one must select the worst load cases in order to analyze the probe structural resistance under fatigue loads. The worst load conditions are associated with high values of θ (θ>80°). However, test specifications impose values of θ between -35° and 35°. For such values the worst conditions occur when θ tends to lower values (Fig 3.12, red ellipse). A value of θ=5% was selected for the fatigue verification.
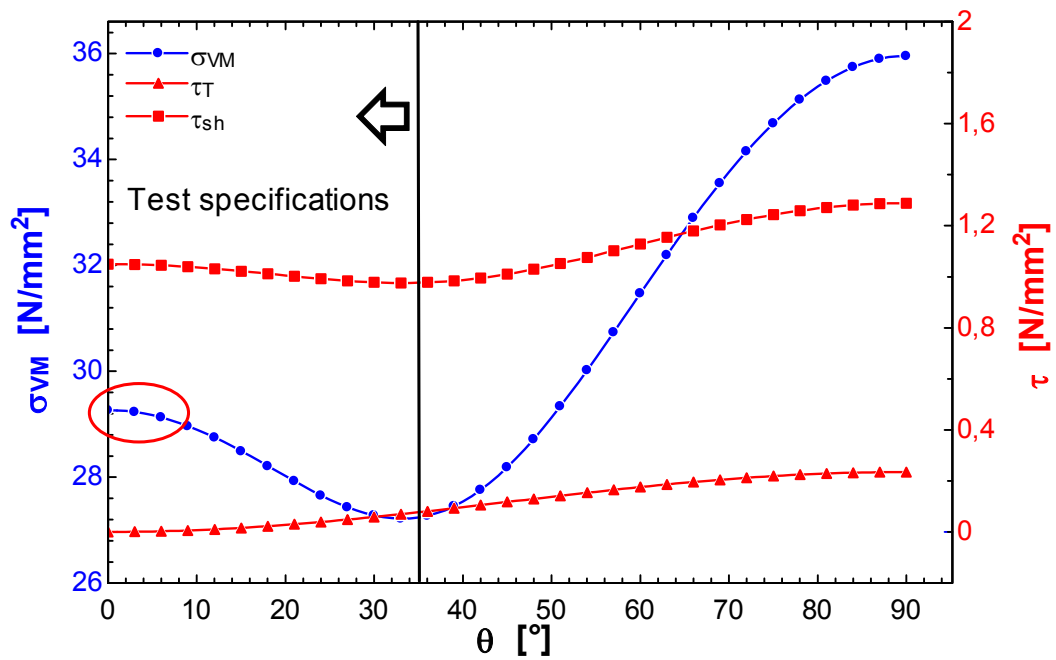
Figure 3.12: Stress as a function of θ.

Figs 3.13 and 3.14 respectively show the Goodman-Smith and the Haigh's diagram for the load case corresponding to θ=5°
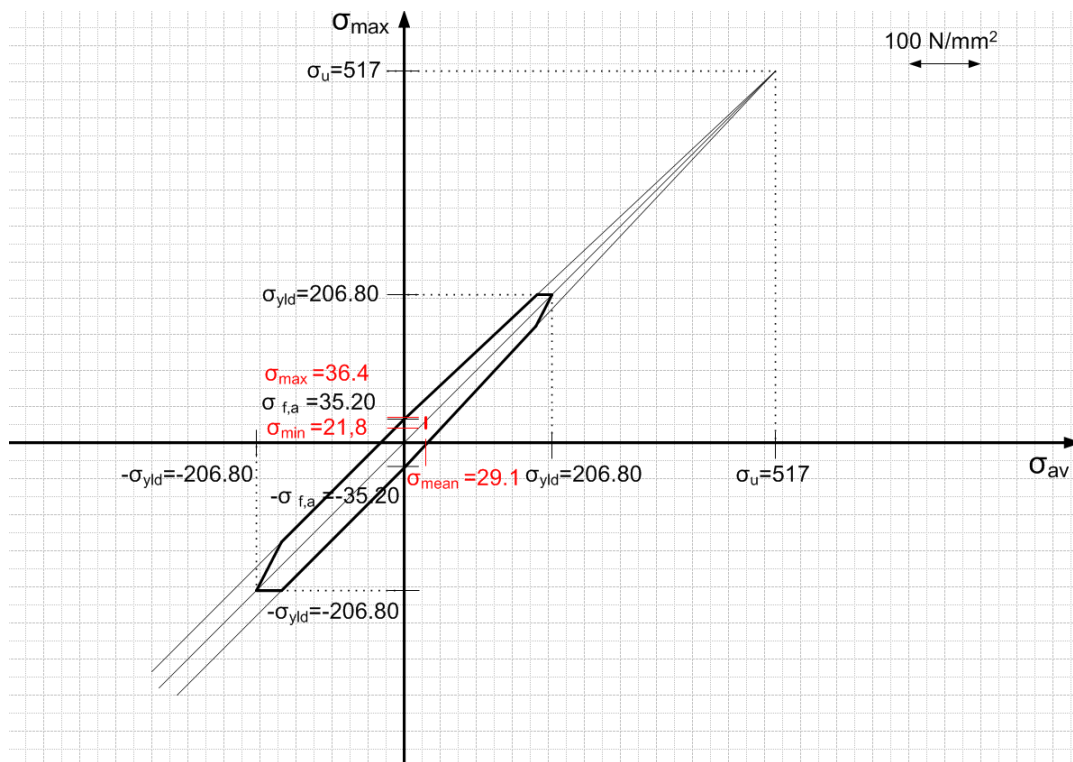
Figure 3.13: Goodman-Smith diagram, θ=5°.
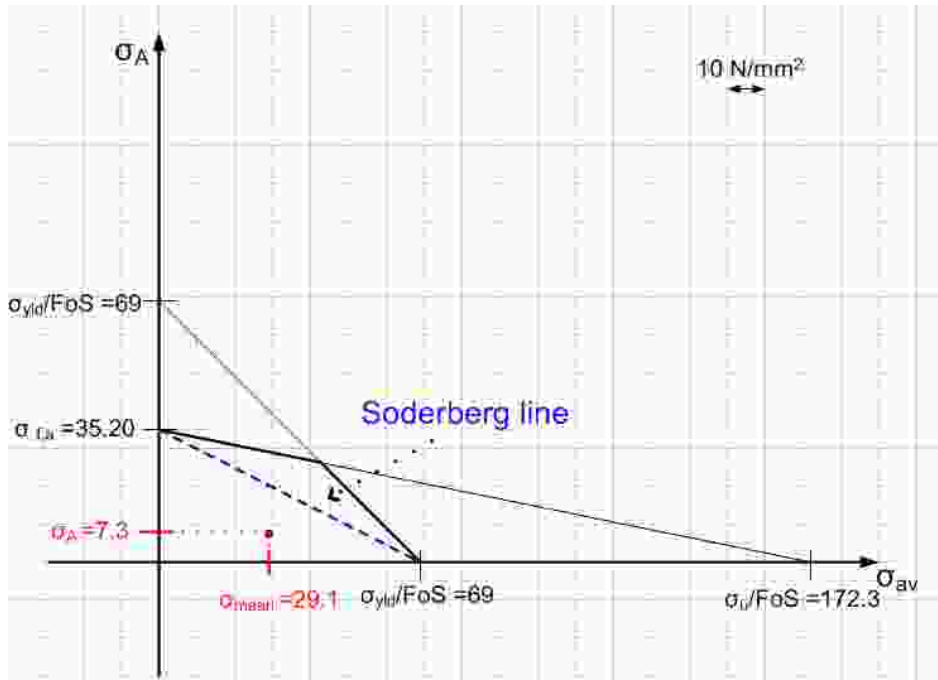
Figure 3.14: Haigh diagram, θ=5°.

Both the diagrams show that the probes ensure a good structural resistance under fatigue loads. In order to verify probes structural resistance in a simple and fast way, the model uses the following equation, related to the Soderberg's line (Fig. 3.14):

$$\frac{\sigma_A}{\sigma_{f,a}} + \frac{\sigma_{mean}}{\sigma_{yld}/FoS} \tag{3.1}$$

If the result of the equation is lower than 1, the probe structural resistance is ensured. A value of 0.24 was obtained for the present case.

The results discussed above confirm that the model is physically sound from the static, the dynamic and the fatigue point of views.

3.2.2 Fluid mechanics analysis

After discussing the results of the parametric analysis from the structural point of view, it's important to present the results of the fluid mechanics analysis. The present section shows the influence of the operating conditions on probes performance, from the fluid mechanics point of view. The following figures and the associated discussions let one to understand probes physical behavior, which is a fundamental issue to optimize their

design. Referring to the following figures, the actual value of each parameter was divided by the corresponding for the design conditions. The subscript "R" stands for "ratio".

Fig. 3.15 represents the **LVF** influence on the purge coefficient and the recovery factor.
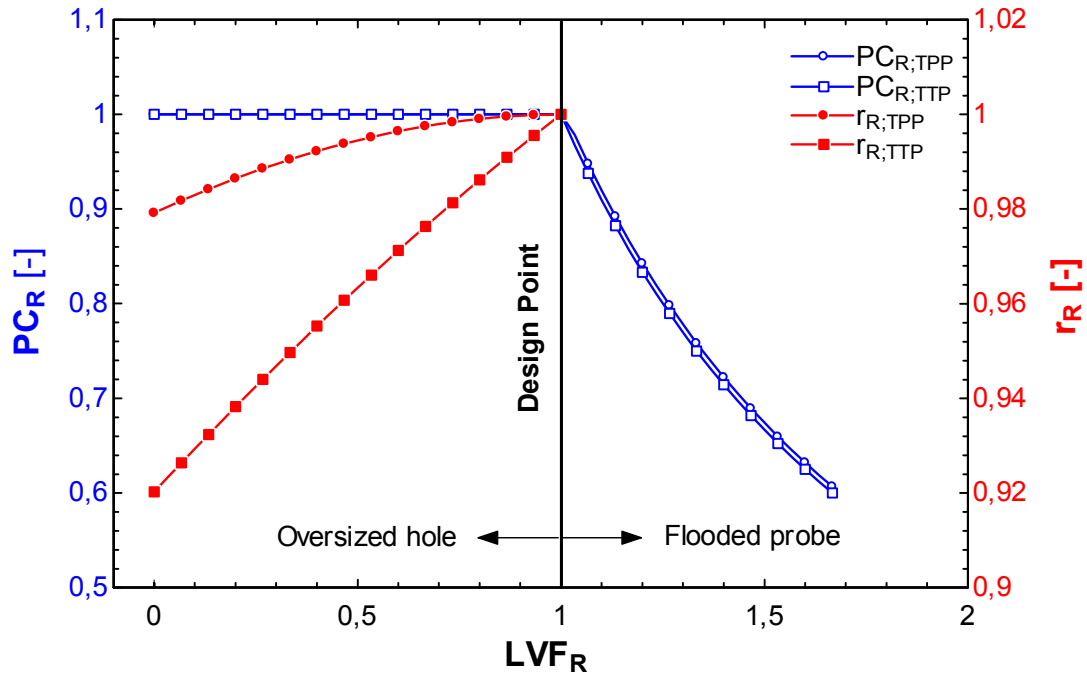
Figure 3.15: *PC_R and r_R as a function of LVF$_R$.*

LVF has a notable influence on the probe performance. If its value increases, the amount of liquid mass flow rate entering the shield increases too, leading to a progressive probe flooding. Starting from low values of *LVF*, the purge system is oversized, and a certain amount of gas flows inside the shield. Under these conditions *r* is lower than the design value ($r_R < 1$). If *LVF$_R$* increases, the recovery factor increases too, until the design point is approached. If *LVF$_R$* continues to increase, the probes become flooded. In this area, the recovery factor cannot be defined. The trend is the same for total pressure and total temperature probes. However, due to the presence of vent holes, total temperature probes show lower values of r_R.

P$_{0g}$ has a certain influence on probes performance (Fig. 3.16):
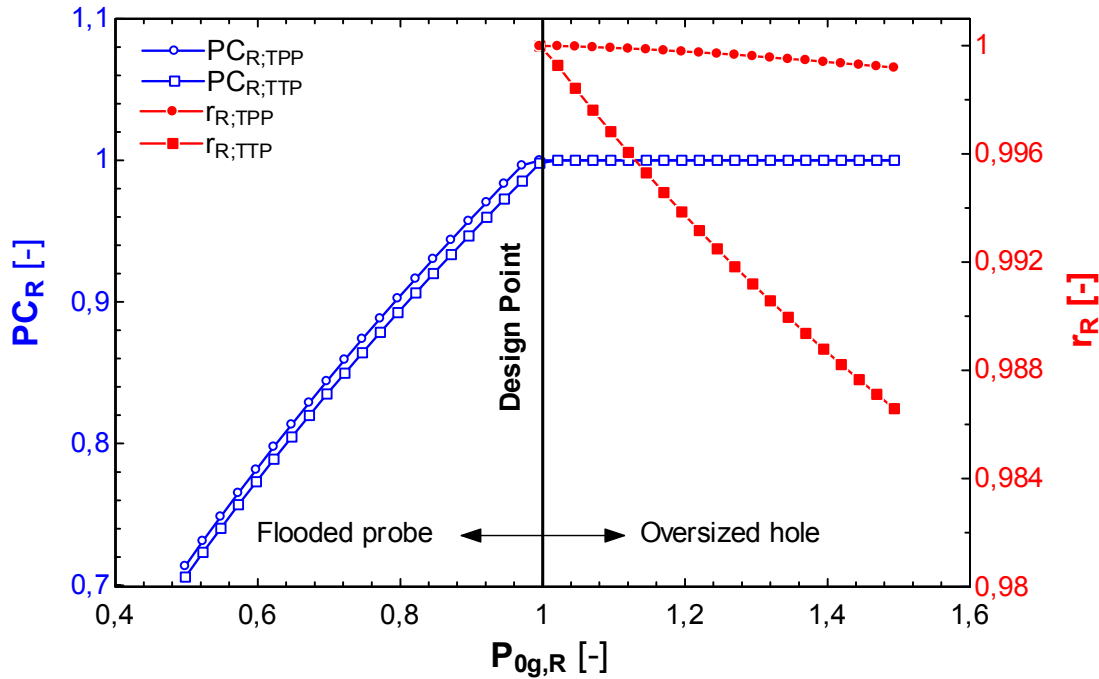
Fig. 3.16: ***PC*$_R$** **and *r*$_R$** **as a function of P$_{0g;R}$.**

An increase in P_{0g} leads to an increase in the pressure drop between probe internal region and converging ducts outlet. A greater amount of water flows through purging holes. If P_{0g} is lower than the design value ($P_{0g,R} < 1$), the probe is flooded and r can't be defined. Once PC assumes a unit value ($P_{0g,R} = 1$), if P_{0g} increases ($P_{0g,R} > 1$) the purging system becomes oversized and a certain amount of gas flows inside the shield ($r_R < 1$). As in the previous case, the trend is the same for the two kinds of probe, even if total temperature probes show lower values of recovery factor on account of the presence of water.

The influence of **Mach number** on probe performance is important, even if it can't be completely observed in the present application case, where it assumes very low values (Ma<0.075). Fig. 3.17 shows the influence of Mach number on purge coefficient and recovery factor. If *Ma* increases, the static pressure and density of gas phase decrease, while its velocity increases. Since a homogeneous flow model is used, the velocity of the liquid phase increases too. This condition leads to a greater mass flow rate of water inside the shield. However, if *Ma* is higher than the design value ($Ma_R > 1$), the recovery factor decreases. In fact, for SwRI tests, the nozzle operates in unchoked conditions. In this area, if the Mach number increases, the pressure drop between the internal region of the probe and the local external area increases, leading to an enhanced purging effect. For this reason, the recovery factor decreases. Once the nozzle is chocked, which is not the case of

SwRI tests, the pressure drop and the purge effects remain constant. In this area, higher values of *Ma* lead to an increase in the value of *r*.
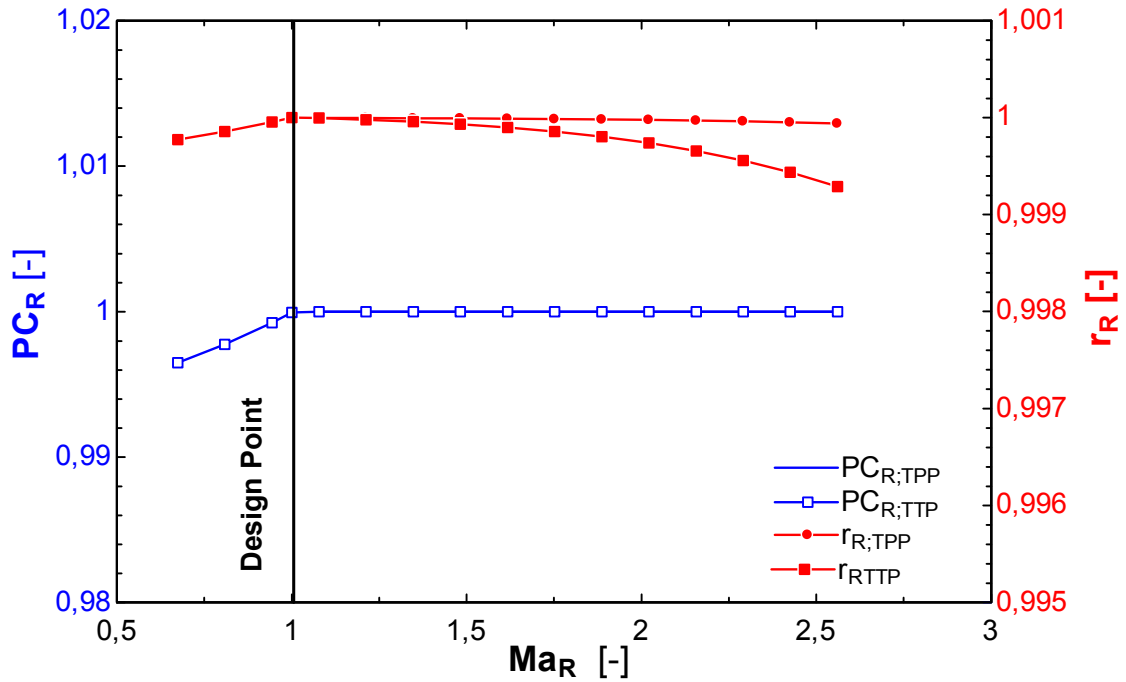
Figure 3.17: *PC_R* and *r_R* as a function of Ma_R.

The **size of the purge holes** has a strong influence on probe performance. During the design phase, several simulations were performed in order to select the best value for purge holes length and radius. Fig. 3.18 shows the influence of purge holes area on PC_R and r_R. If A_{ph} is lower than the design value ($A_{ph,R} < 1$), the probe is flooded. In these conditions, PC is lower than 1 and the recovery factor can't be defined. At the design point, PC assumes a unit value and *r* reaches its maximum value. Finally, if the purge holes cross section is larger than the design value ($A_{ph,R} > 1$), the purge is still complete, but a certain amount of gas flows into the shield ($r_r < 1$). In these conditions, the purge system is oversized and the pressure and temperature tend to the static value.
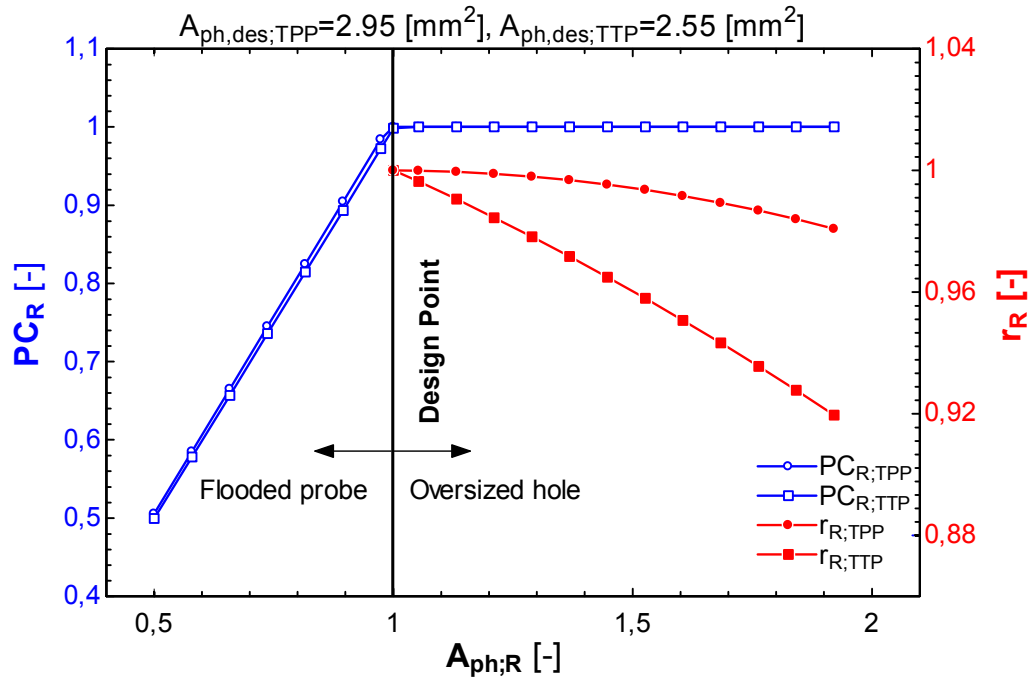
Figure 3.18: *PC_R* **and** *r_R* **as a function of $A_{ph,R}$.**

The results presented in this section show that the model is physically sound also from the fluid mechanics point of view.

3.3 FEM analysis

After probes design with the analytical model, a Finite Element Analysis (FEA) was performed to preliminary validate it from a structural point of view. The Solidworks Simulation tool [54] was used for this purpose. First, some static analyses were performed on the whole probe and its components (mini-shield, sensors). The results were compared with those of the analytical model. Then, the probe natural frequencies and modal shapes were computed with a modal analysis. The analytical model results were very close to those obtained with the numerical analysis.

The present section shows the most important steps and results of the numerical analysis.

Generally, a FEM analysis involves the following steps [55]:

- Geometry drawing and setting up

- Mesh building

- Material assignment

- Boundary conditions

- Analysis

- Post-processing

In the present case the geometry is very simple and there is no need to process it for the FEM analysis. The only modification was performed on the shield internal bevel, which has no meaning from the structural point of view. For this reason, it was removed and replaced with a flat surface (Fig. 3.19).
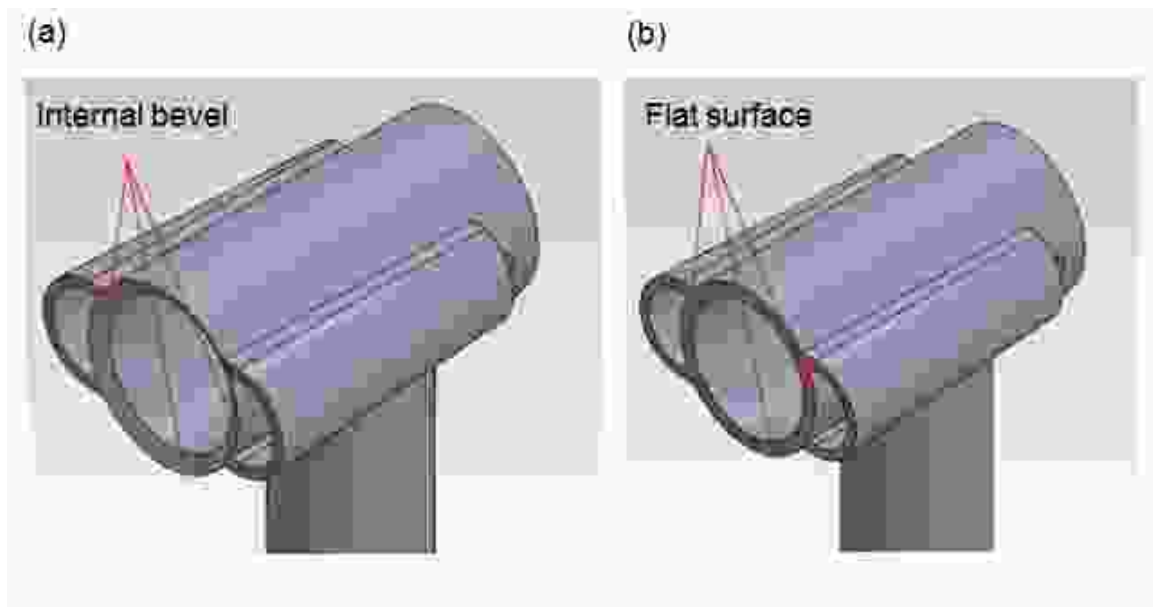
Figure 3.19: Geometry processing for FEM analysis. (a) Original geometry; (b) Modified geometry.

After processing the geometry, one can generate the mesh. Since the present case is very simple, a standard 3D fine mesh, with tetrahedral elements, was created (Fig. 3.20):
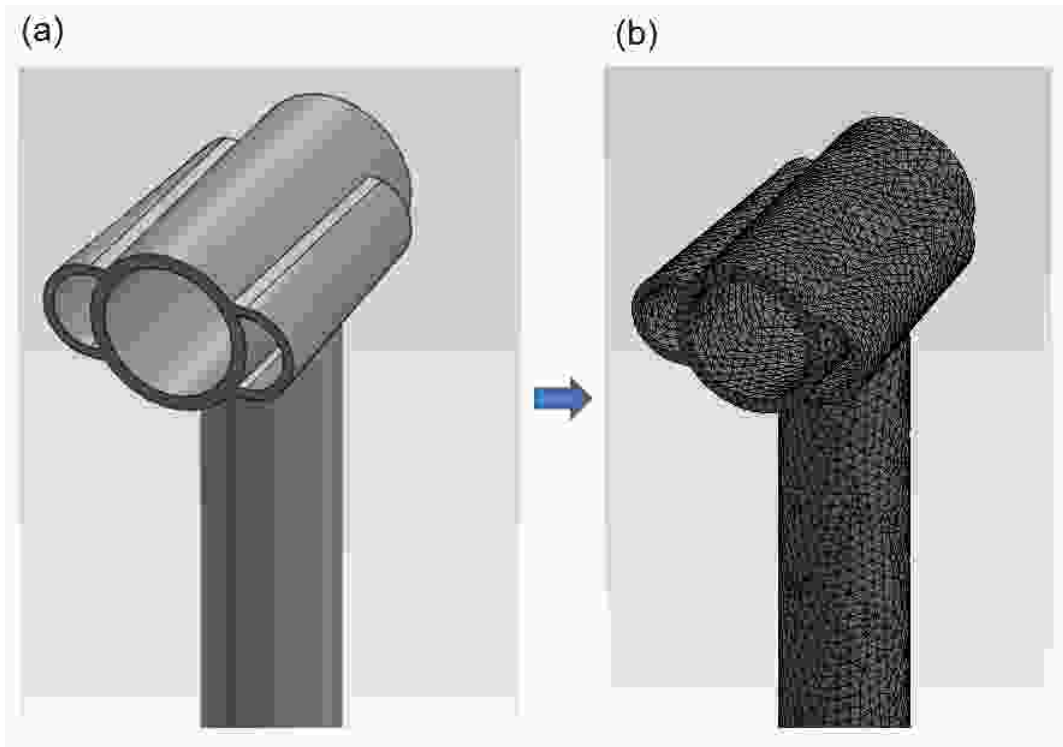
Figure 3.20: Fem analysis model. (a) Geometry; (b) Mesh.

The main mesh features are listed in table 3.4:

Table 3.4: Mesh report (main features)

Mesh Report	
Number of elements	65434
Max aspect ratio	7.94
Elements with AR < 3	99.5%
Elements with AR <10	100%
Failed elements (Jacobian)	0%

After creating the mesh, one must select the material. The stainless steel AISI 304 was used for this case. The material properties, which refer to Solidworks Simulation database, are listed in Table 3.5:

Table 3.5: FEM analysis: material properties.

Material properties	
Material	AISI 304
Young modulus [N/mm^2]	190000
Poisson ratio [-]	0.29
Density [Kg/m^3]	8000
Yield tensile strength [N/mm^2]	517
Ultimate tensile strength [N/mm^2]	208.8

Before running the simulation, one must also set up the boundary conditions, which are different between the static and the modal analysis.

Starting from the static analysis, the load condition is very simple. The loads induced by drag forces and calculated with the analytical model were applied on probe head and probe stem, as uniformly distributed loads (Fig. 3.21a). From the constraints point of view, the probe was modeled as a cantilevered beam (Fig. 3.21b).
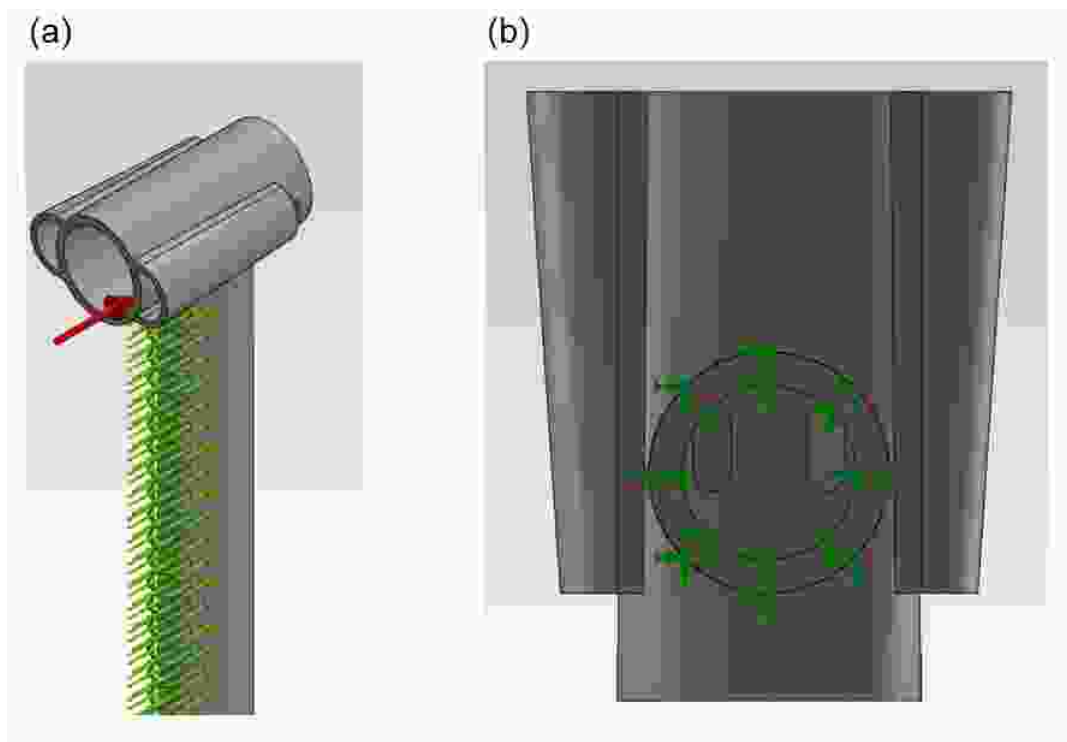
Figure 3.21: FEM static analysis: boundary conditions. (a) Loads; (b) Constraints.

Table 3.6 and Fig. 3.22 represent the results of the static analysis, for the case of probe parallel to flow.

Table 3.6: Static analysis: main results.

STATIC ANALYSIS		
	Analytical model	**Fem analysis**
$F_{D,s}$ [N]	1.87	1.87
$F_{D,st}$ [N]	5.45	5.45
$\sigma_{VM,max}$ [N/mm^2]	**29.30**	**30.20**
dis_{max} [mm]	**0.13**	**0.11**
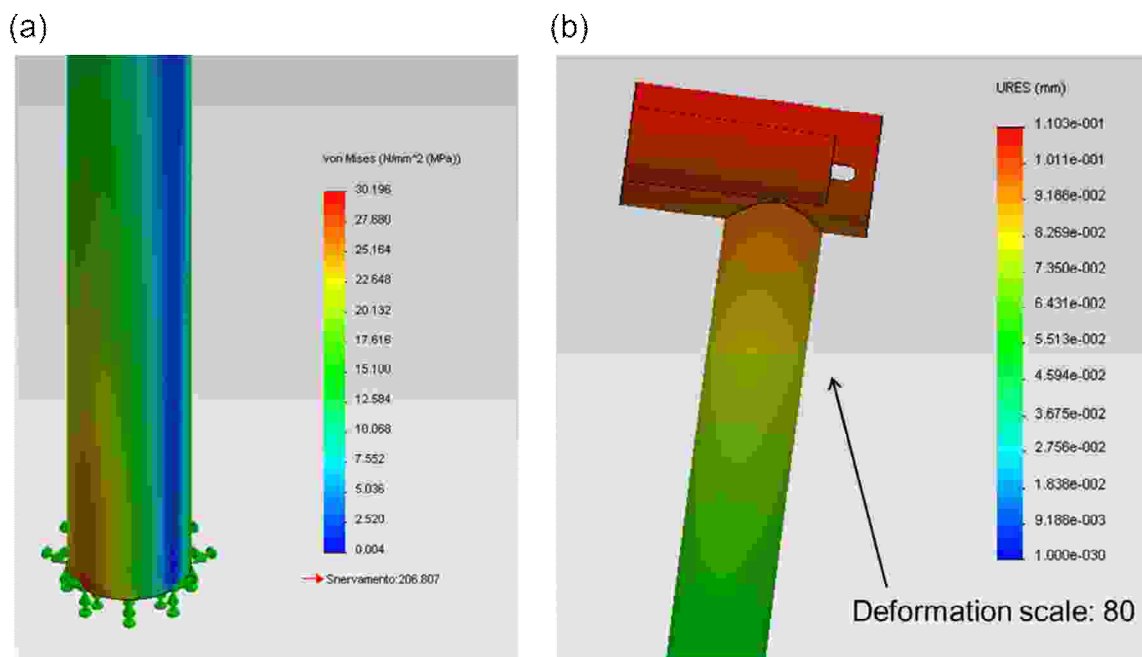
Figure 3.22: Static analysis main results. (a) Von Mises stress, stem basis; (b) Displacement, probe shield and stem terminal section.

As emerges from Table 3.6 and Fig. 3.22, the results obtained with the numerical and the analytical model are very similar, in terms of stress and displacement. The most stressed area, as expected, is located at stem basis. The maximum displacement occurs at probe shield. The results of the numerical analysis confirm that the analytical model gives reliable results in terms of static analysis.

The model developed for the static analysis can be used also for the modal analysis; however, no loads are required. The modal analysis determines the natural modes shape

and frequency, which must be compared with the frequencies obtained with the analytical model. The values of the first natural frequencies of the probe are listed in table 3.7:

Table 3.7: Modal analysis: main results

MODAL ANALYSIS			
	Fem analysis	**Analytical model**	**Mode shape**
$fr_{nat,I}$ [Hz]	426.5	449	Flexural
$fr_{nat,I*}$ [Hz]	426.8	-	Flexural
$fr_{nat,II}$ [Hz]	2851.3	-	Flexural
$fr_{nat,II*}$ [Hz]	2856.2	-	Flexural
$fr_{nat,III}$ [Hz]	4170.6	-	Torsional

Fig. 3.23 shows the first five modal shapes:
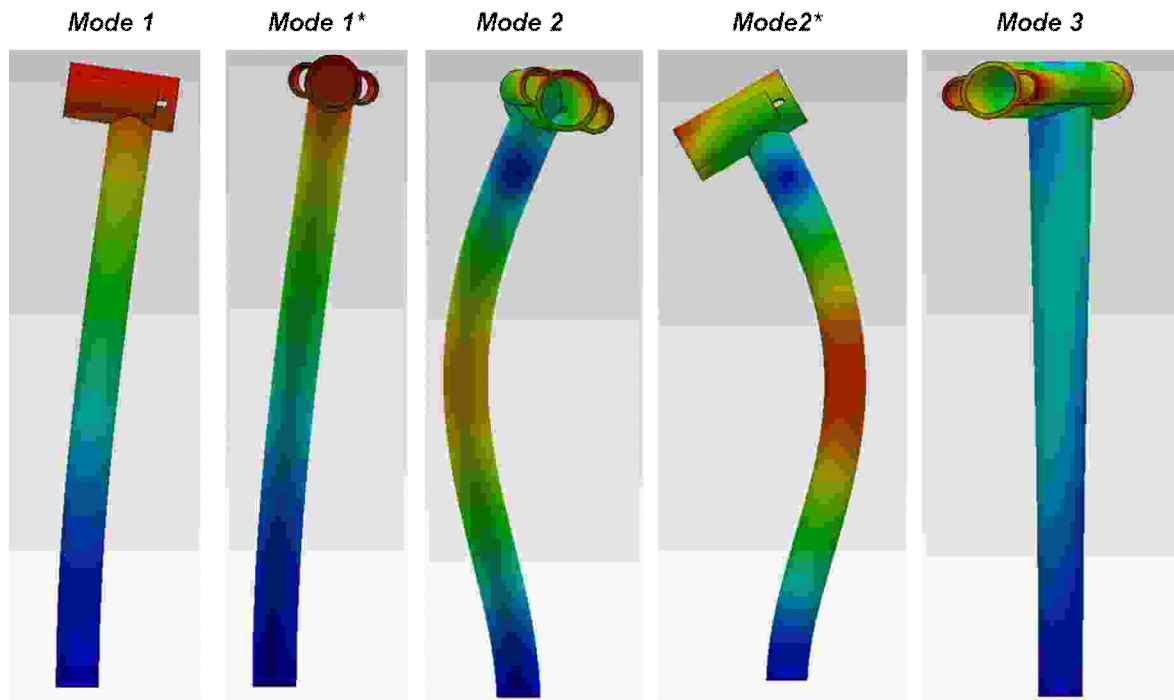
Figure 3.23: Modal analysis: modes shape.

From table 3.7 and Fig. 3.23, it emerges that the first and the second mode have a flexural shape, while the third is a torsional mode. The 1st and the 2nd mode have two values of the natural frequency. This is a consequence of the system symmetry. The most dangerous mode is the first, which should be near the frequency of vortices behind the stem (Figs 3.6-3.9). The value of the 1st natural frequency obtained with the FEM analysis is close to that

obtained with the analytical model, confirming that the model is a reliable instrument for probe design, from the structural point of view.

Chapter 4

Probes manufacturing

4.1 Probes manufacturing

In order to become a reliable instrument for probes design, the analytical model needs to be validated. Starting from the results of the model, some prototypes were manufactured with a Direct Metal Laser Sintering (DMLS) technique [56]. Three prototypes were manufactured for each probe configuration. After its manufacturing, each prototype was processed; the most important geometrical parameters were measured and reported in a comparative table. The best prototype for each configuration was then selected for the test campaign. As previously pointed, probes configuration PSA2 and TSA2 were selected and tested, from a structural and a fluid mechanics point of view. The structural tests consisted in some ping tests, which estimated the first natural frequency of the probes. After this step, the probes were tested in dry conditions in the aerodynamic facility of GE Oil & Gas (Florence). Finally, some preliminary tests in wet conditions were performed in the facility located at SwRI. The present section discusses probes manufacturing and their structural test. The following chapter presents the fluid mechanics tests, both in dry and wet conditions.

From the manufacturing point of view the probe is composed by a shield and a stem. The stem, which is an annular cylinder, was manufactured with a standard machining process. The shield, which is a not a standard component, was manufactured with a DMLS technique [56]. DMLS is an additive manufacturing technology which can quickly

manufacture high quality metal parts, ensuring high resolution and excellent mechanical properties. With a focused laser beam, the DMLS technology melts metal powder locally to fuse it into solid parts. The materials available for such process include Inconel, cobalt chrome, aluminum, titanium, etc. In the present case an alloy of chrome, cobalt and molybdenum was used for shields manufacturing.

The manufacturing process required a geometry modification of total temperature probes. As pointed by the manufacturing company, the mini shield could not be realized as it was because it collapsed during its sintering. In order to avoid this problem they proposed to support it. The conceptual design of such a solution is represented in Fig. 4.1a. Figs 4.1b-d represent the modified geometry of total temperature probes:
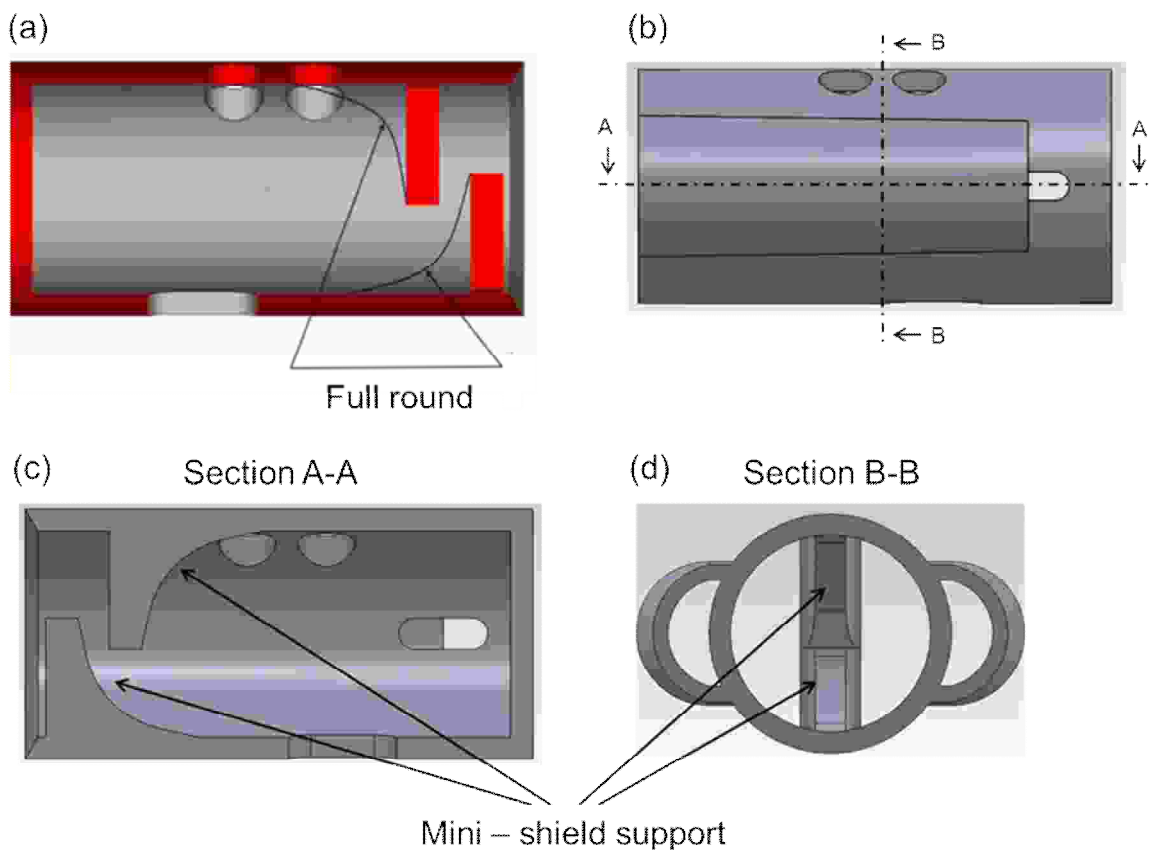
Figure 4.1: Total temperature probe: geometry modifications for shield manufacturing. (a) Conceptual design; (b-d) modified geometry.

After geometry modifications, the probes were manufactured. The following figures represent some prototypes of the manufactured probes.

Fig. 4.2 shows the shield of PSB2 and TSB2 probes:
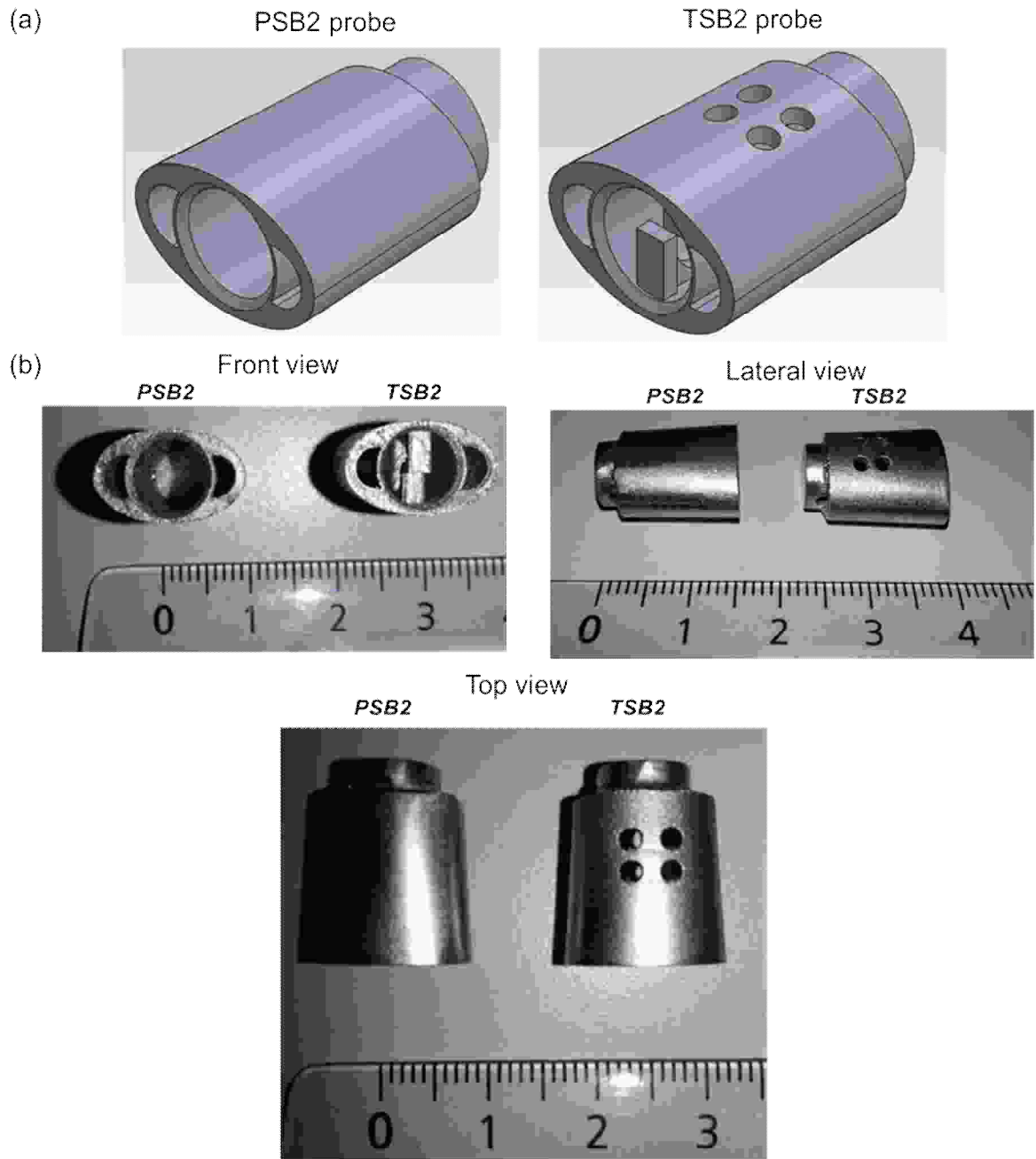
Figure 4.2: PSB2 and TSB2 probes. (a) CAD models; (b) manufactured prototypes.

Fig. 4.3 shows the manufactured prototypes PSA2 and TSB2. These configurations were selected for wet tests at SwRI. The following figure includes the whole probes, including sensing elements.
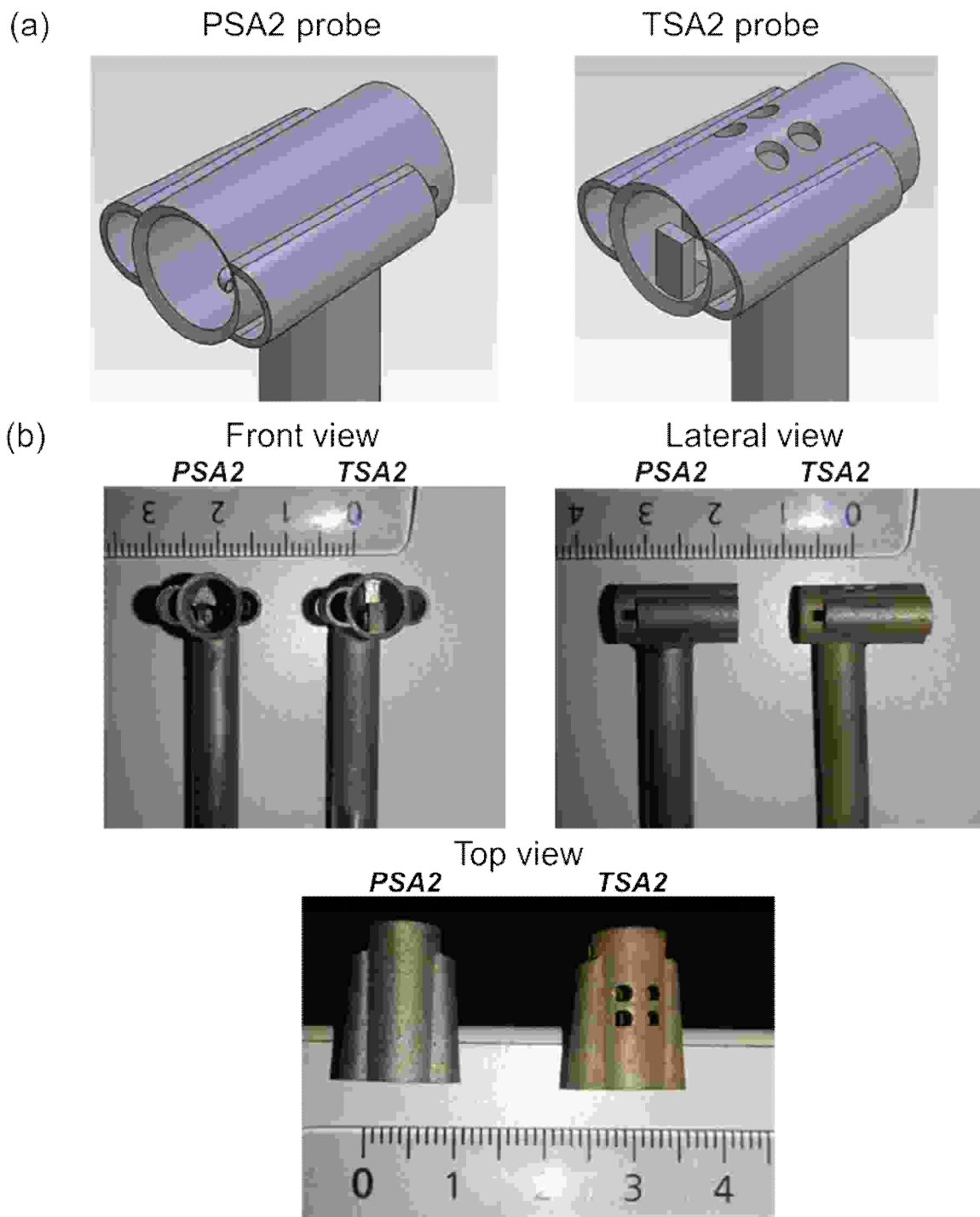
Figure 4.3: PSA2 and TSA2 probes: (a) CAD models; (b) manufactured prototypes.

4.2 Ping test

After probes manufacturing, a ping test was performed on the prototypes selected for SwRI tests. The results were compared to those obtained with the analytical model and the FEM analysis. The present section shows only the main results of the ping tests, which were executed by GE Oil & Gas.

Figure 4.4 shows the frequency response function obtained from ping test for PSA2 probe
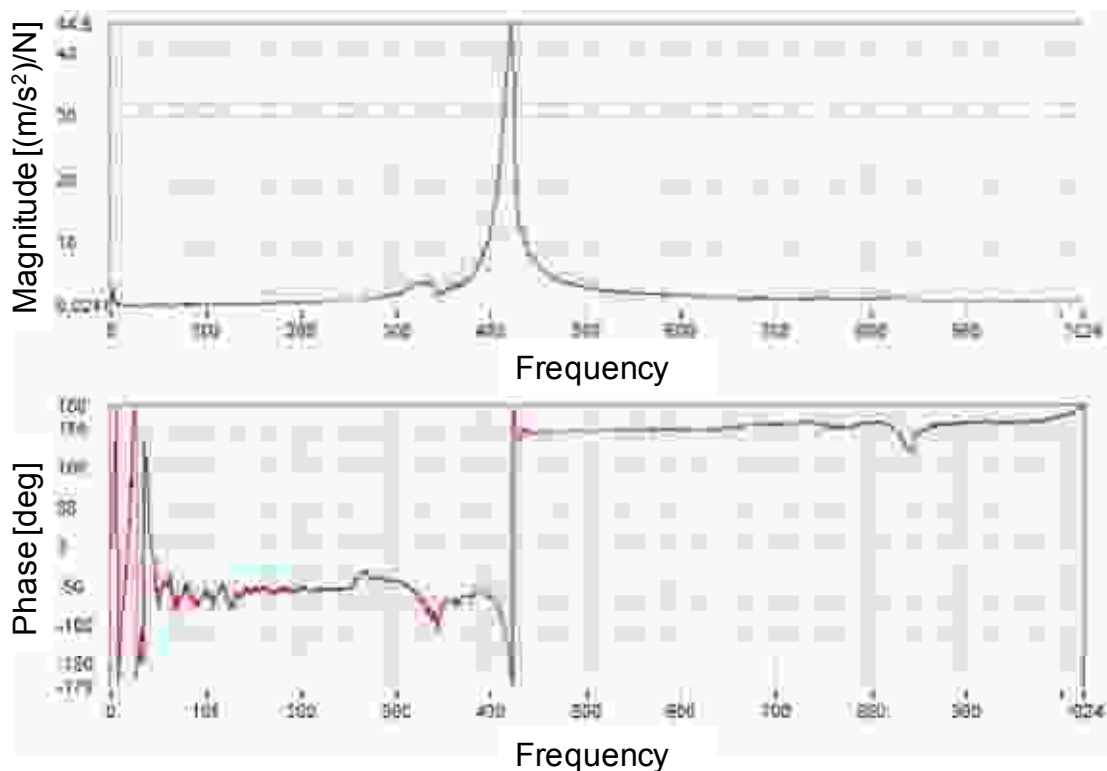
Figure 4.4: Frequency response function for PSA2 probe

The first natural frequencies obtained from ping tests for probes PSA2 and TSA2, together with those obtained with the FEM analysis and the analytical model, are listed in table 4.1:

Table 4.1: Ping tests: main results.

First natural frequency			
Id Probe	**Ping test**	**FEM analysis**	**Analytical model**
PSA2	420 [Hz]	426.5 [Hz]	449 [Hz]
TSA2	436 [Hz]	431.0 [Hz]	446 [Hz]

The results of the ping tests confirm those obtained with the analytical model and with the FEM analysis. The results of the numerical simulation are very close to those obtained with the experimental tests, while the values obtained with the analytical model are less accurate, but satisfactory

As emerges from chapter 3 and chapter 4, the model gives physically sound results, both from the structural and the fluid mechanics point of view. The structural results are confirmed also by a FEM analysis and some experimental tests. In order to completely validate the analytical model, some tests on fluid mechanics performance of probes are required. The following chapter describes some preliminary tests on probes performance, both in a dry and in a wet environment.

Chapter 5

Performance tests

The analytical model developed in the present research aims to become a simple, general and reliable instrument for wet probes design, covering all the aspects related to their design and characterization. In order to perform a complete validation, some performance tests are required. After probes manufacturing, in order to preliminary validate the model, some tests in dry conditions were carried out in the aerodynamic facility of GE Oil & Gas (Florence). The results of these tests were very interesting and similar to those obtained with the analytical model in dry conditions. After these tests, some other tests were performed in wet conditions in a facility located at SwRI. Such a facility, designed for tests on wet gas compressors, was not well suited for probes validation. The operating conditions were characterized by low velocities and low kinetic contributions. The tests gave interesting results, even if they were not sufficient to completely validate the model. Since no test rig is available for wet probes characterization, a dedicated test rig is under development. Such facility will be used to test the probes developed in the present work and to develop new designs.

The present chapter describes the performance tests on wet probes, both in dry and wet conditions. The tests results are presented, discussed and compared to those of the analytical model.

5.1 Dry conditions

The first performance tests on wet probes selected for SwRI (probes PSA2, TSA2) were performed in the dry aerodynamic facility of GE Oil & Gas (Florence). Table 5.1 shows the tests operating conditions:

Table 5.1: Performance tests (dry conditions): operating conditions.

GE Oil & Gas – Probes calibration facility	
Operating conditions	
Fluid	Air
P_0 [bar]	1.013
T [°C]	25
LVF [-]	0%
Ma [-]	0.1-0.7

As emerges from table 5.1, the operating conditions of dry tests are very different from those corresponding to probes design (Table 3.1). Since the model is a general instrument, this is not a problem. In fact, if the geometry is known, the model is not used as an instrument for probes design but for their performance prediction. In this case, the geometrical data refer to those obtained for SwRI tests and the operating conditions to those of GE dry facility.

The model was run both with the nominal and the manufactured geometry, which are compared in table 5.2:

Table 5.2: Nominal and manufactured geometry: a comparison

Id parameter	PSA2		TSA2	
	Nom. Design	**Actual geom..**	**Nom design**	**Actual geom..**
L_s [mm]	16.00	15.83	16.00	16.53
$d_{s,e}$ [mm]	8.00	7.96	8.00	8.01
$d_{s,i}$ [mm]	6.60	6.55	6.60	6.55
$A_{ph,TOT}$ [mm^2]	5.9	-	5.1	-
$A_{cd,in}/A_{cd,out}$ [-]	2.25	2.14	2.25	2.14

As emerges from table 5.2, the DMLS manufacturing process gives interesting results. The difference between the nominal and the manufactured geometry is in the order of tenths of a millimeter magnitude.

During the tests, the measurements were performed in 5 test points for total pressure probe and 4 test points for total temperature probe. The measurements refer to stationary conditions. Probes behavior in transient conditions was not investigated. The test points for total pressure probe and total temperature probe are listed in Tables 5.3 and 5.4:

Table 5.3: Dry tests on PSA2 probe: test points.

Id test point	PSA2 Probe		
	P_0 [bar]	T [°C]	Ma [-]
TP 1	1.013	25.0	0.1
TP 2	1.013	25.0	0.2
TP 3	1.013	25.0	0.3
TP 4	1.013	25.0	0.5
TP 5	1.013	25.0	0.7

Table 5.4: Dry tests on TSA2 probe: test points

Id test point	PSA2 Probe		
	P_0 [bar]	T [°C]	Ma [-]
TP 1	1.013	25.0	0.3
TP 2	1.013	25.0	0.5
TP 3	1.013	25.0	0.6
TP 4	1.013	25.0	0.7

Referring to total pressure probe, the pneumatic signal was acquired and processed by a 15 PSI Rosemount transducer. The measurement uncertainty, which was the 0.02 percent of the instrument full scale, corresponded to a value of 20 Pa. A comparison between the results of the analytical model and the experimental tests was performed in terms of recovery factor (Fig. 5.1). In order to discuss the results, we call *measured recovery factor* the result obtained from the experimental data, and *calculated recovery factor* the one estimated with the analytical model.

The curves of recovery factor (Fig. 5.1) show a very good agreement between analytical and experimental data for total pressure probes. Starting from the analytical model, the red and the green curves respectively represent the recovery factor calculated with the model, associated with the nominal and the manufactured geometry. The two curves are very similar; in fact, the DMLS manufacturing process ensures a high resolution.
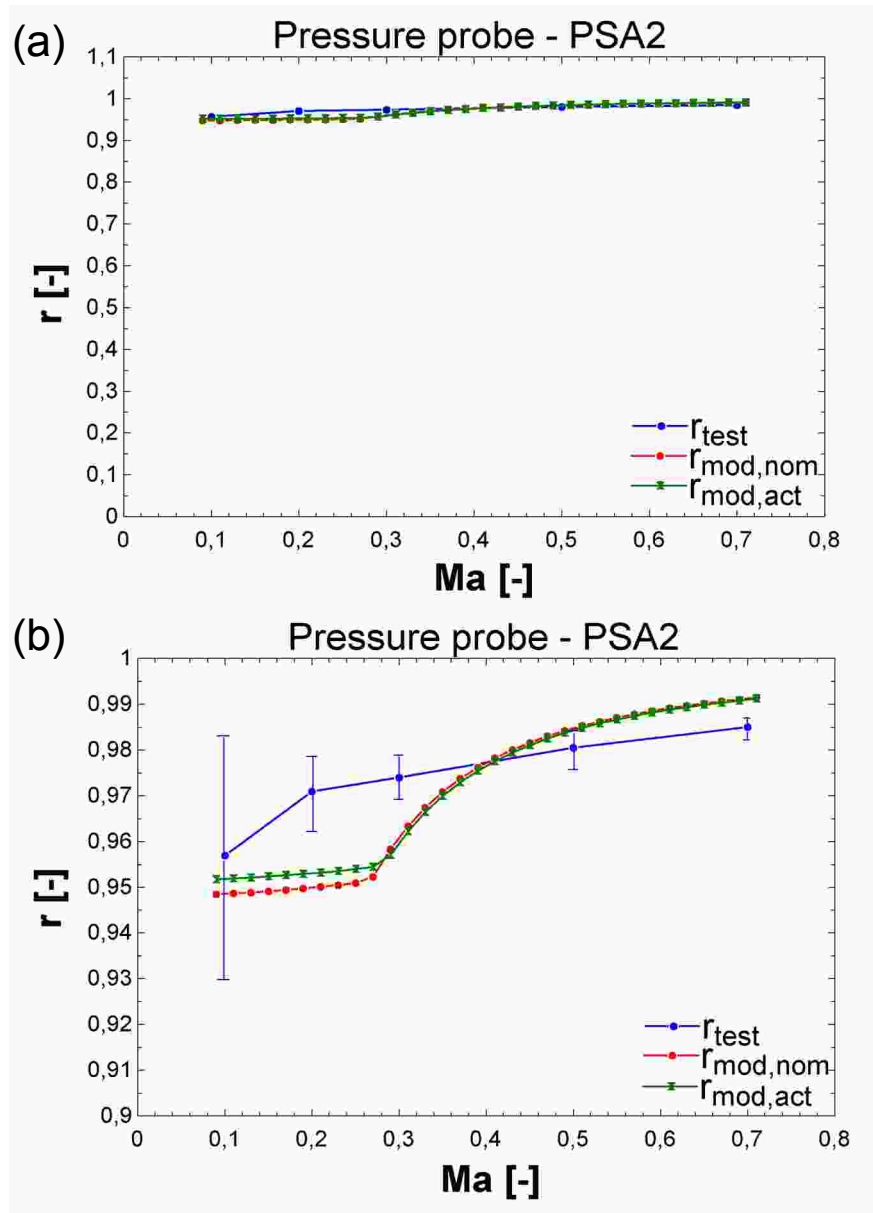
Figure 5.1: Comparison between measured and calculated *r* – *PSA2 probe*. (a) vertical scale between 0 and 1; (b) zoom on vertical scale.

The measured *r* assumes values which are very close to those obtained with the analytical model. The maximum relative error between measured and calculated *r* is lower than 3%.

The curves of calculated *r* show an interesting behavior (Fig 5.1b): for low values of Mach number *r* has a weak dependence on *Ma*. In fact, in this region, the converging ducts are not choked. If the flow velocity increases, the kinetic term becomes higher but the purging holes effect increases too. The gas velocity inside the shield increases, leading the recovery factor to be almost constant. Once the converging ducts are choked, the pressure condition

at their outlet becomes constant and the purging hole effect is constant too. In this region, an increase in the value of *Ma* leads to an increase in *r*.

The curves of measured and calculated *r* show similar trends, even if there is a certain difference for low values of *Ma*. In this region, the measurement uncertainty has a great influence on the measured recovery factor. The transition between subsonic and sonic conditions at nozzles outlet does not emerge clearly from experimental data. A numerical analysis will help to understand what happens in this region.

Total temperature probe was provided with a standard K thermocouple. The measurement uncertainty of the system was 0.5 Kelvin. A comparison between measured and calculated *r* is shown in Fig. 5.2.

As for total pressure probes, the calculated *r* for nominal and manufactured geometry have the same trend and very similar values.

The measured and calculated *r* have also similar values, especially for high Mach numbers. The maximum relative error between measured and calculated *r* is lower than 7%. The measurement uncertainty plays an important role in the case of total temperature probes, especially for low values of *Ma*. As emerges from Fig. 5.2b, all the calculated *r* are inside the uncertainty measurement range.

The curves of measured and calculated *r* show a similar trend. Since *Ma* is higher than 0.3, the probe operates in the region where the converging ducts are choked.
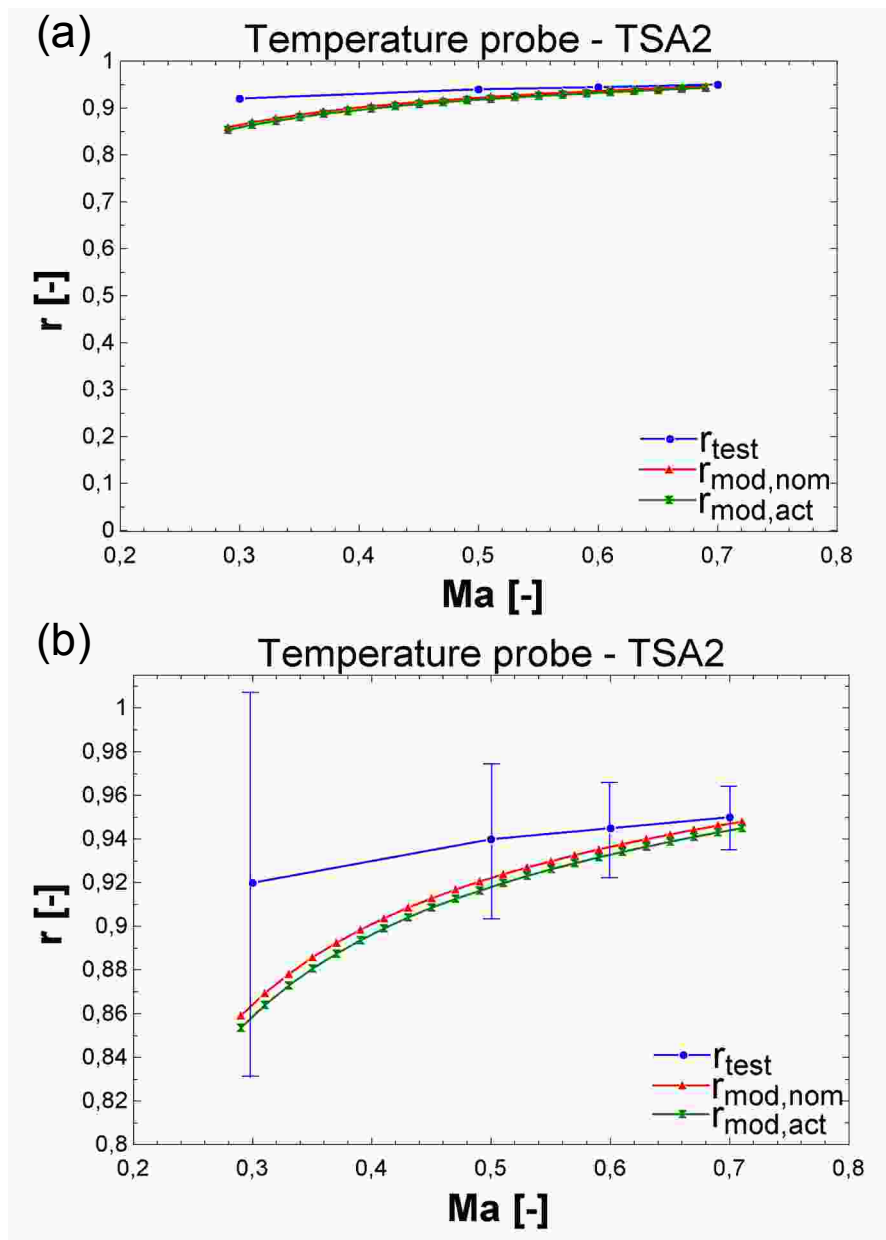
Figure 5.2: Comparison between measured and calculated *r – TSA2 probe*. (a) vertical scale between 0 and 1; (b) zoom on vertical scale.

The first tests performed in a dry environment confirmed that the model seems to be a reliable instrument for probes design and characterization. During the tests, the probes always operated in off design conditions. In fact, the operating conditions were very different from probes design points and the operating fluid was not a wet mixture but a dry gas. The model gave interesting results in terms of recovery factor, especially for high values of Mach number. The highest errors between the analytical and experimental results

were obtained for total temperature probes at low Mach numbers. However, in this region the measurements uncertainty had a great influence on the results.

The first preliminary tests in dry conditions validated the model, which required a further validation in wet conditions.

5.2 SwRI tests

After the first tests discussed above, some other tests in wet conditions have been performed in the facility located at SwRI. This facility [57] is a large-scale wet gas loop, used to measure compressor and loop operation for wet gas flow. The wet gas flow loop, which is designed to test centrifugal compressors in wet gas conditions, can operate with air, nitrogen and CO2 as the gas phase, and with water as the liquid phase. The maximum pressure at compressor suction is 300 psia and the maximum LVF is 5%. The SwRI facility, which was specifically designed for tests on centrifugal compressors, was considered an important opportunity to test the probes developed in the present work, even if the test conditions were not completely suitable for wet probes validation. As emerges from Table 3.1, the flow velocity is lower than 30 m/s, which leads to Mach numbers of gas phase lower than 0.1. In such conditions, the pressure and temperature kinetic contributions are very low and comparable with the measurement uncertainty (0.01 bar for pressure measurements and 0.5 K for temperature measurements). For this reason, the results of these tests can be considered only preliminary. However, no wet facility for probes validation was available during the research activity, and the SwRI test rig represented a good solution to perform tests. Such tests are an opportunity to see how the probes respond in a wet environment from the fluid mechanics and the structural point of view, and if the model gives reasonably good results. Fig. 5.3 represents an overall view on the SwRI test loop [57]:
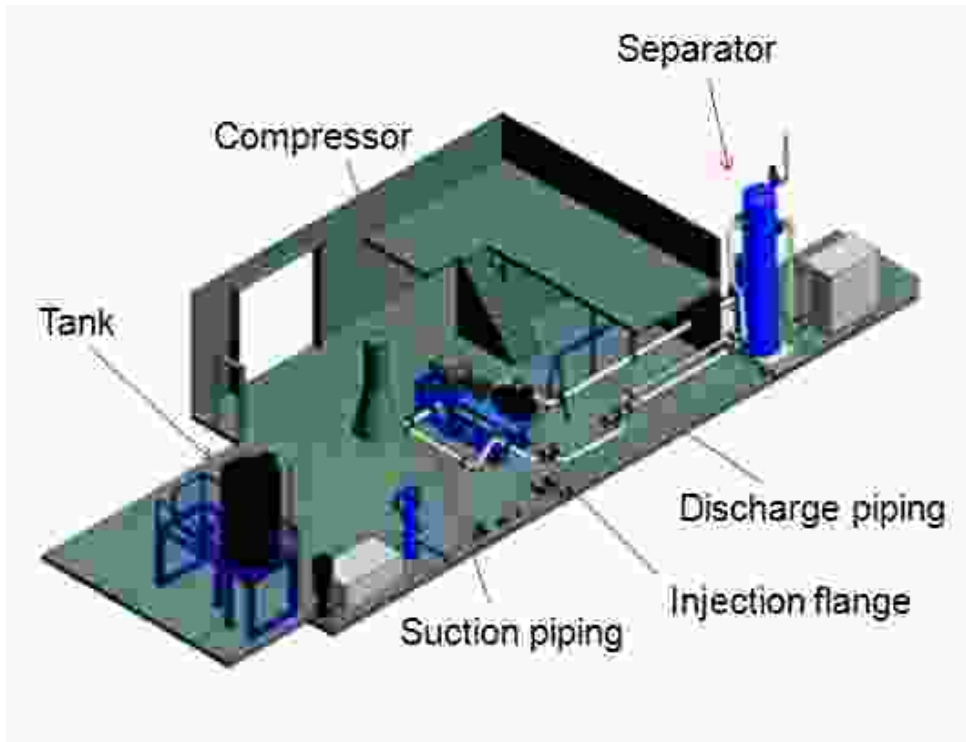
Figure 5.3: SwRI test loop; overall view (adapted from [57])

Fig. 5.4 represents an overview of test components inside of test building:
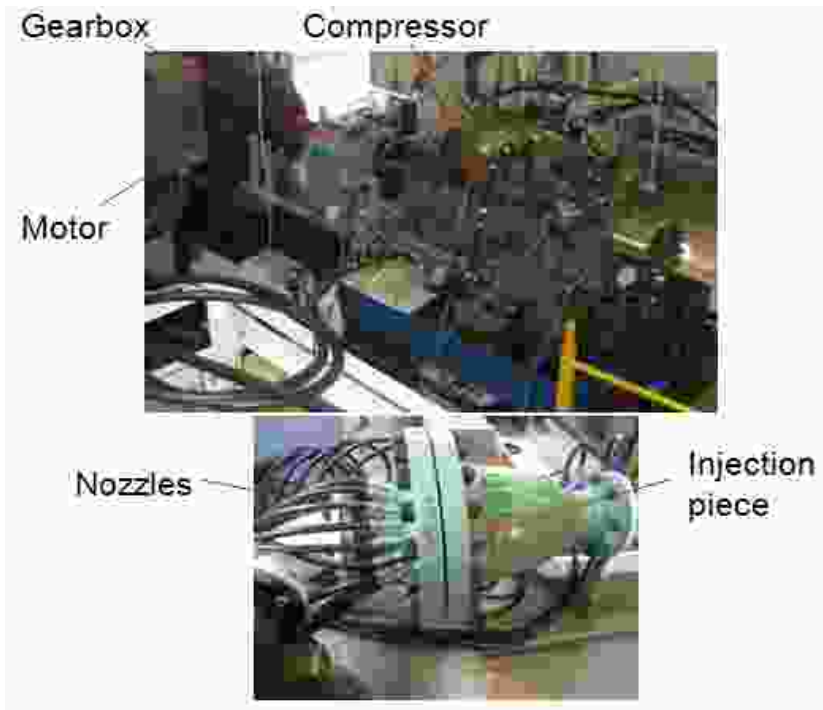
Figure 5.4: SwRI test loop: main components inside test building.

Fig 5.5 represents the measurement position of conventional and new probes during SwRI tests.
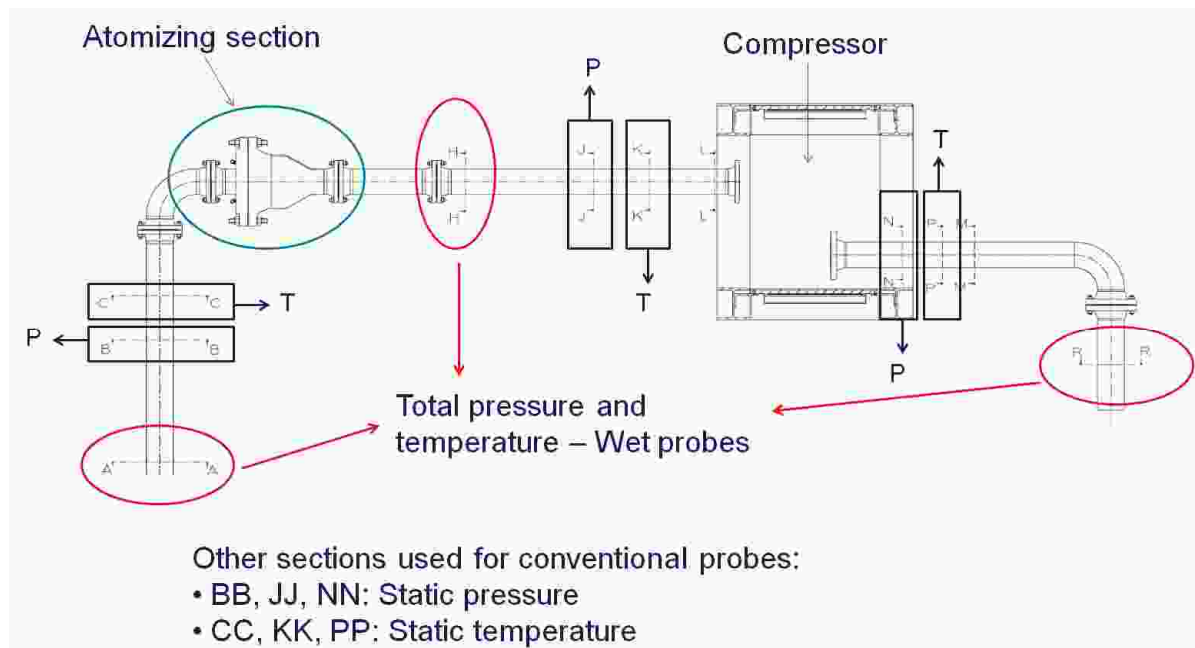
Figure 5.5: SwRI test loop: measurement positions of conventional and new probes.

As emerges from Fig. 5.5, the wet probes are located at compressor suction, both before and after the atomizing section, and at compressor discharge. The other sections are used for conventional probes (P and T respectively stand for conventional pressure and temperature probes). Fig. 5.6 represents the assembly drawing for standard and wet probes:
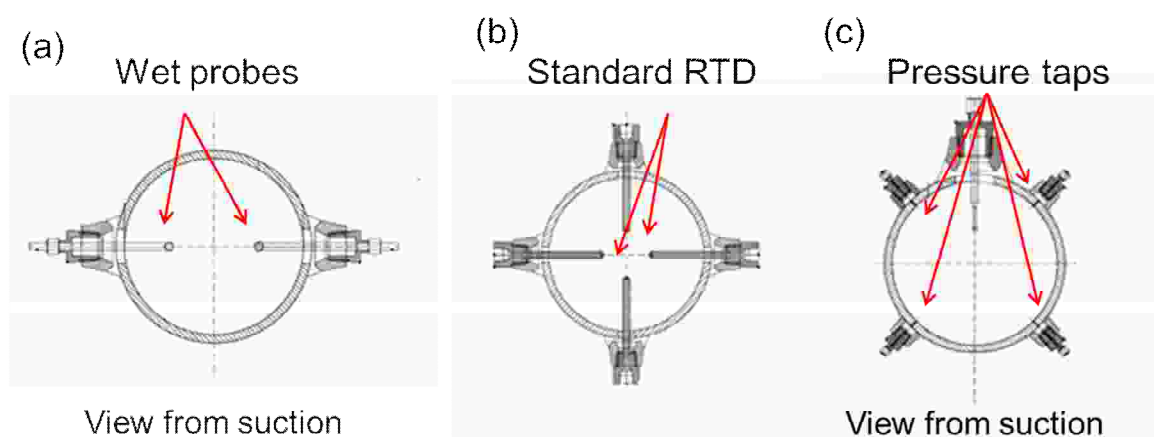
Figure 5.6: Standard and wet probes: assembly diagram. (a) meas. section AA; (b) meas. section CC; (c) meas. section BB.

Each measurement section for wet probes has a total pressure and a total temperature probe. The uncertainty is 0.01 bar for pressure measurements and 0.5 K for temperature measurements. The static temperature is measured with standard RTDs. Each section has four RTDs, whose signals are acquired and post processed, in order to obtain the average value of static temperature. The measurement uncertainty is 0.06 K. Finally, four static pressure taps are used for pressure measurement, with a corresponding uncertainty of 0.005 bar. Fig. 5.6c shows also a standard Pitot probe for the measurement of total pressure in section B-B. Since the probe was broken during the tests, it wasn't used.

Several tests were performed on the centrifugal compressor, changing the values of static pressure at compressor suction, Liquid Volume Fraction, compressor speed, difference between the temperature of liquid and dry phase, etc. The measurements were performed both in stationary and transient conditions. Since the test target was the compressor characterization, it wasn't possible to prepare a design of experiment for probes testing. The following sections show the main results of SwRI tests, both for total pressure and total temperature probes. The data refers to the wet probes located in section H-H, downstream the atomizing section.

5.2.1 Total pressure probes

This paragraph presents the results of total pressure probes during the SwRI tests. The data refer to wet probes located in section H-H. Fig. 5.7 refers to some tests performed in dry conditions, with a pressure of 18 bar and a velocity between 8 and 17 m/s, which corresponds to a *Ma* lower than 0.050. The blue line (P_0-P) represents the difference between the total and the static pressure of gas phase; such a value is calculated from test conditions by GE tools. The red line (P_{calc}-P) represents the recovered kinetic pressure, calculated from the analytical model. Starting from test operating conditions and probe geometry, the model calculates the recovered kinetic pressure. Finally, the green line (P_{meas}-P) represents the difference between the pressure measured by the wet probe and the static value. It is the real kinetic term recovered by the probe during the tests.
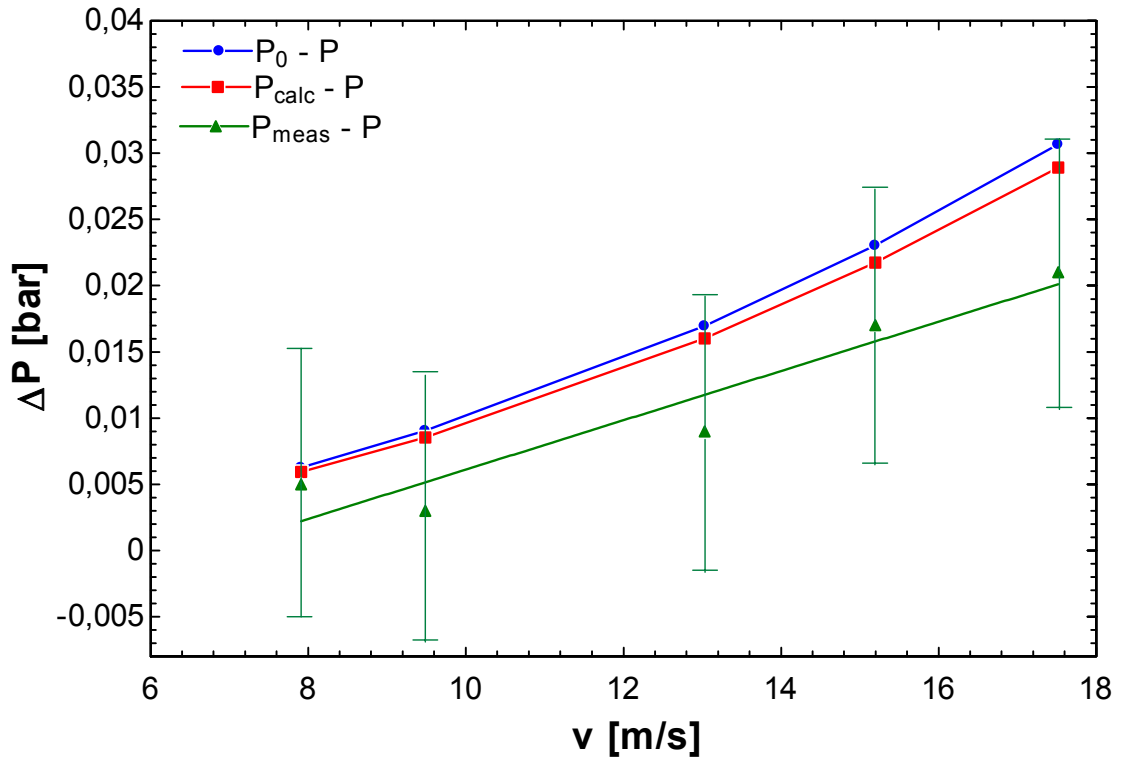
Figure 5.7: SwRI tests, dry conditions: comparison between measured and calculated probes performance.

As emerges from Fig 5.7, the kinetic term is in the order of magnitude of the measurement uncertainty. Considering the measurement uncertainty, the analytical and experimental curves seem to overlap; from these considerations one can conclude that the model gives physically sound results.

Figs 5.8 and 5.9 show the results of total pressure probe in wet conditions. These tests were performed varying LVF, which was between 0.5 and 3%. The velocity was very low ($v < 7$ m/s) and the associated kinetic term was always lower than the measurement uncertainty. The experimental results for a LVF of 2% are not reported because the measurement point was not stable and the data could not be used. As emerges from Fig. 5.8, analytical and experimental results show similar trends. The estimated values are different from those calculated, but this is induced by the measurement uncertainty. The results have also been represented in terms of recovery factor (Fig. 5.9), leading to the same considerations.
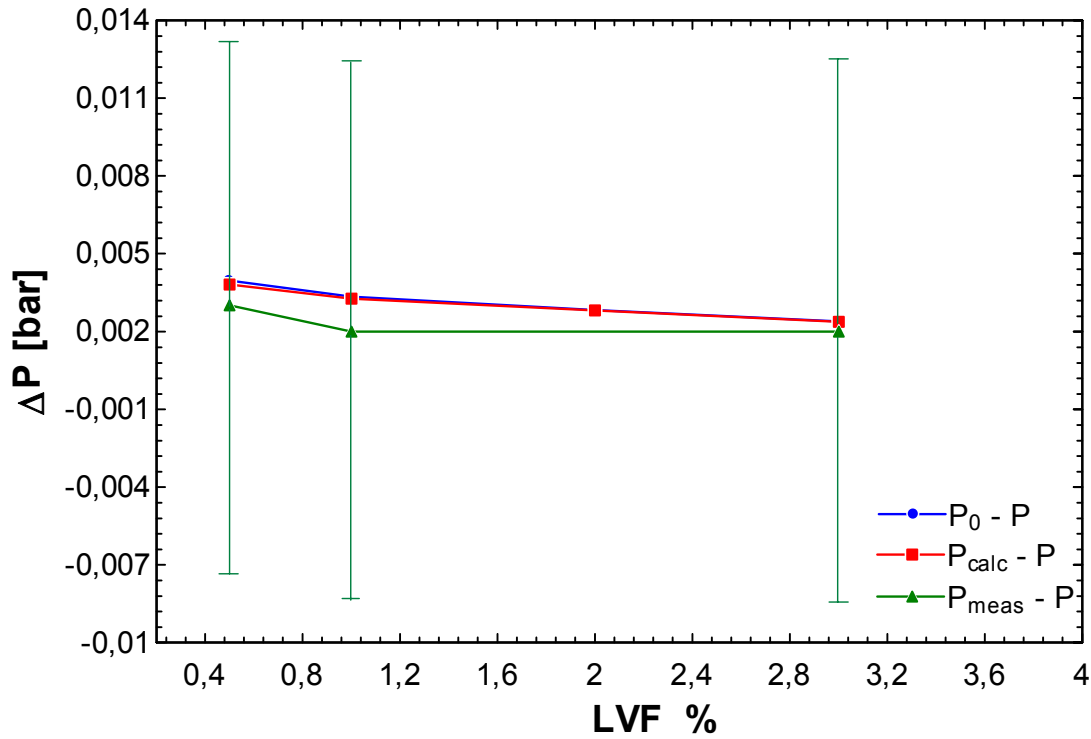
Figure 5.8: SwRI tests, wet conditions: a comparison between measured and calculated probes performance.
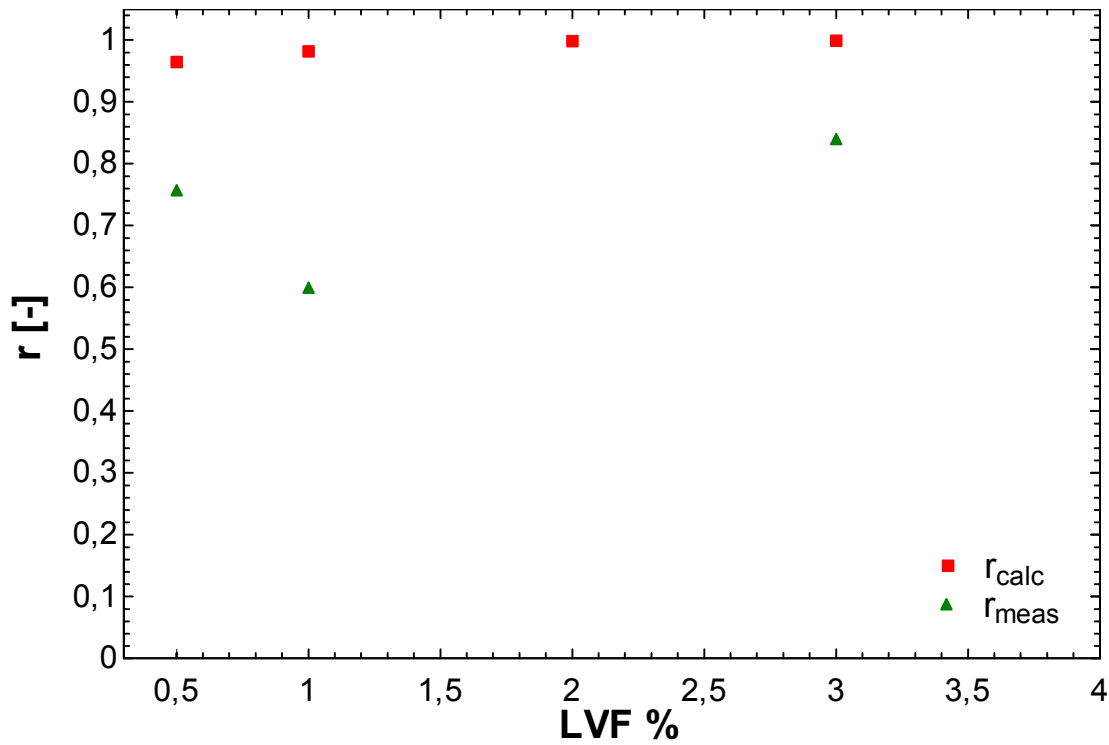
Figure 5.9: SwRI tests, wet conditions: a comparison between measured and calculated recovery factors.

The results obtained from SwRI tests are very interesting. Good results have been obtained both in dry and wet conditions. The analytical and experimental results always show the same trend, confirming that the model gives physically sound results. However, the measured data are different from those calculated with the model, but this is the consequence of test conditions.

5.2.2 Total temperature probes

This paragraph presents the results of total temperature wet probes during SwRI tests. As for total pressure probes, the data refer to wet probes located in section H-H. The very low kinetic term and the thermocouple uncertainty make the total temperature probes characterization meaningless in terms of recovery factor. The kinetic term, for these tests, is always lower than 0.15 K, and the thermocouple uncertainty is 0.50 K. For this reason, a direct comparison between the temperatures measured by a wet probe and standard RTDs in two close positions (section H-H and section K-K) and in the same test conditions is presented.

Starting from dry conditions, the blue circles in Fig 5.10 represent the average temperatures measured by four RTDs in section KK. The temperature calculated by the analytical model, from test conditions and probe geometry, is represented with the red squares. The green triangles indicate the temperatures measured by the wet probe.

Referring to Fig 5.10, the total temperatures calculated by the model are very close to those obtained with the standard sensors. The model gives physically sound results; in fact, the difference between the calculated total temperatures and the static measured values (RTD) increases with the flow velocity and consequently with the temperature kinetic term. Good agreement seems to exist between analytical and experimental results; wet probes readings and calculated values have the same trend, even if wet probes seems to be affected by a constant offset of 0.15 K. Since this value is inside measurement uncertainty, no definitive conclusions are possible.
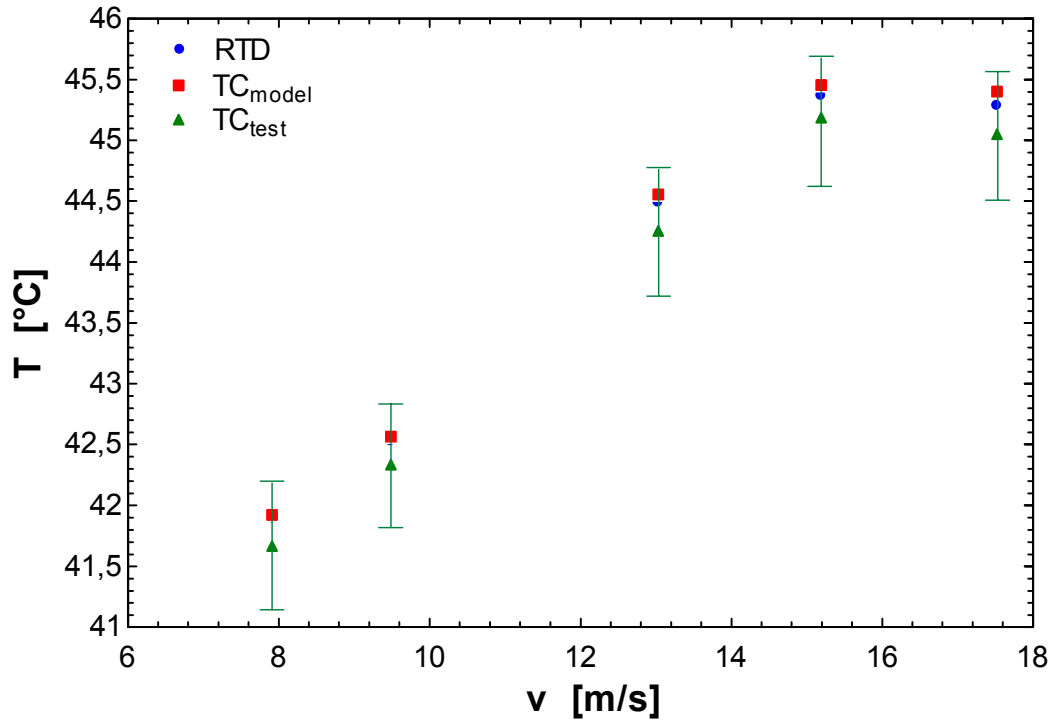
Figure 5.10: SwRI tests, dry conditions: a comparison between standard RTDs and wet probe.

Fig 5.11 shows the results of total temperature probe in wet conditions:
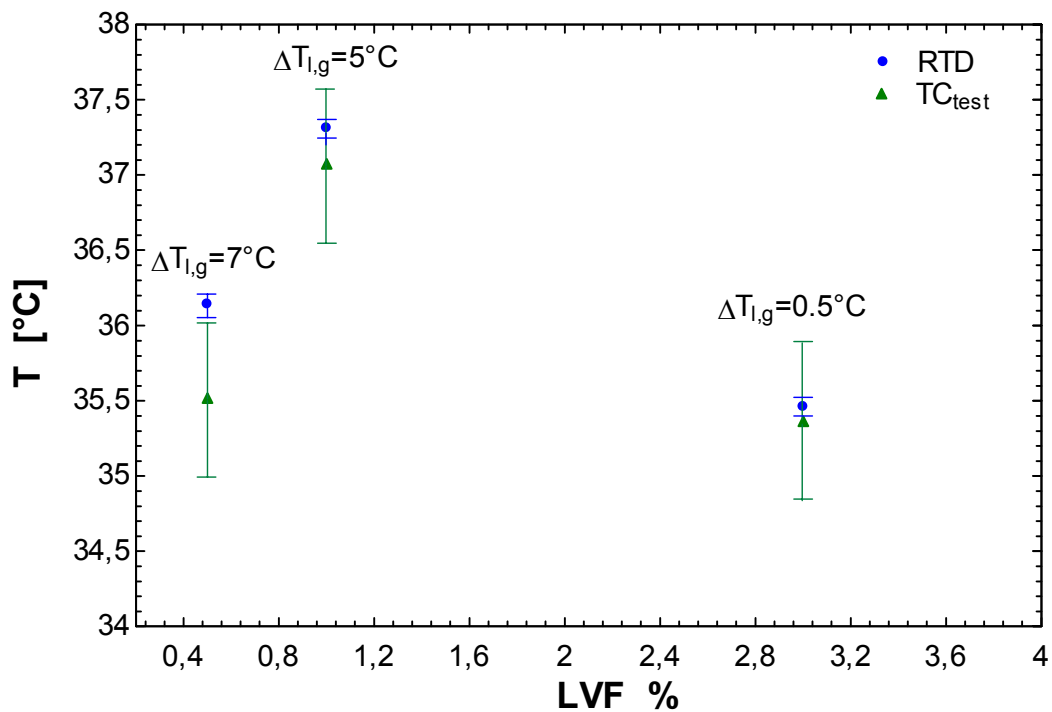
Figure 5.11: SwRI tests, wet conditions: a comparison between standard RTDs and wet probe.

The post processing of wet data is more difficult than that of tests in dry conditions. Fig. 5.11 refers to wet tests; the *LVF* is between 0.5 and 3% and the temperature of liquid phase is different from that of gas phase. In this test the gas phase is colder that the liquid phase. As the *LVF* increases, the difference between T_l and T_g decreases. An important issue related to tests in wet conditions is the lack of reference for static temperature of liquid phase downstream the atomization. In fact, the temperature of liquid phase is measured downstream the high pressure pump which pressurizes water for the sprays, but no temperature is measured downstream the atomization section. The model can be run with the static temperature of gas phase and the liquid temperature downstream the high pressure pump, but the results are not completely reliable. For this reason, the comparison is made only between the temperatures measured by standard RTDs and wet probe.

The wet probe gives a temperature which is lower than RTD in all the cases. The difference is higher than the constant offset between them. Since T_g is lower than T_l, the wet probe appears to be less affected by the presence of water droplets with respect to the RTDs. As the LVF increases and the difference between the temperatures of the two phases decreases, the two sensors give very similar results. It seems that, for high values of LVF, wet probes are affected by the presence of droplets. From this results it is not clear if the probe works well. In fact, the results are affected by the measurement uncertainty and by the offset, and there is no reference temperature for water downstream the atomization.

Before concluding with the results of SwRI tests, a short discussion on total temperature probes in transient tests is proposed. The transient tests consisted in a step variation of the *LVF*, which is changed from 0 to a value set by the test for a few seconds. The operating conditions for the main tests are listed in table 5.5. The acronym *TT* stands for transient test.

Table 5.5: Transient tests: main operating conditions

Transient tests				
	P [bar]	**$\Delta T_{l,g}$ [°C]**	**v_g [m/s]**	**LVF %**
TT 1	18.5	-5.0	12.5	0-0.50
TT 2	18.5	-4.5	11.0	0-2.00
TT 3	18.5	-2.0	10.0	0-5.50

Fig. 5.12 represents the results of the transient tests.
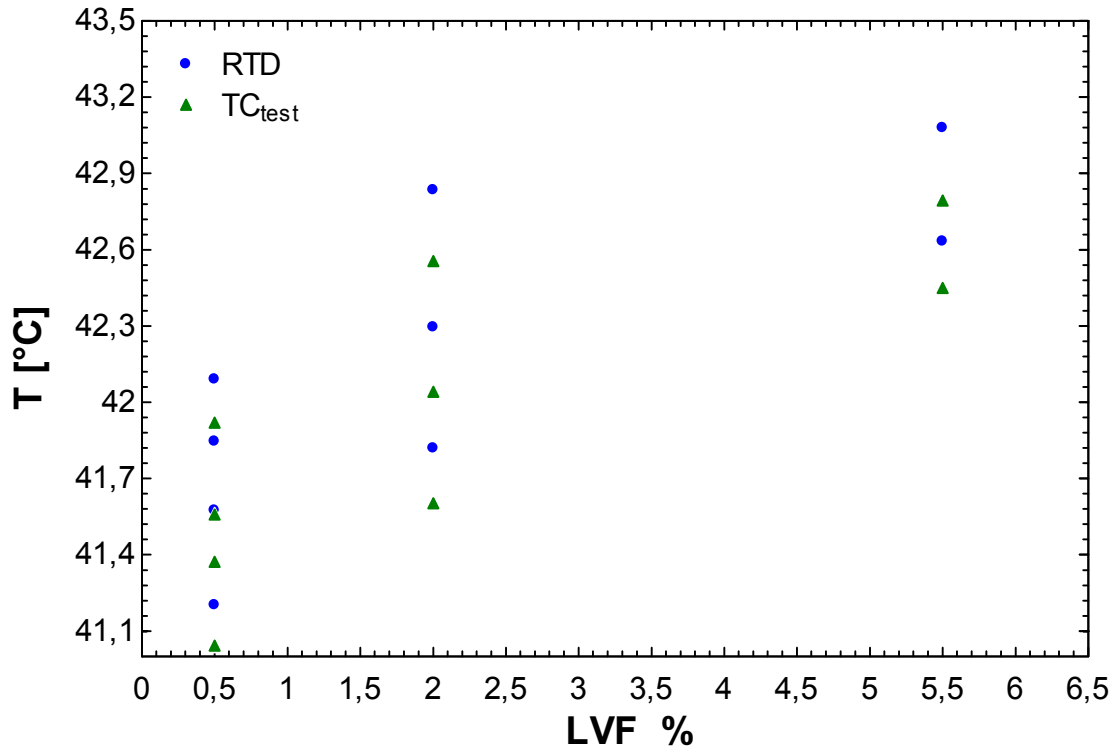
Figure 5.12: Transients tests: comparison between standard RTDs and wet probe measurements.

The results of transient tests are different from those obtained by wet measurements in stationary conditions. As emerges from Fig. 5.12, probes behavior is similar to those obtained for dry conditions (Fig. 5.10). Wet and conventional probes measure both intermediate temperature between liquid and gas phase and give very similar results. The only difference is caused by the measurement offset between the two probes. This can be caused by tests conditions, which lead the two phases to assume the same temperature, by a malfunction of wet probes or by the conductive heat transfer towards wet probe stem. Since RTDs, which are heavily affected by the presence of water, and wet probes give the same temperature, one can expect that also wet probes are affected by water, and that the mini shield doesn't work well. As previously discussed, transient tests give interesting results, but it's impossible to understand if the wet probes are really affected by the presence of water or not. In order to better understand probes behavior a dedicated facility is under development.

5.3 Concluding remarks

The present chapter describes the results of performance tests on wet probes, which assume a fundamental importance to validate the model. The first tests were performed in a dry environment; they gave very interesting results, validating the model and confirming that it is a reliable instrument for probes design. The tests performed in wet conditions gave some indications, even if the SwRI facility was not suitable for complete probes validation. The kinetic term was lower than the measurement uncertainty in most the cases. However, these tests gave some qualitative indications on probes behavior in wet conditions.

Total pressure probes had an interesting behavior. The analytical and experimental results showed the same trend, even if the measured data were different from those calculated from the model. This was a consequence of the low kinetic term, which had the same order of magnitude of the measurement uncertainty.

Total temperature probes gave interesting results in dry conditions; analytical and experimental results had the same trend, even if wet probes readings didn't agree with the model. Wet probes were affected by measurement uncertainty, which was lower than kinetic term in most the cases; the *TC* readings were always lower than RTDs by a constant offset of 0.15 °C. The results of wet tests were more difficult to post-process than those in dry conditions. The measurement uncertainty was accompanied by a lack of reference for T_l downstream the atomization. From the results of wet tests in stationary conditions, it seemed that wet probes were less affected by water droplets than standard RTDs, but the same behavior didn't emerge from transient tests, were the only difference between probes was the measurement offset. From SwRI tests it in not possible to understand if total temperature wet probes work well. For this reason, probes response must be investigated with a dedicated facility, which is under development. Since the model gives reasonably good results for total pressure probes in dry and wet conditions, and for total temperature probes in dry conditions, it can be considered only partially validated. The complete model validation will be performed after wet test in the dedicated facility.

The current and the previous chapters of the present work deal with the development of probes for the measurement of total pressure and total temperature of gas phase in wet

environments. After the presentation of probes conceptual design, the analytical model for their design, the simulation and the tests in dry and wet conditions, it's important to discuss how the probes can be improved and miniaturized. One of the most interesting approach for probes improvement and miniaturization is represented by the use of superhydrophobic materials.

The following chapter is a general introduction to superhydrophobic materials for industrial application. After a first part on the physical principles and the simplest mathematical models to describe hydrophobicity, the main manufacturing approaches are discussed.

The following chapter is the basis for future developments, which focuses on the research of these materials and their application on wet probes. The availability of the wet test facility has a fundamental importance for this activity. In fact, such test rig allows to perform some tests on new solutions. If the physical principle works well with air and water, further developments will deal with oleophobic solutions and their application in real wet gas environments.

Chapter 6

Superhydrophobic materials for industrial application: an introduction

The methodology developed and partially validated in the present research activity is a basic instrument for the fluid mechanics and structural design of wet tolerant probes for the measurement of total pressure and total temperature in wet gas conditions. After probes design, manufacturing and testing, some efforts were made to understand which the best technologies to improve probes performances and miniaturize their design are. One of the most interesting approach is represented by superhydrophobic materials.

Superhydrophobic surfaces are characterized by an extremely low wettability; when a water droplet approaches such a surface, it slips away without wetting it. Superhydrophobic materials and nanotechnology represent a very interesting challenge for the development of optimized probes and sensors, which can measure the thermodynamic properties of the gas phase without being affected by the wet phase. The first step at this proposal is the study of superhydrophobic materials and their potential applications to wet probes. Then, such materials must be applied to wet probes, in order to obtain supehydrophobic probes. Finally, the probes must be tested. At this proposal, the wet facility which is under assembly represents a fundamental instrument to perform this research. If the physical principle gives interesting results with a mixture of air and water, it will be interesting to study oleophobic material for specific wet gas applications, where the mixture is composed of hydrocarbon gases, liquids and water.

This chapter is an introduction to superhydrophobic materials for industrial application; the first part relates to materials hydrophobicity, main parameters and classical approaches to describe it. The second part focuses on the most important manufacturing processes to obtain superhydrophobic surfaces. The present chapter is the basis for future developments.

6.1 Superhydrophobicity: fundamental concepts and physical models.

Wettability is a fundamental issue in the engineering analysis of surfaces; generally, two limit conditions are considered in the industrial application. The first condition is the complete wettability of a surface, which is called hydrophilicity. When a surface has a high hydrophilicity, the droplets which approach it do not preserve their spherical shape and form a thin film on the surface, which becomes wet. When a surface is hydrophobic, the droplets tend to preserve their spherical shape, limiting their contact with the surface, which remains dry or becomes partially wet. Fig. 6.1 is a schematic representation of a hydrophilic and a hydrophobic surface.

Hydrophilic surface   Hydrophobic surface

Figure 6.1: Hydrophilic and hydrophobic surfaces: a schematic representation

The wettability of surfaces depends on the surface energy of the material and the surface roughness. The basic concepts of superhydrohobic surfaces can be found in [58-60]. The first fundamental parameter is the contact angle θ. When a droplet of water rests on a surface, there is a contact angle measured at the edge of the droplet. It can be defined as the tangent angle of the liquid-vapor interface at the three-phase boundary. Surface tension γ can be regarded as a force per unit length and is given in units of N m^{-1} or as energy per unit area J m^{-2}. When a droplet of water rests on a solid surface, three interfaces become relevant and provide interfacial tensions:

- Liquid vapor interface γ_{LV}
- Solid-vapor interface γ_{SV}
- Solid liquid interface γ_{SL}

The balance among these three interfacial forces determines the behavior of the droplet on the surface.

The basic models relate the wettability of surfaces to interfacial tensions, contact angle and surface roughness. The starting point of a wetting model is defined by the Young equation [61], derived for a sessile drop on an ideal rigid, homogeneous, flat and inert surface (Fig.6.2):
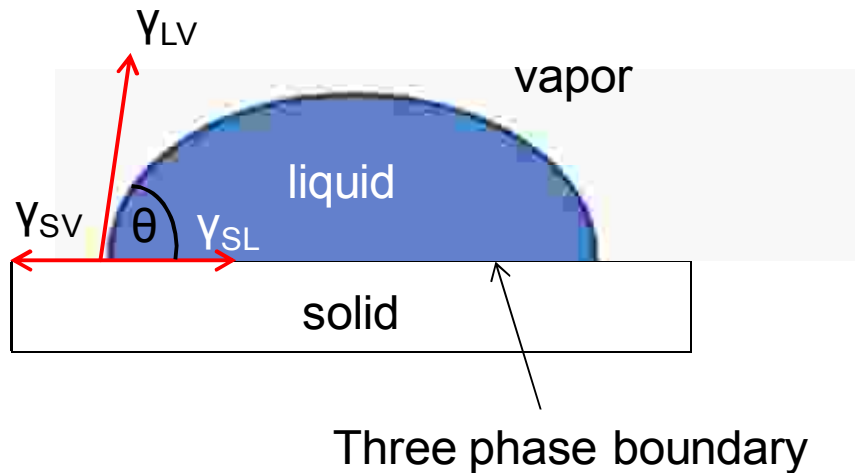
Figure 6.2:Schematic of a liquid droplet in contact with a smooth surface.

Referring to Fig. 6.2, the Young model relates θ to interfacial tensions γ:

$$\cos\theta = \frac{\gamma_{SV} - \gamma_{SL}}{\gamma_{LV}} \tag{6.1}$$

Young model does not take into account surface roughness, which has a great influence on surfaces wettability. Fig. 6.3 is a schematization of surface roughness and wetting of four different surfaces [62]:
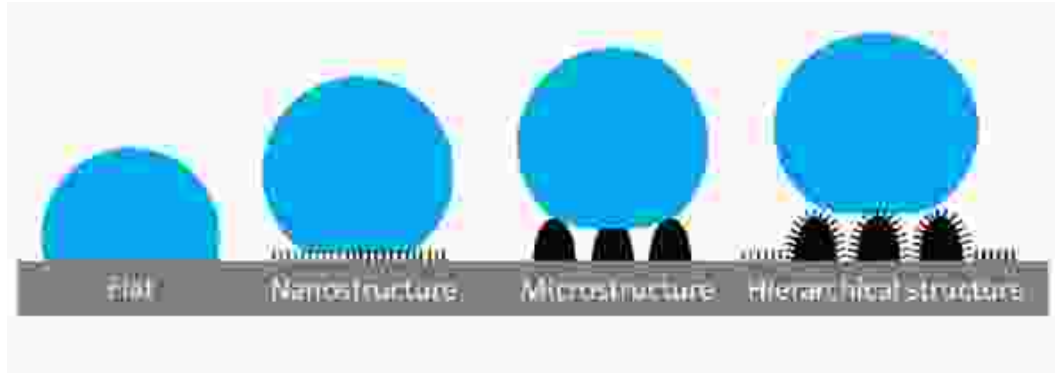
Figure 6.3: Surface roughness and wetting of four different surfaces: a schematization [62].

As emerges from Fig. 6.3, the largest contact area between the droplet and the surface is given in flat and microstructured surfaces, is reduced in nanostructured surfaces and minimized in hierarchical structures. An hierarchical structure combines micro-scale and nano-scale rugosity. In order to consider the effect of surface roughness on the contact angle, two models were proposed:

- Wenzel model
- Cassie-Baxter model

The Wenzel model [63-64] assumes that the water penetrates into the grooves caused by the surface roughness and that the contact between the water and the solid surface is homogeneous. In the Cassie-Baxter model [65-66] the droplet is suspended on the roughness asperities and the contact between the droplet and the solid surface is heterogeneous. The space between the droplet and the solid surface is filled with air bubbles. Fig. 6.4 is a schematic representation of Wenzel and Cassie-Baxter states.

Starting from Wenzel model, the contact angle can be defined as a function of the Young contact angle (eq. 5.1) and a roughness factor *r*:

$$\cos\theta^W = r\cos\theta \qquad\qquad (6.2)$$

r corresponds to the ratio between real surface area and the smooth surface area. The subscript *W* stands for *Wenzel model*. As emerges from eq. 6.2, surface roughness influences wettability. In fact, if a surface is hydrophilic ($\theta < 90°$), the surface roughness makes it more hydrophilic; conversely, if a surface is hydrophobic ($\theta < 90°$), it makes it more hydrophobic.
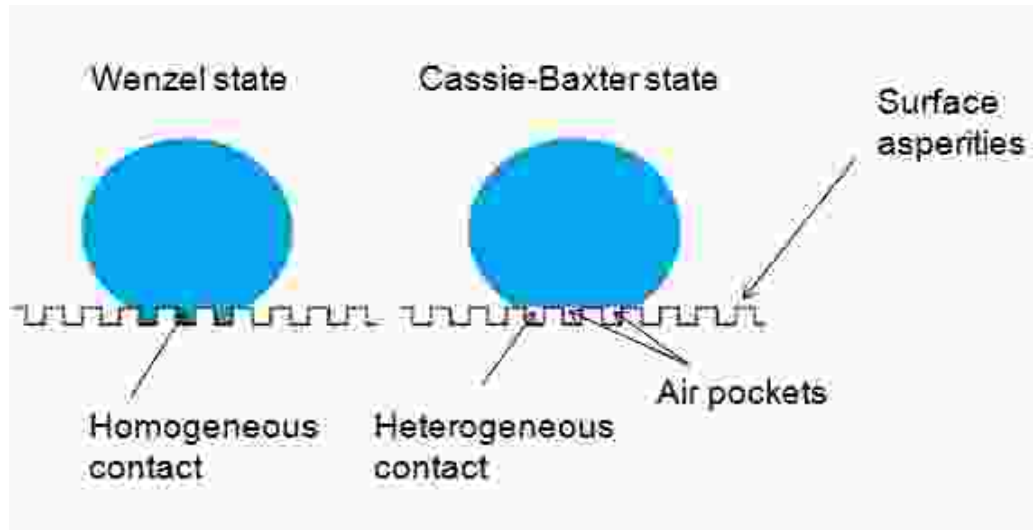
Figure 6.4: Liquid droplet on a rough surface: schematization of Wenzel and Cassie-Baxter states (adapted from [62]).

The Cassie-Baxter model defines the contact angle as a function of the Young contact angle (eq. 6.1) and a roughness factor *f*. As previously explained, a heterogeneous contact occurs between the droplet and the solid surface in Cassie-Baxter model. A partial contact area between droplet and solid surface A_{LS} and a partial contact area between droplet and air A_{LG} can be defined. The associated *roughness factor f* is calculated as it follows:

$$f = \frac{A_{LS}}{A_{LS} + A_{LG}} \tag{6.3}$$

The Cassie-Baxter contact angle θ^{CB} is defined as it follows:

$$\cos\theta^{CB} = -1 + f(\cos\theta + 1) \tag{6.4}$$

As emerges from what discussed above, the surface roughness influences surfaces wettability. The Young model builds up the basic theory for wetting phenomena on ideal smooth surfaces. The Wenzel model is valid if the surface is homogeneously wetted, and the Cassie-Baxter model is applied to the heterogeneous state. A common characterization of surface wettability can be performed using the contact angle (table 6.1). Young model, together with those of Wenzel and Cassie-Baxter are an interesting theoretical support to understand the basic principles of surfaces wettability. However, the problem is more complex and a lot of other aspects need to be investigated, for example when and how a

115

wetting state can be achieved. Another interesting issue deals with the transition between a wetting state and the other, and how this transition happens. The theories mentioned above are necessary but not sufficient to describe the complex physics of surfaces wettability.

Table 6.1: Characterization of surface wettability as a function of contact angle

Contact angle	Surface type
$\theta < 10°$	Superhydrophilic
$10° < \theta < 90°$	Hydrophilic
$90° < \theta < 150°$	Hydrophobic
$\theta > 150°$	Superhydrophobic

Another fundamental parameter to define a superhydrophobic state is the contact angle hysteresis *CAH*, which is a measure of energy dissipation during the flow of a droplet on a solid surface. In order to define this parameter, one must define the advancing contact angle θ_A and the receding contact angle θ_R. Fig. 6.5 is a schematic representation of a drop sliding on a tilted plane [59].
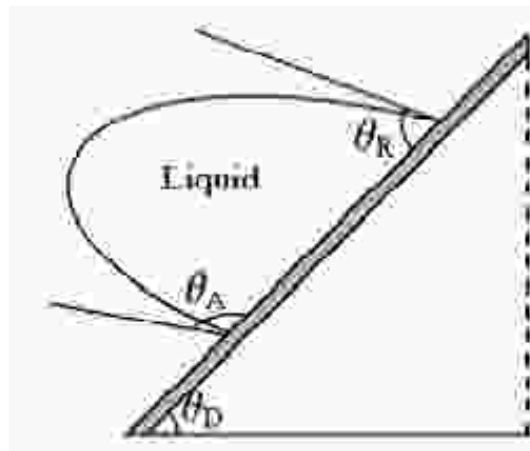
Figure 6.5: Schematic representation of a drop sliding on a tilted plane [59]

Referring to Fig. 6.5, the droplet advances at the lower side with an angle θ_A and recedes at the upper side with an angle θ_R. In order to let the droplet slide off, the surface must be tilted over the sliding angle θ_D. The *CAH* is associated with θ_D [67]; high contact angle hysteresis corresponds to high θ_D, which implies a lower tendency of droplet to roll of the surface, even if the contact angle is high. For this reason, a highly superhydrophobic surface should have high values of θ, but also low values of *CAH*. θ_A and θ_R can be observed with a simple experience. If a liquid droplet is withdrawn from a solid surface

(Fig. 6.6a), one can observe two steps. First, the droplet volume and the contact angle decrease, while the contact area remains constant. As the contact angle reaches a certain value, which remains constant during the process, the droplet volume continues to decrease and the contact area begins to recede. The same thing occurs if one adds water to the droplet (Fig. 6.6b); the volume, as well as the contact angle, increases but the contact area doesn't change until the contact angle will reach a constant value. Then, the contact angle remains constant, but the liquid volume and the contact area decrease. The constant values assumed by the contact angles during water droplet advancing and receding are respectively θ_A and θ_R.
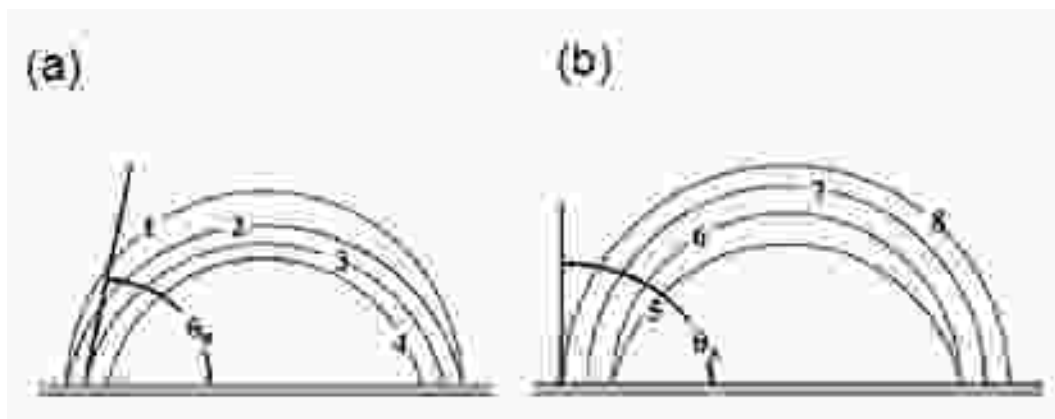
Figure 6.6: Advancing and receding contact angle: a simple experience. (a) Droplet of water receding on a surface; (b) Droplet of water advancing on a surface [59].

The *CAH* can be defined as the difference between θ_A and θ_R. Surface roughness has a strong effect on *CAH* [68-69]. If the surface is in the Wenzel wetting state, the contact angle is high (superhydrophobic surface), but liquid droplets on the surface remain unmoved until a high θ_D is reached. Conversely, if the surface is in the Cassie-Baxter state, the droplets slide off easily. Wenzel and Cassie-Baxter state are both hydrophobic from the contact angle point of view, but the first present higher values of *CAH*. When a surface presents a high contact angle ($\theta > 150°$) and low *CAH* ($\theta \rightarrow 0$) it is defined *self cleaning surface*. Water droplets through these surfaces easily roll off and clean the surface during the process. The self-cleaning property is usually associated with hierarchical structures (Fig. 6.3), where micro-scale and nano-scale roughness coexist.

The present paragraph presents the fundamental concepts, the most significant parameters and the classical approaches to describe surfaces wettability. From what

discussed above emerges that, in order to achieve a self-cleaning surface, one must ensure a high value of θ and a low *CAH*, which are associated with a Cassie-Baxter state. In order to improve wet probes, one must focus on the technologies which can ensure the self-cleaning property.

6.2 Superhydrophobicity: low energy materials and manufacturing processes.

The wettability of surfaces depends on the physic of materials (surface energy) and the surface roughness (technological process). The research on superhydrophobic material started from the observation of natural phenomena, especially plants leaves [70-71] and led to the development of superhydrophobic surfaces, with high contact angles and low *CAH*. The classical example of self-cleaning surface is the lotus leaf, which presents a hierarchical structure (Fig. 6.7). The scientific research on surfaces wettability pointed that the combination of a micro-scale and a nano-scale surface roughness, together with the use of a low energy material, lead to self cleaning surfaces. After the previous paragraph, where the fundamental concepts on surfaces wettability are discussed, the present section gives a short and general introduction to the main technological processes for superhydrophobic surfaces manufacturing.

The manufacturing approaches for superhydrophobic surfaces manufacturing can be divided into two directions [58, 59, 67, 71-73]:

- Top-down approaches
- Bottom-up approaches

Top-down approaches generate a superhydrophobic surface from a low energy material substrate. The most important top down treatments are template, lithography, plasma treatment and micromachining. The low surface energy materials used for top-down approaches [74] are fluorocarbons, for example Teflon, silicones like polydimethylsiloxane (PDMS), organic and inorganic materials. Examples of organic materials are polyethylene (PE), polyamide and polycarbonate.
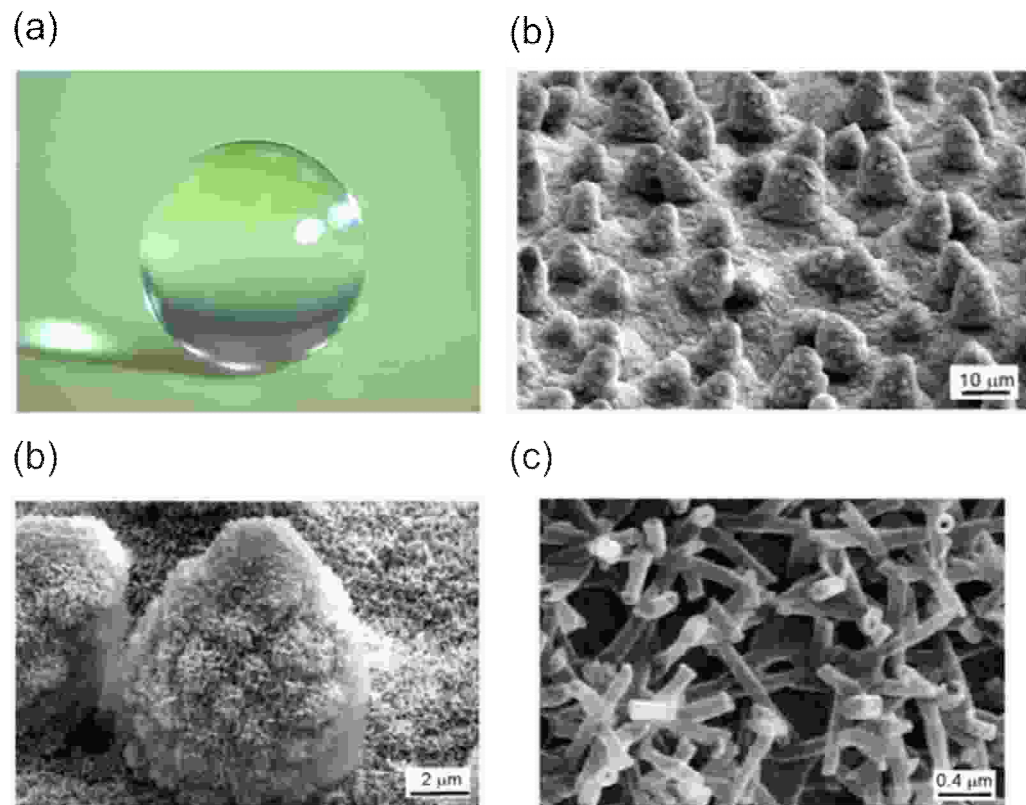
Figure 6.7: Lotus leaf surface. (a) macroscopic view; (c-d) SEM microscopic images [62].

Contrary to the top-down approach, bottom-up methods generate superhydrophobic surfaces with coating and chemical operations like self-assembly and self-organization, where components spontaneously assemble until a stable structure of minimum energy is reached. The main bottom-up treatments are chemical vapor deposition (CVD), layer by layer deposition, assembly and sol-gel.

The most required features for the present application are ease of application, economicity, durability and high hydrophobicity. The probes have a complex geometry and small dimensions, which will be reduced for their miniaturization. From this simple and general introduction, it seems that bottom-up approaches, where the surfaces can be treated with sprays or gel, are more suitable, even if more accurate studies are required before selecting a manufacturing approach.

The present chapter is a general introduction to surfaces wettability and superhydrophobic surfaces. In the first section the fundamental concepts, the main parameters and the classical models to study surfaces wettability are presented. Such

concepts are the basis for the selection of superhydrophobic materials for the present application. The second section presents the two main approaches related to the generation of superhydrophobic surfaces. From the above considerations it seems that the bottom-up approach results more suitable for the present application. However, this is only a preliminary consideration. In order to select the best manufacturing process to realize superhydrophobic probes, further researches are required, examining the single approaches from the following point of view:

- Contact angle
- Contact angle hysteresis
- Ease of application
- Uniformity
- Durability
- Mechanical strength
- Thermal conductivity

After selecting and applying the best approach to wet probes, they must be tested. If the results are satisfying, the research can extend to oleophobic materials, in order to realize an optimized probe for a real wet gas application

Chapter 7

Conclusions

The objective of this research activity was the development of probes for the measurement of total pressure and total temperature of gas phase in wet gas conditions. The requirement of such probes is a consequence of the research and development in subsea compression, which represents an important technology in the exploitation of natural gas resources, especially in the North Sea. The research on wet gas compression focused on the development of wet tolerant machines, which can operate with mixtures of hydrocarbon gases, liquids and water, with a liquid content up to 5% on a volume based. During performance tests on such machines standard total pressure and total temperature probes are used, leading to some errors due to the contact between liquid droplets and probes sensors. For this reason, the development of wet tolerant probes is a relatively new challenging topic, which supports the oil & gas companies in the fundamental phase of compressors performance tests. All the activities of this research are the result of a cooperation between University of Florence and GE Oil & Gas. Since no probes for this application were studied before, the present research aims to develop a validated methodology for wet probes design and characterization, with a wide range of application.

Basing on a literature search on two phase flows, standard probes for measurements in turbomachinery, and previous attempts to develop wet tolerant probes (related to different fields of application), the fundamental issues were identified. Then, the main physical principles were defined and converted into some conceptual designs. Finally, the most promising configurations were selected.

The following stage was the development of an analytical model for probes detailed design. The model, which was implemented into an EES code, provides a complete analysis of the expected probes performance, from the fluid dynamics and the structural point of view. The probes can be designed starting from the specific application operating conditions and from a first attempt geometry. Once the operating conditions are defined, one can play with probe geometry, until the required performance for nominal conditions are reached. After defining probe geometry, one can run the model in off-design conditions to obtain a complete performance characterization. The developed model aims to become a reference tool for wet probes design. For this reason, the following stages of the PhD activities were oriented to model validation.

The model was run for a real case, which consisted in a pressurized two phase flow, composed by air and water, with a LVF up to 3%. Such operating conditions corresponded to those of a wet compressors test facility located at SwRI (Southwest Research Institute, Texas). The model was run both in design and off-design conditions, and a parametric analysis was performed to assess probes behavior in a wide range of operation. From the simulations and the parametric analysis emerged that the model gave physically sound results, both from the fluid mechanics and the structural point of view. In order to preliminary validate the model, some FEM static and modal analyses were carried out; the results of these analyses were compared to those of the model in terms of mechanical stress and natural frequencies. The results of the numerical analysis confirmed those of the analytical model. The values of the mechanical stress and the first natural frequency obtained with the model show a percentage relative error lower than 6% respect to the numerical simulations.

Starting from the geometry obtained with the model, some prototypes of probes were manufactured with a Direct Metal Laser Sintering (DMLS) technique, which ensures high resolution and excellent mechanical properties. The most important geometrical parameters were then measured and compared with the nominal values; basing on these considerations, the best prototypes for the test campaign were selected. After probes manufacturing, some ping tests were performed on the selected prototypes. The results of the tests confirmed those obtained with the analytical and the numerical simulations. A percentage relative error on the first natural frequency lower than 2.0% was obtained

between the experimental and the numerical data. The analytical model showed greater values of the error, which was still lower than 8%.

After probes design, manufacturing and structural testing, this activity focused on performance tests on the selected prototypes. The first tests were performed in the dry aerodynamic facility of GE Oil & Gas (Florence), with atmospheric air as operating fluid. The operating conditions of dry tests were different from the reference points for probes design. The model was run with the prototypes geometry and with the operating conditions of the dry facility. The analytical and experimental results were compared in terms of recovery factor. The maximum relative percentage error between measured and calculated *r* was lower than 3% for total pressure probes and lower than 7% for total temperature probes. The highest errors occurred at low Mach number, where the measurement uncertainty had a great influence on results. The test performed in dry conditions confirmed that the model seems to be a reliable instrument for probes design.

The next tests were carried out in the wet compressors facility located at SwRI. Such a facility was a fundamental opportunity to test the probes in pressurized wet conditions, even if the operating points were not suitable for probes calibration. The flow velocity was lower than 30 m/s, leading to very low kinetic contributions, comparable to the measurement uncertainty. However, no wet facility for probes calibration was available during the present research activity, and the SwRI test rig represented the only chance to test the probes in wet conditions. The experimental results were compared to those obtained with the analytical model. Starting from total pressure probes, good results were obtained both in dry (SwRI test rig could operate both in dry and wet conditions) and wet conditions. The analytical and the measured data showed the same trend, confirming that the model gave physically sound results. The measured data were different from those calculated with the model, but this was a consequence of test conditions. Total temperature probes gave interesting results in dry conditions, where the analytical and experimental results showed the same trend, even if probes readings didn't agree with the model. The results of wet tests were more difficult to post-process than those in dry conditions. In this case the results of wet probes were compared to those of standard RTDs, located in close positions. From the results of wet tests it seemed that wet temperature probes were less

affected by water droplets than standard RTDs, even if the same behavior wasn't obtained in transient conditions.

From the performance tests discussed above emerges that the model gives interesting results for total pressure probes both in dry and wet conditions, and for total temperature probes in dry conditions. For this reason, the model can be considered only partially validated. Since the SwRI facility was not suitable for probes calibration, a wet gas test bench is under development.

In order to conclude the present research activity, some efforts were made to identify the best technologies to improve probes performances and miniaturize their design. A potential solution was identified in superhydrophobic materials. When a water droplet approaches a superhydrophobic surface, it slips away without wetting it. The main parameters and the classical approach to describe these materials were studied, together with the most important manufacturing processes to obtain these surfaces. From the first considerations emerge that superhydrophobic materials represents a very interesting challenge for the development of optimized probes and sensors, which can measure the thermodynamic properties of the gas phase without being affected by the wet phase, even if further studies are required.

The methodology developed and partially validated in the present research activity represents the basic instrument for the design of wet tolerant probes for wet gas applications. The present work must be followed by further tests on the dedicated facility, which is under developments and which allows a complete validation of the analytical model. After the model validation, some new probes based on superhydrophobic materials should be developed and tested, in order to understand how such materials can really improve probes design. If the principle of operation works well, another research on oleophobic materials must be performed, and a final probes configuration, optimized and minimized for a real wet mixture must be developed.

Bibliography

[1]   International Energy Agency, 2013. "2013 Key World Energy Statistics Report". www.iea.org/publications/freepublications/publication/KeyWorld2013.pdf

[2]   BP, 2014. "BP Statistical Review of World Energy June 2014". http://www.bp.com/en/global/corporate/about-bp/energy-economics/statistical-review-of-world-energy.html

[3]   Brenne, L., Bjørge, T.,Bakken, L. E., Hundseid, Ø. , 2008. "Prospect for subsea wet gas compression". *Proceedings of ASME Turbo Expo 2008* (GT2008-51158), June 9-13, 2008, Berlin, Germany.

[4]   Brenne, L., Bjørge, T., Gillaranz, J. L., Koch, J. M., Miller, H., 2005. "Performance evaluation of a centrifugal compressor operating under wet gas conditions". *Proceedings of the Thirthy-Fourth Turbomachinery Symposium*, Houston, USA.

[5]   Hundseid, Ø., Bakken, L. E., 2006. "Wet gas performance analysis". *Proceedings of ASME Turbo Expo 2006* (GT2006-91035), May 8-11, 2006, Barcelona, Spain.

[6]   Hundseid, Ø., Bakken, L. E., Grüner, T. G., Brenne, L., Bjørge, T., 2008. "Wet gas performance of a single stage centrifugal compressor". *Proceedings of ASME Turbo Expo 2008* (GT2008-51156), June 9-13, 2008, Berlin, Germany.

[7]   Wood, A. B., 1944. *A textbook of sound*. Bell.

[8]   Grüner, T. G., Bakken, L. E., Brenne, L., Bjørge, T., 2008. "An experimental investigation on airfoil performance in wet gas flow". *Proceedings of ASME Turbo Expo 2008* (GT2008-50483), June 9-13, 2008, Berlin, Germany.

[9]   Fabbrizzi, M., Cerretelli, C., Del Medico, F., D'Orazio, M., 2009. "An experimental investigation of a single stage wet gas centrifugal compressor". *Proceedings of ASME Turbo Expo 2009* (GT2009-59548), June 8-12, 2009, Orlando, Florida, USA.

[10]   Ransom, D., Camatti, M., Bertoneri, M., Podestà, L., Wilcox, M., Bigi, M., 2011. "Mechanical performance of a two stage centrifugal compressor under wet gas conditions". *Proceedings of the Fortieth Turbomachinery Symposium*, September 12-15, 2011, Houston, Texas, pp. 121-128.

[11]   Bertoneri, M., Duni, S., Ransom, D., Podestà, L., Camatti, M., Bigi, M., Wilcox, M., 2012. "Measured performance of a two-stage centrifugal compressor under wet gas conditions". *Proceedings of ASME Turbo Expo 2012* (GT2012-69819), June 11-15, 2012, Copenaghen, Denmark.

[12]   Wuest, W., 1980. "Pressure and Flow Measurement". AGARDograph No. 160, 7 rue Ancelle, 92200 Neuilly sur Seine, France.

[13]   Folsom, R. G., 1956. "Review of the Pitot Tube", Trans. ASME, 78, pp. 1447-1460.

[14]   Doebelin, E. O., 2004. *Measurement systems: Application and Design fifth edition*. The McGraw-Hill Companies.

[15]   Dudziniski, T. J., Krause, L. N., 1971. "Effect of inlet geometry on flow-angle characteristics of miniature total-pressure tubes". NASA Technical Note No. D-6406, Washington, D.C. 20546.

[16]   Kiel, G., 1935. "Total Head meter with small sensitivity to yaw". NACA Technical memorandum No. 775, Washington, D.C. 20546.

[17]   www.unitedsensorcorp.com/kiel.html

[18]   Glawe, G. E., Holanda, R., Krause, L.N., 1978. "Recovery and radiation corrections and time constants of several sizes of shielded and unshielded thermocouple probes for measuring gas temperature". NASA Technical Paper No. 1099, Washington, D.C. 20546.

126

[19] Bidini, G., Manfrida, G., Valentini, E.,1987, "Assessment of measurement error for gas-turbine total temperature probes". Fluid Measurement and Instrumentation Forum 1987, ASME Fluids Engineering Division-Cincinnati, Ohio, U.S.A., June 14-18.

[20] Saravanamuttoo, H. I. H., 1990. "Recommended practices for measurement of gas path pressures and temperatures for performance assessment of aircraft turbine engines and components". AGARD Advisory Report No. 245, 7 rue Ancelle, 92200 Neuilly sur Seine, France.

[21] Zeisberger, A., 2007. "Total temperature probes for turbine and combustor applications". *Proceedings of ISABE 2007* (ISABE-2007-1108), September 2-7, 2007, Beijing, China.

[22] Bidini, G., Manfrida, G., Valentini, E., 1989. "Accurate prediction of gas turbine total temperatures: validation of the radiation error model". ASME Fluid Measurement and Instrumentation Forum, 1989.

[23] Dussourd, J. L., Shapiro, A. H., 1958. "A deceleration probe for measuring stagnation pressure and velocity of a particle-laden gas stream". *Jet Propulsion*, January 1958, pp. 24-34.

[24] Murthy, S. N. B., Leonardo, M., Ehresman, C. M., 1986. "A stagnation pressure probe for droplet-laden air flow", *Jet Propulsion*, Vol. 2, No. 2, May-June 1986, pp.195-196.

[25] Benton, T. K., Seay, J. R., 1985. Apparatus for measuring fluid flow rate in a two-phase fluid stream, Oct. 8. US Patent 4545260.

[26] Colten, T. M., Brown, W. W., Nelson, R. L., 2010. Pitot probe with water blockage prevention, May 18. US Patent 7716980.

[27] Kovach, K., Beede, W. L., Hamrick, J. T., 1951. "Experimental evaluation by thermodynamic methods of work input to a centrifugal compressor operating with water injection". NACA Research Memorandum No. E50J31, Washington, D.C. 20546.

[28]   Kievet, F. G., Van Raaij, J., Kerkhof, P. J. A. M., 1997. "A device for measuring temperature and humidity in a spray dryer". *Transactions of the Institution of Chemical Engineers*, **75**(A), pp. 329-333.

[29]   Kock, F., Kockel, T. K., Tuckwell, P. A., Langrish, T. A. G., 2000. "Design, numerical simulation and experimental testing of a modified probe for measuring temperatures and humidities in two-phase flow". *Chemical Engineering Journal*, **76**, pp. 49-60.

[30]   Dimarzo, M., Ruffino, P., 2003. Sensor probe for measuring temperature and liquid volumetric fraction of a liquid droplet laden hot gas and method of using same. US Patent 6609412.

[31]   Gerbi, F., Marrazzo, M., Maraschiello, F., Manfrida, G., 2014. Total pressure and total temperature measurement in wet gas condition. WO 2014/095711 A1.

[32]   F – Chart Software. http://www.fchart.com/ees/

[33]   Fox, R. W., McDonald, A. T., Pritchard, P. J., 2003. *Introduction to Fluid Mechanics, Sixth Edition*. John Wiley & Sons, Inc.

[34]   White, F. M., 2011. *Fluid Mechanics, Seventh Edition*. The McGraw-Hill Companies.

[35]   Sabetta, F., 1999. *Gasdinamica.* Edizioni Ingegneria 2000.

[36]   Crowe, C., Sommerfeld, M., Tsuji, Y., 1998. *Multiphase Flows with Droplets and Particles*. CRC Press LLC.

[37]   Medaugh, F. W., Johnson, G. D., 1940. "Investigation of the discharge and coefficient of small circular orifices". *Civ. Eng. (N.Y.)*, **7**, pp. 422-424.

[38]   Lienhard (V), J. H., Lienhard (IV), J. H., 1984. "Velocity coefficients for free jets from sharp-edged orifices". *Journal of Fluids Engineering*, **106**, pp. 13-17.

[39]   Hay, N., Lampard, D., 1998. "Discharge coefficient of turbine cooling holes: a review". *ASME Journal of Turbomachinery,* **120**, pp. 314-319.

[40] Rowbury, D. A., Oldfield, M. L. G., Lock, G. D., 2001. "A method for correlating the influence of external crossflow on the discharge coefficients of film cooling holes". *ASME Journal of Turbomachinery*, **123**, pp. 258.265.

[41] Gritsch, M., Schulz, A., Witting, S., 2001. "Effect of crossflows on the discharge coefficient of film cooling holes with varying angles of inclination and orientation". *ASME Journal of Turbomachinery*, **123**, pp.781-787.

[42] Da Soghe, R., Andreini, A., 2013. "Numerical characterization of pressure drop across the manifold of turbine casing cooling system". *ASME Journal of Turbomachinery*, **135**.

[43] Huening, M., 2012. "Discharge coefficient measurements of round, inclined orifices with inlet cross-flow in and against direction of inclination". *Proceedings of the Institution of Mechanical Engineers, Part C: Journal of Mechanical Engineering Science*, pp. 319-328.

[44] Schlichting, H., 1970. *Boundary-Layer Theory, Seventh Edition*. McGraw-Hill Series in Mechanical Engineering, McGraw-Hill Book Company.

[45] Budynas, R. G., Nisbett, J. K., 2011. *Shigley's Mechanical Engineering Design, Ninth Edition*. The McGraw-Hill Companies.

[46] www.matweb.com

[47] Bannantine, J. A., Comer, J. J., Handrock, J. L., 1990. *Fundamentals of Metal Fatigue Analysis*. Prentice Hall.

[48] Stephens, R. I., Fatemi, A., Stephens, R. R., Fuchs, H. O., 2001. *Metal Fatigue in Engineering, 2ⁿᵈ Edition*. John Wiley & Sons.

[49] Matsumoto, M., 1999. "Vortex shedding of bluff bodies: a review". *Journal of Fluids and Structures* **13**, pp. 791-811.

[50] Sarioglu, M., Yavuz, T., 2000. "Vortex shedding from circular and rectangular cylinders placed horizontally in a turbulent flow". *Turkish Journal of Engineering and Environmental Sciences* **24,** pp. 217-228.

[51] Thai Hoa, L. 2005. "Reviews on bluff body flow around prism and girders".

[52] Harris, C. M., Piersol, A. G., 2002. *Harris' Shock and Vibration Hanbook, fifth edition*. The McGraw-Hill Companies.

[53] Genta, G., 1998 *Vibrations of Structures and Machines-Pratical Aspects, third edition*. Springer, New York.

[54] http://www.solidworks.com/sw/products/simulation/structural-analysis.htm

[55] Zienkiewicz, O. C., Taylor, R. L., 2000. *The Finite Element Method, Fifth Edition*. Butteworth Heinemann.

[56] Simchi, A., Petzold, F., Pohl, H., 2003. "On the development of diret metal laser sintering for rapid tooling". *Journal of Materials Processing Technology* **141**, pp. 319-328.

[57] http://www.swri.org/4org/d18/mechflu/wet-gas-comp/default.htm

[58] Shirtcliffe, N. J., McHale, G., Atherton, S., Newton, M. I., 2010. "An introduction to superhydrophobicity", *Advanced in Colloid and Interface Science* **161**, pp. 124-138.

[59] Yan, Y. Y., Gao, N., Bathlott, W., 2011. "Mimicking natural superhydrophobic surfaces and grasping the wetting process: A review on recent progress in preparing superhydrophobic surfaces". *Advanced in Colloid and Interface Science* **169**, pp. 80-105.

[60] Yoshimitsu, Z., Nakajima, A., Watanabe, T., Hashimoto, K., 2002. "Effects of surface structure on the hydrophobicity and sliding behavior of water droplets", *Langmuir* **18**, pp. 5818-5822.

[61] Adamson, A. W., Gast, A. P., 1997. *Physical chemistry of surfaces, Sixth Edition*. Wiley Blackwell.

[62] Bhushan, B., Jung, Y. C., 2011. "Natural and biomimetic artificial surfaces for superhydrophobicity, self-cleaning, low adhesion and drag reduction". *Progress in Materials Science* **56**, pp. 1-108.

[63]   Wenzel, R. N., 1936. "Resistance of solid surfaces to wetting by water". *Ind Eng Chem* **28**, pp. 988-994.

[64]   Wenzel, R. N., 1949. "Surface roughness and contact angle". *J Phys Colloid Chem* **53**, pp. 1466-7.

[65]   Cassie, A. B. D., Baxter, S., 1944. "Wettability of porous surfaces". *Trans Faraday Soc* **40**, pp. 0546-50.

[66]   Cassie, A. B. D., 1948. "Contact angles". *Discussion of the Faraday Society* **3**, pp. 11-16.

[67]   Ji, H., Chen, G., Hu, J., Wang, M., Min, C., Zhao, Y., 2013. "Biomimetic superhydrophobic surfaces". *Journal of Dispersion Science and Technology* **34**, pp. 1-21.

[68]   He, B., Lee, J., Patankar, N. A., 2004. " Contact angle hystesesis on rough hydrophobic surfaces". *Colloids and Surfaces A: Physicochem. Eng. Aspects* **248**, pp. 101-104.

[69]   Wang, X. D., Peng, X. F., Lu, J. F., Liu, T., Wang, B. X., 2004. "Contact angle hysteresis on rough solid surfaces". *Heat Transfer-Asian Research* **33**, pp. 201-210.

[70]   Barthlott, W., Neinhuis, C., 1997. "Purity of the sacred lotus, or escape from contamination in biological surfaces". *Planta* **202**, pp.1-8.

[71]   Kock, K., Bhushan, B., Barthlott, W., 2008. "Diversity of structure, morphology and wetting of plant surfaces", *Soft Matter* **4**, pp. 1943-63.

[72]   Celia, E., Darmanin, T., Taffin de Givenchy, E., Amigoni, S., Guittard, F., 2013. "Recent advances in designing superhydrophobic surfaces". *Journal of Colloid and Interface Science* **402**, 1-18.

[73]   Li, X. M., Reinhoudt, D., Crego-Calama, M., 2006. "What do we need for a superhydrophobic surface? A review on the recent progress in the preparation of superhydrophobic surfaces". *Chem. Soc. Rev.* **36**, pp. 1350-1368.

[74]   Ma, M., Hill, R. M., 2006. "Superhydrophobic surfaces". *Current Opinion in Colloid & Interface Science* **11**, pp. 193-202.